Université de Toulouse

THÈSE

En vue de l'obtention du

DOCTORAT DE L'UNIVERSITÉ DE TOULOUSE

Délivré par :
Institut National Polytechnique de Toulouse (INP Toulouse)

Discipline ou spécialité :

Micro-ondes, Electromagnétisme et Optoélectronique

Présentée et soutenue par :
Ahmed ALI MOHAMED ALI SAYED AHMED

le : mardi 4 mai 2010

Titre :

Développement de Nouveaux Composants Passifs Multicouches et l'Implémentation d'une Matrice de Butler Large-Bande et Compacte en Technologie GIS

JURY

Pr. Ke WU; Pr. Roberto SORRENTINO; Pr.Thierry MONEDIERE; Pr. Bernard JECKO; Pr. Hervé AUBERT; Dr. Fabio COCCETTI; Nelson FONSECA

Ecole doctorale :
Génie Electrique, Electronique et Télécommunications (GEET)

Unité de recherche :
LAAS-CNRS

Directeur(s) de Thèse :

Pr. Hervé AUBERT

Rapporteurs :

Pr. Ke WU; Pr. Roberto SORRENTINO; Pr.Thierry MONEDIERE

LIST OF CONTENTS

CHAPTER FOUR

TWO-LAYER WIDEBAND SIW BEAM-FORMING MATRICES

LIST OF TABLES

LIST OF FIGURES

LIST OF ABBREVIATIONS

BFN	Beam-forming network
BI-RME	Boundary integral-resonant mode expansion
CAD	Computer Aided Designs
CDMA	Code division multiple access
CRLH	Composite Right left handed
EM	Electromagnetic
FDMA	Frequency division multiple access
FDTD	Finite difference time domain
FSIW	Folded substrate integrated waveguide
HMIC	Hybrid microwave integrated circuits
HMSIW	Half-mode substrate integrated waveguide
LAAS	Laboratory of analysis and architecture of systems
LH	Left-handed
LTCC	Low temperature co-fired ceramics
M-BFN	Multiple beam-forming network
MIMO	Multiple Input/Multiple Output
MPA	Multi-port amplifiers
PCB	Printed circuit board
RH	Right-handed
RSIW	Ridged substrate integrated waveguide
SDMA	Space division multiple access
SIC	Substrate integrated circuits
SIW	Substrate integrated waveguide
SLL	Side lobe-level
SoS	System on substrate
TDMA	Time division multiple access
TE	Transverse electric
TEM	Transverse electromagnetic
TM	Transverse magnetic
VNA	Vector network analyzer

ACKNOWLEDGEMENTS

The first to thank for giving me the power to do this job is GOD. You have given me strength, satisfaction and joy while doing my job through those surrounding me starting with my family that is always of great support to me.

This work has been achieved in the "Laboratoire d'Analyse et d'Architecture des Systèmes" of the "Centre National de la Recherche Scientifique" (LAAS-CNRS), Toulouse, within the "Micro et Nanosystèmes pour les Communications sans fils" (MINC) research group.

I would like to thank my supervisor, Prof. Hervé AUBERT, professor at the INP-Toulouse and LAAS-CNRS, for proposing this interesting research subject to me, for his precious scientific discussions that have guided me all along my thesis, his availability, and continuous support.

I would also like to thank Prof. Robert PLANA, head of the MINC research team at the LAAS-CNRS for giving me the chance to be one of his team, for providing all needed equipments, material and software and for ensuring this harmony within the group.

I would also like to express my acknowledgement to Eng.M.Sc.Nelson FONSECA, formerly engineer at the CNES-Toulouse and currently at the European Space Agency (ESA) for suggesting lots of interesting ideas along this thesis and for his sincere contributions.

Dr. Fabio COCCETTI, thank you for your interesting ideas and helpful discussions. You are a colleague that I appreciate and a friend that I respect.

Also I would like to express my gratitude to Prof. Hani GHALI, professor at the Ain Shams University, Egypt. Prof. Hani, thank you for introducing me to this wonderful group and continuous belief in me.

I am deeply thankful to Prof. Ke WU, Canada Research Chair and head of Polygrames Research Center, Prof. Roberto SORRENTINO, professor at the university of Perugia, Italy as well as Prof. Thierry MONEDIERE, professor at Limoges University and XLIM research institute, for accepting to examine my thesis.

I also dedicate my special thanks to my dear wife, friend and colleague, Heba. This thesis is one more happy achievement that I owe you, and because of your support I am sure it is not the last. Together, we could always overcome lots of difficult moments.

To my mother, sisters and to the memory of my father, you have been great parents to me. Your sacrifices and support offer me great help and continuous motivation.

I also would like to thank my friend and colleague Tarek DJERAFI, for his precious help that I appreciate and the successful collaboration we have. I am also grateful to Prof. Ke WU for providing the fabrication facilities at PolyGrames Research Center.

Finally, I thank all my friends and colleagues that were of great help to me by participating in this healthy and friendly environment.

ABSTRACT

Multibeam antennas have become a key element in nowadays wireless communication systems where increased channel capacity, improved transmission quality with minimum interference and multipath phenomena are severe design constraints. These antennas are classified in two main categories namely adaptive smart antennas and switched-beam antennas. Switched-beam antennas consist of an elementary antenna array connected to a Multiple Beam Forming Network (M-BFN). Among the different M-BFNs, the Butler matrix has received particular attention as it is theoretically lossless and employs the minimum number of components to generate a given set of orthogonal beams (provided that the number of beams is a power of 2). However, the Butler matrix has a main design problem which is the presence of path crossings that has been previously addressed in different research works.

Substrate Integrated Waveguide (SIW) features interesting characteristics for the design of microwave and millimetre-wave integrated circuits. SIW based components combine the advantages of the rectangular waveguide, such as the high Q factor (low insertion loss) and high power capability while being compatible with low-cost PCB and LTCC technologies. Owing to its attractive features, the use of SIW technology appears as a good candidate for the implementation of BFNs. The resulting structure is therefore suitable for both waveguide-like and planar structures.

In this thesis, different novel passive components (couplers and phase shifters) have been developed exploring the multi-layer SIW technology towards the implementation of a two-layer compact 4×4 Butler matrix offering wideband performances for both transmission magnitudes and phases with good isolation and input reflection characteristics.

Different techniques for the implementation of wideband fixed phase shifters in SIW technology are presented. First, a novel waveguide-based CRLH structure is proposed. The structure is based on a single-layer waveguide with shunt inductive windows (irises) and series transverse capacitive slots, suitable for SIW implementations for compact phase shifters. The structure suffers relatively large

insertion loss which remains however within the typical range of non-lumped elements based CRLH implementations.

Second, the well-known equal length, unequal width SIW phase shifters is discussed. These phase shifters are very adapted for SIW implementations as they fully exploit the flexibility of the SIW technology in different path shapes while offering wideband phase characteristics. To satisfy good return loss characteristics with this type of phase shifters, the length has to be compromised with respect to the progressive width variations associated with the required phase shift values. A two-layer, wideband low-loss SIW transition is then proposed. The transition is analyzed using its equivalent circuit model bringing a deeper understanding of its transmission characteristics for both amplitude and phase providing therefore the basic guidelines for electromagnetic optimization. Based on its equivalent circuit model, the transition can be optimized within the well equal-length SIW phase shifters in order to compensate its additional phase shift within the frequency band of interest. This two-layer wideband phase shifter scheme has been adopted in the final developed matrix architecture.This transition is then exploited to develop a three-layer, multiply-folded waveguide structure as a good candidate for compensated-length, variable width, low-loss, compact wideband phase shifters in SIW technology.

Novel two-layer SIW couplers are also addressed. For BFNs applications, an original structure for a two-layer 90° broadband coupler is developed. The proposed coupler consists of two parallel waveguides coupled together by means of two parallel inclined-offset resonant slots in their common broad wall. A complete parametric study of the coupler is carried out including the effect of the slot length, inclination angle and offset on both the coupling level and the transmission phase. The first advantage of the proposed coupler is providing a wide coupling dynamic range by varying the slot parameters allowing the design of wideband SIW Butler matrix in two-layer topology. In addition, previously published SIW couplers suffer from direct correlation between the transmission phase and the coupling level, while the coupler, hereby proposed, allows controlling the transmission phase without significantly affecting the coupling level, making it a good candidate for BFNs employing different couplers, such as, the Nolen matrix.

A novel dual-band hybrid ring coupler is also developed in multi-layer Ridged SIW (RSIW) technology. This coupler has been jointly developed with Tarek Djerafi in a collaboration scenario with Prof. Ke Wu from the Ecole Polytechnique

de Montréal. The coupler has an original structure based on two concentric rings in RSIW topology with the outer ring periodically loaded with radial, stub-loaded transverse slots. A design procedure is presented based on the Transverse Resonance Method (TRM) of the ridged waveguide together with the simple design rules of the hybrid ring coupler. A C/K dual band coupler with bandwidths of 8.5% and 14.6% centered at 7.2 GHz and 20.5 GHz, respectively, is presented. The coupler provides independent dual band operation with low-dispersive wideband operation.

Finally, for the Butler matrix design, the two-layer SIW implementation is explored through a two-fold enhancement approach for both the matrix electrical and physical characteristics. On the one hand, the two-layer topology allows an inherent solution for the crossing problem allowing therefore more flexibility for phase compensation over a wide frequency band. This is achieved by proper geometrical optimization of the surface on each layer and exploiting the SIW technology in the realization of variable width waveguides sections with the corresponding SIW bends. On the other hand, the two-layer SIW technology is exploited for an optimized space saving design by implementing common SIW lateral walls for the matrix adjacent components seeking maximum size reduction. The two corresponding 4×4 Butler matrix prototypes are optimized, fabricated and measured. Measured results are in good agreement with the simulated ones. Isolation characteristics better than -15 dB with input reflection levels lower than -12 dB are experimentally validated over 24% frequency bandwidth centered at 12.5 GHz. Measured transmission magnitudes and phases exhibit good dispersive characteristics of 1dB, around an average value of -6.8 dB, and 10° with respect to the theoretical phase values, respectively, over the entire frequency band.

CHAPTER ONE

State of the Art of Beam-Forming Matrices with SIW Technology

1.1. Introduction

The increasing development of wireless applications introduces new requirements for the related terrestrial and spatial communication systems. These requirements imply severe constraints regarding an increased channel capacity with improved transmission quality with minimum interference and multipath phenomena. Different communication multiple access schemes have been developed to satisfy these needs; such schemes include the Frequency Division Multiple Access (FDMA), Time Division Multiple Access (TDMA) and Code Division Multiple Access (CDMA). For further increase of the channel capacity, another approach can be combined to the three former conventional access methods. This approach allows different users to access the same time-frequency or code channel within the same cell using Space Division Multiple Access (SDMA). Recently, the SDMA has offered new applications for multibeam antennas for both terrestrial and spatial applications [1].

This chapter presents the state of the art of beam-forming matrices, and in particular, those implemented using Substrate Integrated Waveguide technology. The chapter is organized as follows; Section 1.2 addresses the historical background of beam-forming matrices citing different relevant articles with different technologies. The need of implementing BFNs in waveguide-like technology with planar topology is clarified. In Section 1.3, the Substrate Integrated Waveguide technology is introduced starting from the basic concept, the historical development and going

briefly through some SIW implementations. The basic SIW design considerations are discussed in Section 1.4. In Section 1.5, the mostly employed techniques for miniaturization of Substrate Integrated Circuits (SICs) are addressed. Section 1.6 focuses on the so far published SIW implementations of BFNs followed by a conclusion in Section1.7.

1.2. Historical Development of Beam Form Matrices

To realize a multi-beam antenna, one way is to use an elementary antenna array properly fed by means of a Multiple Beam Forming Network (M-BFN) – also called Multiple Input/Multiple Output (MIMO) matrix. Multi input, multi output beam forming matrices are characterized by a number of inputs equal to the number of beams to produce and a number of outputs equal to the number of elementary radiators in the antenna array [2]. Such antennas are extensively used in Space Division Multiple Access (SDMA) applications. The M-BFN subsystem can also be used in Multi-Port Amplifiers (MPA) for distributed amplification. This technique is used in satellite communication systems to ensure similar optimum efficiency for all amplifiers [3].

Since the early 1960's, different types of (M-BFNs) have been proposed, such as Blass matrix [4], Nolen matrix [5], Rotman lens [6] and Butler matrix [7]. Among these different matrices, the Butler matrix has received particular attention in literature as it is theoretically lossless and employs the minimum number of components to generate a given set of orthogonal beams, provided that the number of beams is a power of 2. However, the Butler matrix has a main design problem which is the presence of path crossings. To overcome this problem, some specific designs have been suggested but they are not easily scalable for larger matrices [8], [9]. Another well-known method for single-layer realizations is to employ extra 0dB couplers by means of back-to-back pairs of 3 dB couplers to produce the crossover transfer function [3], [10]. This leads to an increased number of components with increased losses especially for larger matrices. In [11], a Lange coupler is used to replace the crossover offering therefore an interesting planar design with wideband performances. However, the complete structure is rather adapted to microstrip technology as it requires wire bonding.

Good performances have also been obtained using a multi-layered design

with suspended stripline technology [12]. However, the circuit suffers from a linear phase variation with frequency despite its fabrication complexity. A coplanar waveguide-based two-layer structure is suggested in [13]. However, this solution suffers from being narrow band for both transmission magnitude and phase, consequently, it is very sensitive to technological tolerances.

To avoid radiation losses, scan losses and/or coupling problems that might occur between the different paths of the matrix and the other components especially the radiating elements, waveguide implementations are recommended. On the other hand, as BFNs can be used in MPA systems, waveguide implementations become better for such applications owing to their improved power handling capability with respect to the other planar structures. However, such implementations suffer from the classic waveguides problems in terms of the resulting bulky structures, low integration profile and excitation problems and limited applications due to the large weight especially for space aircrafts or satellites applications requiring light weight, low profile and high integration density. Such waveguide implementations are found in literature [3]. Computer Aided Design (CAD) optimization has also been reported in [10] where rigorous fabrication-oriented optimization is presented followed by mechanical and thermal considerations for related structures reported in [14]. In [15], a complete waveguide-based structure has been reported for a narrow-band Butler matrix. Although the two-layer design offers a solution for the crossing arms problem in a compact area layout, the bulky waveguide problem has not been solved.

In order to obtain the advantages of rectangular waveguides while remaining in planar profiles, Substrate Integrated Waveguide (SIW) technology becomes an interesting candidate for the implementation of such matrices. The SIW technology is indeed a compromise between both planar and waveguide technologies, that features interesting characteristics in terms of ease of integration to other circuit components while offering components with high quality factors.

1.3. Historical Background of SIW

The substrate integrated waveguide technology is based on realizing a waveguide within a dielectric substrate. The upper and lower substrate metallization are used as the broad walls of the waveguide structure while the side narrow walls are synthesized in the form of two rows of metalized via-holes or grooves connecting the top and bottom metallic plates, Fig.1.1. The resulting structure is a waveguide

that possesses a planar profile and offers the good performances of metallic waveguides.

Since the early 1990's, different attempts have been proposed towards the implementation of waveguide structures in planar form. The first reference in literature is a Japanese patent in 1994 in which a new dielectric-filled waveguide is proposed in the form of a two rows of metallic vias in a dielectric substrate [16]. Shortly later, another U.S. patent reports the implementation of the waveguide with Low Temperature Co-fired Ceramics (LTCC) process and calling it a layered dielectric structure [17]. In 1997, a preliminary use of the SIW technology for millimeter-wave antenna arrays applications appears in [18] followed by further related studies by the same team in [19] and SIW components in LTCC by another Japanese team in [20].

Since the early 2000's, a renew of interest to the SIW technology and SIW-based components has been intensively carried out by the team led by Prof. Ke Wu at the Polygrames Research Center. A particular effort has been focused by the latter team on the design and modeling of SIW components, planar excitations and interconnects introducing the concept of Substrate Integrated Circuits (SIC) as a new vision of System on Substrate (SoS). A simple microstrip to SIW transition reported in 2001 has promoted the research on SIW [21] and became in fact one of the most cited references in SIW works employing planar excitations. Most of the classical microwave components have been mapped into SIW technology. This includes different planar transitions [21]-[26], filters [27]-[32], couplers [33]-[35], diplexers [36]-[37], six-port circuits [38], circulators [39], [40], and antennas [41]-[46]. Exploiting its ease of integration, several active components have been implemented in SIW technology. Such implementations include oscillators [47, 48], mixers [49] and amplifiers [50, 51].

1.4. SIW Design Considerations

In literature, a number of articles treated the analysis and modeling of SIW components [41], [52]-[56]. In 2002, Cassivi et al. have studied the dispersion properties of SIW in case of a rectangular waveguide using the Boundary Integral-Resonant Mode Expansion (BI-RME) method combined with the Floquet's theorem [52]. Upon their study, it was shown that the SIRW has the same guided-wave characteristics as the conventional rectangular waveguides. Empirical equations have

been extracted for the equivalent rectangular waveguide width giving the same characteristics for the fundamental mode propagating in the SIW having the same height and dielectric filling, such that:

$$a_{SIW} = a_{RWG} + \frac{d^2}{0.95h} \tag{1.1}$$

Where a_{SIW} and a_{RWG} are the widths of the SIW and its equivalent classical rectangular waveguide, respectively, d is the via-hole diameter and h is the waveguide substrate height, see Fig. 1.1.

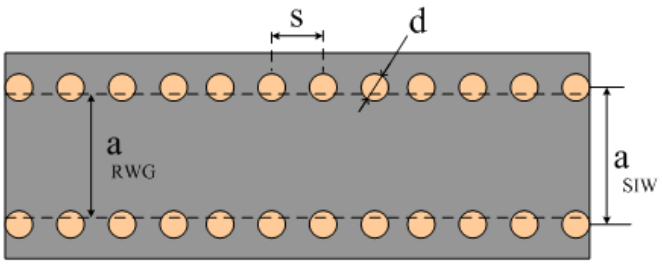

Fig. 1.1 Configuration of an SIW structure synthesized using metallic via-hole arrays.

According to [52], Eq. (1.1) has a precision within ±5% for $h < \lambda_o \sqrt{\varepsilon_r}/2$ and h< 4 *d*.

In 2004, Yan et al. reported experimental formula for a_{RWG}/a_{SIW} [41], such that:

$$a_{RWG} = a_{SIW} \times \left(\xi_1 + \frac{\xi_2}{\frac{s}{d} + \frac{\xi_1 + \xi_2 - \xi_3}{\xi_3 - \xi_1}} \right) \tag{1.2}$$

where

$$\xi_1 = 1.0198 + \frac{0.3465}{\frac{a_{SIW}}{s} - 1.0684}$$

$$\xi_2 = -0.1183 - \frac{1.2729}{\frac{a_{SIW}}{s} - 1.2010}$$

$$\xi_3 = 1.0082 - \frac{0.9163}{\frac{a_{SIW}}{s} + 0.2052}$$

The relative error of the formula of Eq. (1.2) has been estimated below 1%, [41]. It has to be noted that, the formulas given by Eq. (1.1) and Eq. (1.2) are generally used to obtain initial values for the equivalent width. These values are generally subject to optimizations based on full-wave commercial simulators. For SIW components with more generalized shapes, two basic design rules related to the metalized hole diameter and pitch size are used to neglect the radiation loss. These two rules are sufficient but not always necessary [58, 59], the two conditions are given by Eq. (1.3) as

$$d < 0.2\,\lambda_{g,} \qquad s \leq 2d \tag{1.3}$$

where λ_g is the waveguide wavelength.

In 2005, an interesting study of the leakage characteristics of SIW has been carried out by Xu et al. based on a numerical multimode calibration procedure [57]. In their study, several interesting conclusions have been reported. This includes the fact that SIW structures synthesized in terms of periodic metal-plated via-holes can support only the propagation of TE_{n0} modes. This natural filter characteristic has encouraged indeed the use of SIW technology in many applications providing enhanced performances for filer-related applications. On the other hand, by noting the surface electric current distribution, a technological condition has been underlined. A good contact of the metalized vias with both metal plates of the substrate is a must in order not to perturb the surface current density for the TE_{n0} modes. A further improvement in the equivalent width formula has also been proposed in [52] and given by Eq. (1.4).

$$a_{RWG} = a_{SIW} - 1.08\frac{d^2}{s} + 0.1\frac{d^2}{a_{SIW}} \tag{1.4}$$

1.5. Miniaturization Techniques of SICs

By comparing the SIW based components to their equivalent realizations in planar transmission lines supporting TEM or quasi TEM propagation, one can note that the size of the former ones is much larger than that of other planar realizations. This is simply due to the fact that the width of the SIW, for normal right-handed propagation, is strictly related to the operating frequency band. The width of the

other planar transmission lines is rather related to the impedance. Reducing the size of SIW components to be comparable to those implemented in planar transmission lines becomes therefore a challenging need especially for relatively low microwave frequency bands.

So far, several SIW miniaturization techniques have been proposed. In 2004, Grigoropoulos et al. have suggested compact folded SIW (FSIW) [60]. The structure is analogous to that reported in [61, 62] so called T-septum waveguide using the dielectric-filled SIW implementation. The guide operates as a conventional waveguide whose sides have been folded underneath its central part. In fact, there are two types of FSIW structures, namely the C-type FSIW and the T-type FSIW, [63, 64].

Another method for SIW miniaturization in single-layer topology has been proposed by Profs. Wu and Hong by introducing the Half-Mode SIW (HMSIW) [65]. A size reduction up to 50% has been verified by bisecting the SIW along the maximum electric field region along the length. Owing to the large width-to-height ration, each resulting half-open structure becomes a HMSIW structure that keeps almost the same original field distribution in its own part. The principle is also applicable on multi-layered structures as in [66] where the same group proposes the Folded HMSIW (FHMSIW).

The use of single Ridged waveguide in multi-layered SIW implementations (RSIW) has also been explored for miniaturization of SIW components. The increased bandwidth of ridged waveguides with respect to classical rectangular waveguides is directly translated in terms of size miniaturization. A tapered microstrip access transition with tapered RSIW has been reported in [67] providing therefore an interesting microstrip excitation for relatively thick SIW through the tapered RSIW section. Several investigations on the RSIW, FSIW and TFSIW have been then carried out by Ding et al. in [68]-[70]. Fig. 1.2 illustrates several realizations of compact SIW components.

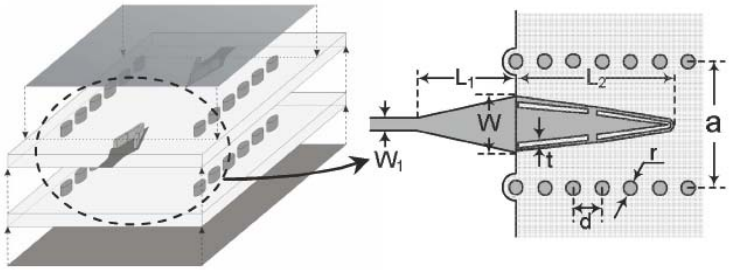

(a)

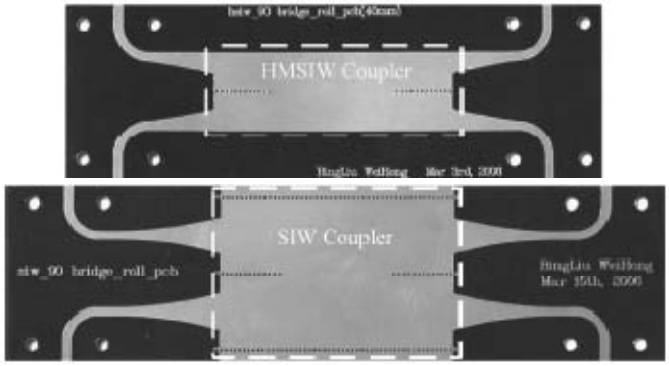

(b)

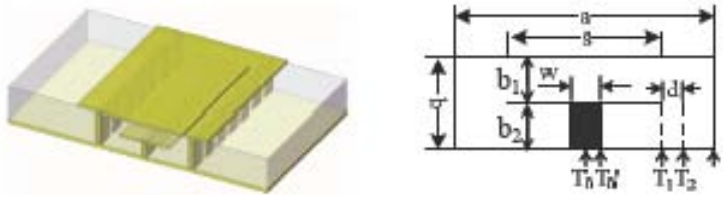

(c)

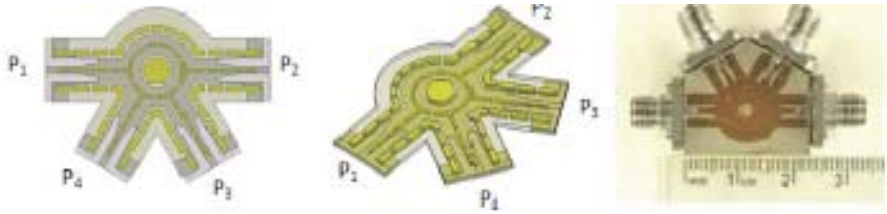

(d)

Fig. 1.2 (a) Microstrip to SIW transition through tapered ridged SIW section [67]. (b) H-plane SIW coupler and its HMSIW implementation, [65]. (c) Layout of TFSIW [69] and (d) TFSIW hybrid ring coupler [69].

1.6. BFNs using SIW Technology

In literature, several BFNs have been reported using SIW technology in both single-layer [70-75] and double-layer topologies [76]. This section gives a brief overview on each of these implementations.

Fig. 1.3 illustrates the post-wall waveguide single-layer Butler matrix reported by Shinichi et al. in [70]. The matrix employs the typical configuration of a 4x4 Butler matrix. The design employs hybrid H-plane directional couplers, cross couplers are used at the crossing arms locations and fixed phase shifts are achieved by varying the corresponding waveguides widths. The matrix was fabricated on a 3.2 mm thick Teflon substrate with a dielectric constant of 2.17, coaxial feed is used for the matrix excitation. The matrix is about 28mm wide and has a length that exceed 110mm for a narrowband performance around 26 GHz. Further improvements related to the same group was reported later in [71] to control the side lobe level but the circuit was not experimentally demonstrated.

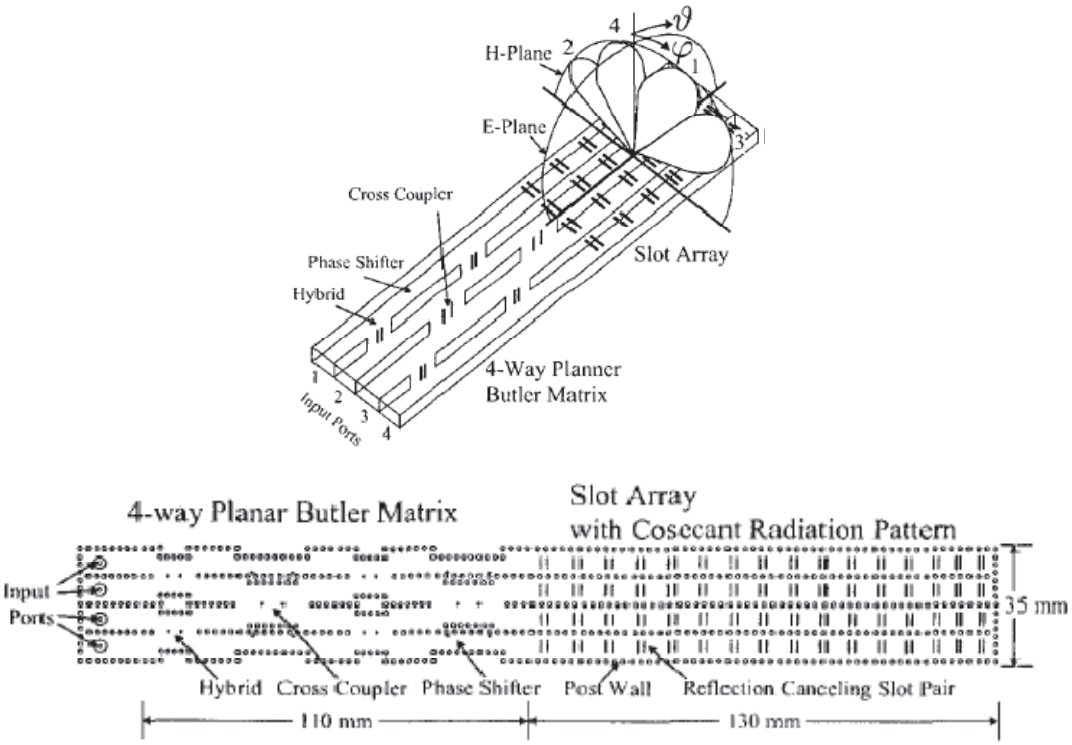

Fig. 1.3 Butler matrix with slot antenna array: 3-D waveguide view and corresponding planar via-hole arrangement [70].

In [72], Chen et al. presented a 24-beams slot array antenna constructed by six 4-beams single layer SIW antennas that integrate the design of six 4x8 modified Butler matrices to ensure a low side lobe level amplitude distribution. The block diagram of the 4x8 Butler matrix is shown in Fig. 1.4 together with the SIW multibeam antenna fed by the 4x8 matrix as reported in [72]. The multibeam antenna

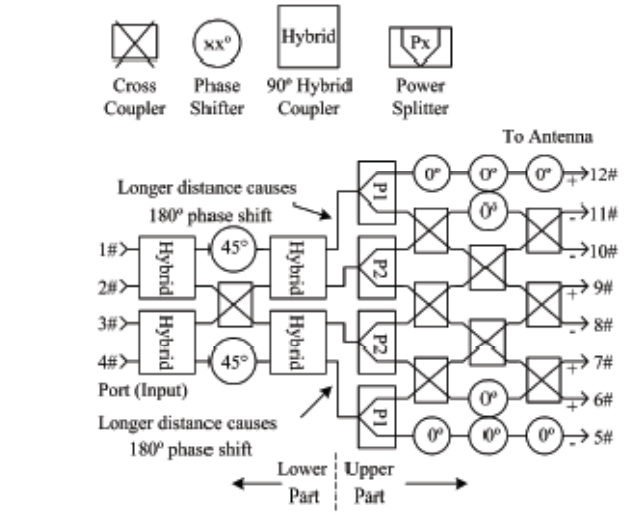

(a)

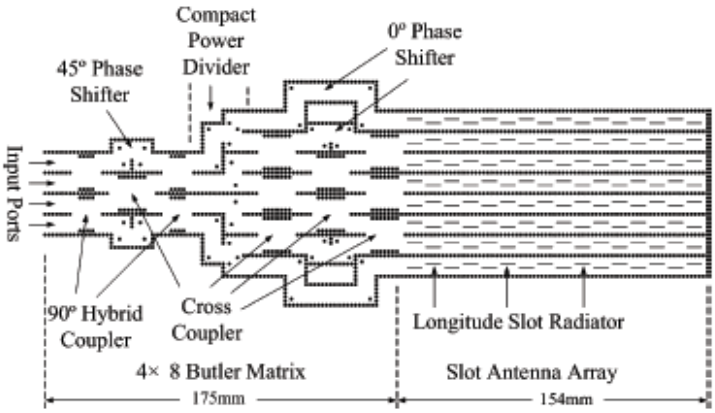

(b)

Fig. 1.4 (a) Block diagram of the 4x8 Butler matrix and (b) the corresponding SIW implementation feeding a slot antenna array, [72].

was realized on a Rogers 5880 substrate with thickness of 1.5748 mm and dielectric constant 2.2. The developed 4x8 matrix has a bandwidth defined by a reflection loss less than -14 dB over the 15.6-16.6 GHz frequency band with a 600 MHz usable bandwidth around 16 GHz with the restriction of a side lobe level lower than -10 dB.

The Rotman lens has also received an interest for SIW planar implementations where the input and output ports can be realized in SIW technology as well as the radiating elements [73, 74].

A novel multi-beam SIW Rotman lens in low-cost SIW technology has been reported by Sbarra et al. in [73] where a Ku-band lens prototype with three ports feeding an eight-element array has been demonstrated. Instead of using dummy ports with matched termination to avoid multiple reflections in the TEM parallel-plates

region, adsorbing sidewalls are proposed by appropriately drilling the lossy material to ensure the matching between the TEM and the drilled absorbing material. The matrix is illustrated in Fig. 1.5 with overall dimensions of 22cm x 16 cm. The circuit was implemented on a 1.575 mm thick Taconic substrate with relative permittivity of 2.5 with a 3.15mm thick lossy material with dielectric constant of 13.4. An overall efficiency around 30% has been reported. With good performances in terms of return loss, insertion loss and side lobe level.

Another relevant study on the SIW Butler matrix is the one reported by Cheng et al. in [74] for seven input beam ports and nine output array ports integrated with a slot antenna array implemented at 28.5 GHz. The dummy ports are exploited to suppress the side lobes for broadband operation in terms of the beam deviation angle with frequency. The structure was realized on a 0.508 mm thick Rogers substrate with relative permittivity of 2.2. Low amplitude ripple over the 27-30 GHz frequency band has been reported while the overall measured radiation efficiency remains below 57%. The developed multibeam antenna is shown in Fig. 1.6.

Fig. 1.5 3x8 SIW Rotman lens with perforated absorbing material [73].

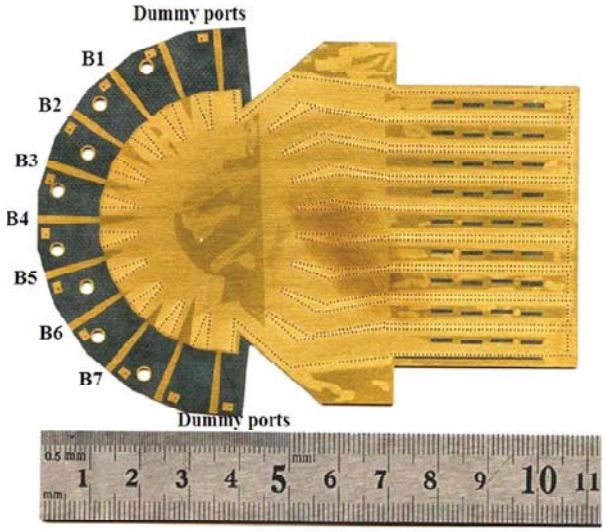

Fig. 1.6 SIW multibeam slot array antenna with 7x9 Rotman lens [74].

Implementation of single-layer Nolen matix in SIW technology has also been addressed. In [75], Djerafi et al. present a planar Ku-band Nolen matrix in SIW technology. The matrix consists of a cruciform SIW coupler previously developed by the same group [35], together with unequal length, variable width SIW phase shifters [32] in a single layer topology. The matrix offers very good characteristics at the design center frequency with respect to the reference theoretical values while phase dispersion has been investigated over 500 MHz around 12.5 GHz with respect to the beam squint angle. The circuit was realized on a 0.787mm thick Rogers substrate with relative permittivity of 2.33, the overall matrix dimensions are 13.7cm×10.5cm and is illustrated in Fig. 1.7.

The implementation of BFNs in double layer SIW topologies has also been addressed. In [76], Chen et al. proposed a double-layer 4x16 SIW Blass matrix at 16 GHz. The matrix employs SIW like cross couplers [77, 78] while the phase shifters are realized by extending the corresponding waveguide lengths that are bent into arcs. Characteristics of -12 dB side lobe level with matrix efficiency of 50% have been reported. The matrix structure is illustrated in Fig. 1.8 and was implemented on 0.508mm thick Rogers substrate with relative permittivity of 2.2.

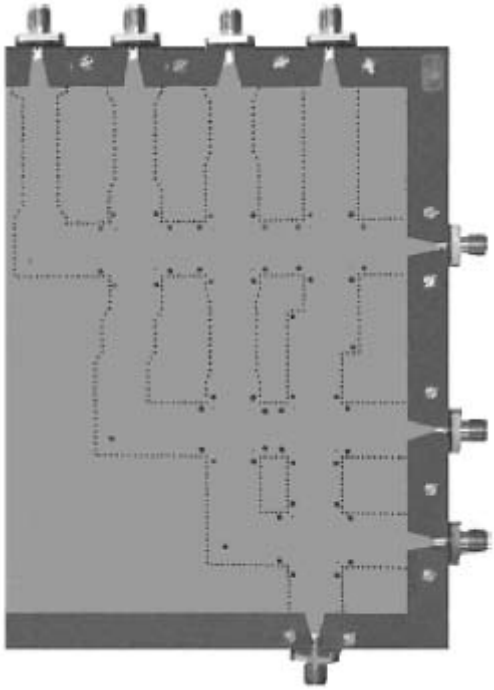

Fig. 1.7 Developed 4x4 SIW Nolen matrix of [75].

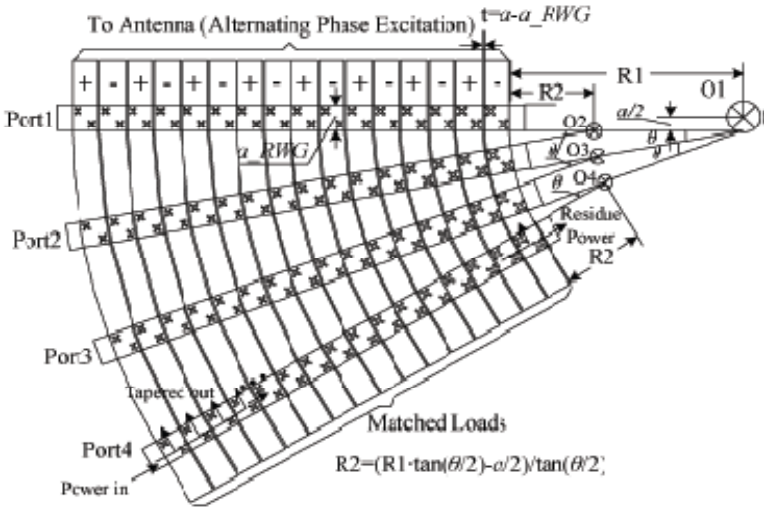

Fig. 1.8 Equivalent waveguide structure of the 4x16 Blass matrix [76].

1.7. Conclusion

In this chapter, the state of the art of beam forming matrices together with the substrate integrated waveguide technology has been presented. The chapter has started by describing the function of BFNs in nowadays wireless communication systems defining the required characteristics and performances, where several relevant works related to BFNs have been presented pointing out the advantage of each.

The SIW technology is an attractive candidate for BFNs and their related passive components. It provides the advantages of metallic waveguides in terms of high quality factor, good power handling capability, low loss, planar implementation while being compatible with low-cost standard PCB and LTCC technologies. No doubt that SIW technology is progressing everyday giving rise to attractive implementations of passive and active microwave components. Moreover, the design flexibility of SIW and the development of different transitions and interconnects in both single-layer and multi-layer topologies gave rise to a larger concept, namely the Substrate Integrated Circuit (SIC) introducing a new vision of System on Substrate (SoS). Several realizations for BFNs have been recently reported and briefly presented in this chapter.

In the following chapters, the multi-layer SIW technology will be explored to develop different novel passive components (couplers and phase shifters). Some of these newly developed components will be used to implement a two-layer compact 4×4 SIW Butler matrix offering wideband performances for both transmission magnitudes and phases with good isolation and input reflection characteristics.

References of Chapter One

[1] A. El-Zooghby, "Potentials of smart antennas in CDMA systems and uplink improvements," *IEEE Ant. Prop. Mag.*, Vol. 43, No. 5, pp.172-177, Oct. 2001.

[2] P. S. Hall and S. J. Vetterlein, "Review of radio frequency beamforming techniques for scanned and multiple beam antennas," *IEE proceedings*, Vol. 137, No. 5, pp. 293-303, 1990.

[3] B. Piovano, L. Accatino, A. Angelucci, T. Jones, P. Capece and M. Votta "Design and breadboarding of wideband NxN Butler matrices for multiport amplifiers," *Microw. Conf.*, Brazil, SBMO, pp. 175-180, 1993.

[4] J. Blass, Multi-directional antenna: New approach top stacked beams, *IRE Int. Convention Record*, Pt 1, 1960, pp 48-50.

[5] J. Nolen, "Synthesis of multiple beam networks for arbitrary illuminations," *Ph. D. Thesis*, Bendix Corporation, Radio Division, Baltimore, April 1965.

[6] W. Rotman and R. F. Tuner, "Wide-angle microwave lens for line source applications," *IEEE Trans. Ant. Propagat*., Vol. 11, pp. 623-632, 1963.

[7] J. Butler and R. Lowe, "Beam-forming matrix simplifies design of electrically scanned antennas," *Electron design*, pp. 170-173, 1961.

[8] C. Dall'Omo, T. Monediere, B. Jecko, F. Lamour, I wolk and M. Elkael, "Design and reslization of a 4x4 Microstrip Butler matrix without any crossing in millimeter waves," *Microw. Opt. Tech. Lett*., Vol. 38, No. 6, pp.462-465, Sep. 2003

[9] H. Hayashi, D.A. Hitko and C. G. Sodini, "Four-element planar butler matrix using half-wavelength open stubs," *IEEE Microw. Wireless Comp. Lett*., Vol. 12, No.3, Mar. 2002.

[10] F. Alessandri, M. Dionigi R. Sorrentino and L. Tarricone, "Rigorous and efficient fabrication-oriented CAD and optimization of complex waveguide networs," *IEEE Trans. Microw. Theory Tech.*, Vol. 45, No. 12, pp. 2366-2374, Dec. 1997.

[11] T. N. Kaifas and J. Sahalos, "On the design of a single-layer wideband butler matrix for switched-beam UMTS system applications," *IEEE Trans. Ant. Propagat*., Vol. 48, pp. 193-204, Dec. 2006.

[12] M. Bona, L. Manholm, J. P. Starski and B. Svensson, "Low-loss compact Butler matrix for a microstrip antenna," *IEEE Trans. Microw. Theory Tech*., Vol. 50, No.9, pp.2069-2075, Sep. 2002.

[13] M. Nedil, T. A. Denidi and L. Talbi, "Novel Butler matrix using CPW multilayer technology," *IEEE Trans. Microw. Theory Tech*., Vol. 54, No.1, pp.499-507, Jan. 2006.

[14] L. Accatino, F. Muoio, B. Piovano, G. Gaille and M. Mongiardo, "CAD of waveguide Butler matrices including mechanical and thermal constraints," *European Microw. Conf.*, pp.1-4, 2001.

[15] J. Hirokawa, F. Murukawa, K. Tsunekawa and N. Goto, " Double-layer structure of rectangular-waveguides for Butler matrix," *European Microw. Conf.*, pp.1-4, Milan, Oct. 2002.

[16] F. Shigeki, "Waveguide line," Japanes patent: JP 06 053711, 1994.

[17] A. Piloto, K. Leahy, B. Flanick and K. A. Zaki, "Waveguide filters having a layered dielectric structures," U.S. Patent: 5 382 931, Jan. 1995.

[18] M. Ando, J. Hirokawa, T. Yamamot, A. Akiyama, N. Kimura, Y. Kimura and N. Goto, "Novel single-layer waveguides for high-efficiency millimeter-wave arrays," *IEEE millimeter waves conference proceedings*, pp. 177-180, 1997.

[19] M. Ando, J. Hirokawa, T. Yamamot, A. Akiyama, N. Kimura, Y. Kimura and N. Goto, "Novel single-layer waveguides for high-efficiency millimeter-wave arrays," *IEEE Trans. Microw. Theory Tech*., Vol. 46, No.6, pp.792-799, June 1998.

[20] H. Uchimura, T. Takenoshita and M. Fuji, "Development of a "Laminated waveguide"," IEEE *Trans. on Microw. Theory Techn.*, Vol.46, No. 12, pp.2438-2443, Dec. 1998.

[21] D. Deslandes and K. Wu, "Integrated microstrip and rectangular waveguide in planar form," *IEEE Microwave Compon. Lett*., Vol. 11, pp. 68-70, Feb. 2001.

[22] D. Deslandes and K. Wu, "Integrated transition of coplanar to rectangular waveguides," IEEE MTT-S, pp.619-622, 2001.

[23] V. S. Mottonen and A. V. Raisanen, "Novel wide-band coplanar waveguide-to-rectangular waveguide transition," *IEEE Trans. Microw. Theory Tech*., Vol. 52, No.8, pp.1836-1842, Aug. 2004.

[24] S. Lee, S. Jung and H. Lee, "Ultra-wideband CPW-to-substrate integrated waveguide transition using an elevated-CPW section," *IEEE Microw. Wireless Comp. Lett.*, Vol. 18, No. 11, pp. 746-748, Nov. 2008.

[25] X. Chen and K. Wu, "Low-loss ultra-wideband transition between conductor-backed coplanar waveguide and substrate integrated waveguide," *IEEE MTT-S*, pp. 349-352, June 2009.

[26] H. J. Tang, W. Hong, Z. C. Hao, J. X. Chen, and K. Wu, "Optimal design of compact millimetre-wave SIW circular cavity filters," *Electronics Lett.*, 2005, Vol. 41, No. 19.

[27] X.-P. Chen, and K. Wu, "Substrate Integrated Waveguide cross coupled filter with negative coupling structure," *IEEE Trans. Microw. Theory Tech.*, Vol. 56, No. 1, pp. 142-149, 2008.

[28] Z. C. Hao, W. Hong, X. P. Chen, J. X. Chen, K. Wu, T. J. Cui, "Multilayered Substrate Integrated Waveguide (MSIW) elliptic filter," *IEEE Microw. Wireless Comp. Lett.*, Vol. 15, No. 2, pp. 95–97, 2005.

[29] Z. C. Hao, W. Hong, X. P. Chen, J. X. Chen, and K. Wu, "Compact super-wide bandpass Substrate Integrated Waveguide (SIW) filters," *IEEE Trans. Microw. Theory Tech.,* Vol. 53, No. 9, pp. 2968–2977, 2005.

[30] D. Stephens, P. R. Young and I. D. Robertson, "Millimeterwave substrate integrated waveguides and filters in photo imageable thick-film technology," *IEEE Trans. Microw. Theory Tech*., Vol. 53, No. 12, pp. 3832-3838, 2005.

[31] B. Potelon, J. Favennec, C. Quendo, E. Rius, C. Person and J. Bohorquez, "Design of a substrate integrated waveguide (SIW) filter using a novel topology of coupling," *IEEE Microw. Wireless Comp. Lett.*, Vol. 18, No. 9, pp. 596-598, Sept. 2008.

[32] Y. Cheng, W. Hong and K. Wu, "Novel Substrate Integrated Waveguide fixed phase shifter for 180-degree Directional Coupler," *IEEE MTT-S*, pp. 189-192, Honolulu, June 2007.

[33] Y. Cassivi, D. Deslandes and K. Wu, "Substrate integrated waveguide directional couplers," *Asia-Pacific Microw. Conf*., Nov. 2002.

[34] Z. C. Hao, W. Hong, J. X. Chen, H. X. Zhou, and K. Wu, "Single-layer substrate integrated waveguide directional couplers," *IEE Proc. Microw. Antennas Propagat.,* Vol. 153, No. 5, pp. 426–431, 2006.

[35] T. Djerafi and K. Wu, "Super-compact Substrate Integrated Waveguide cruciform directional coupler," *IEEE Microw. Wireless Comp. Lett*., Vol. 17, No. 11, pp. 757–759, 2007.

[36] Z. C. Hao, W. Hong, X. P. Chen, J. X. Chen, and K. Wu, "K. Planar diplexer for microwave integrated circuits," *IEE Proc. Microw. Antennas Propagat.*, Vol. 152, No. 6, pp. 455–459, 2005.

[37] H. J. Tang, W. Hong, J.-X. Chen, G. Q. Luo and K. Wu, "Development of millimeter-wave planar diplexers based on complementary characters of dual-mode substrate integrated waveguide filters with circular and elliptic cavities," *IEEE Trans. Microw. Theory Techn.,* Vol. 55, No. 4, pp. 776–782, 2007.

[38] X. Xu, R. G. Bosisio, and K. Wu, "A new six-port junction based on Substrate Integrated Waveguide technology," *IEEE Trans. Microw. Theory Techn.*, Vol. 53, No. 7, pp. 2267 – 2273, 2005.

[39] W. D'Orazio, K. WU and J. A. Helszajn, "Substrate integrated waveguide degree-2 circulator," *IEEE Microw. Wireless Comp. Lett*., Vol. 14, No. 5, pp. 207–209, 2004.

[40] W. D'Orazio, and K. Wu, "Substrate-integrated-waveguide circulators suitable for millimeter-wave integration," *IEEE Trans. Microw. Theory Techn*., Vol. 54, No. 10, pp. 3675-3680, 2006.

[41] L. Yan, W. Hong, G. Hua, J. Chen, K. Wu and T. J. Cui, "Simulation and experiment on SIW slot array antennas," *IEEE Microw. Wireless Comp. Lett*., Vol. 14, No. 9, pp. 446-448, 2004.

[42] D. Deslandes and K. Wu, "Substrate integrated waveguide leaky wave antenna: Concept and design considerations," *Asia-Pacific Microw. Conf*., Dec. 2005.

[43] Y. J. Cheng, W. Hong and K. Wu, " Design of a monopulse antenna using a Dual V-Type Linearly Tapered Slot Antenna (DVLTSA)," *IEEE Trans. Antennas Propagat.*, Vol. 56, No. 9, pp. 2903–2909, 2008.

[44] D. Kim, J. W. Lee, C. S. Cho and T. K. Lee, "X-band circular ring-slot antenna embedded in single-layered SIW for circular polarization," *Electron. Lett*., Vol. 45, No. 13, June 2009.

[45] J. Bohorquez, H. Pedraza, I. Pinzon, J. Castiblanco, N. Pena and H. Guarizo, "Planar substrate integrated waveguide cavity-backed antenna," *IEEE Antennas Wireless Prop. Lett.*, Vol. 8, pp. 1139-1142, 2009.

[46] K. Kuhlmann, K. Rezer and A. Jacob, "Far field measurement on Ka-band substrate-integrated waveguide antenna array with polarization multiplexing," *IEEE MTT-S*, pp.1337-1340, June 2008.

[47] Y. Cassivi and K. Wu, "Low cost microwave oscillator using substrate integrated waveguide cavity," *IEEE Microw. Wireless Comp. Lett*., Vol. 13, No. 2, pp. 48 – 50, 2003.

[48] C. Zhong, J. Xu, Z. Yu and Y. Zhu, "Ka-Band Substrate Integrated Waveguide Gunn Oscillator," *IEEE Microw. Wireless Comp. Lett*., Vol. 18, No. 7, pp. 461–463, Jul. 2008.

[49] J.-X. Chen, W. Hong, Z.-C. Hao, H. Li and K. Wu, "Development of a low cost microwave mixer using a broad-band Substrate Integrated Waveguide (SIW) coupler," *IEEE Microw. Wireless Comp. Lett*., Vol. 16, No. 2, 2006.

[50] H. Jin, G. Wen, "A novel four-way Ka-band spatial power combiner based on HMSIW," *IEEE Microw. Wireless Comp. Lett*., Vol. 18, No. 8, pp. 515-517, 2008.

[51] M. Abdolhamidi, M. Shahabadi, "X-band substrate integrated waveguide amplifier," *IEEE Microw. Wireless Comp. Lett. ,* Vol. 18, No. 12, pp. 815-817, 2008.

[52] Y. Cassivi, L. Perregrini, P. Arcioni, M. Bressan, K. Wu, G. Conciauro, "Dispersion characteristics of substrate integrated rectangular waveguide," IEEE *Microw. Wireless Comp. Lett.*, Vol. 12, No. 9, pp. 333-335, 2002.

[53] F. Xu, Y. Zhang, W. Hong, K. Wu, T. J. Cui, "Finite difference frequency-domain algorithm for modeling guided-wave properties of substrate integrated waveguide," *IEEE Trans. Microw. Theory Techn*., Vol. 51, No. 11, pp. 2221-2227, 2003.

[54] L. Yan, W. Hong, K. Wu, and T. J. Cui, "Investigations on the propagation characteristics of the substrate integrated waveguide based on the method of lines," *Proc. IEE Microw. Antennas Propagat.*, Vol. 152, pp. 35–42, 2005.

[55] F. Xu, K. Wu and W. Hong, "Domain decomposition FDTD algorithm combined with numerical TL calibration technique and its application in parameter extraction of substrate integrated circuits," *IEEE Trans. Microw. Theory Techn.*, Vol. 54,No. 1, pp. 329-338, 2006.

[56] M. Bozzi, L. Perregrini and K. Wu, "Modeling of conductor, dielectric and radiation losses in substrate integrated waveguide by the boundary integral-resonant mode expansion method," *IEEE Trans. Microw. Theory Techn.*, Vol. 56, No. 12, pp. 3153-3161, 2008.

[57] F. Xu and K. Wu, "Guided-wave and leakage characteristics of substrate integrated waveguide," *IEEE Trans. Microw. Theory Tech.*, Vol. 53, No. 1, pp. 66-73, Jan. 2005.

[58] D. Deslandes and K. Wu, "Design consideration and performance analysis of substrate integrated waveguide components," *Europ. Microw. Conf.*, pp.1-4, Oct. 2002.

[59] K. Wu, D. Deslandes and Y. Cassivi, "The substrate integrated circuits- a new concept for high-frequency electronics and optoelectronics," *Microwave Review*, pp.2-9, Dec. 2003.

[60] N. Grigoropoulos and P. R; Young, "Compact folded waveguides," *Europ. Microw. Conf.*, pp.973-976, 2004.

[61] G. Mazumder and P. Saha, "Rectangular waveguide with T-shaped septa," *IEEE Trans. Microw. Theory Techn.*, Vol. 35, pp. 201-204, Feb. 1987.

[62] Y. Zhang and W. Joines, "Some properties of T-septum waveguides," *IEEE Trans. Microw. Theory Techn.*, Vol. 35, pp. 769-775, Aug. 1987.

[63] N. Grigoropoulos, B. Izquierdo and P. R. Young, "Substrate integrated folded waveguides (SIFW) and filters," *IEEE Microw. Wireless Comp. Lett.*, Vol. 15, No. 12, pp.829-831, Dec. 2005.

[64] B. Izqueirdo,N. Grigoropoulos and P. Young, "Ultra-wideband multilayer substrate integrated folded waveguides," *IEEE MTT-S*, pp. 610-612, 2006.

[65] B. Liu, W. Hong, Y. Q. Wang, Q. H. Lai and K. Wu, "Half mode substrate integrated waveguide (HMSIW) 3dB coupler," *IEEE Microw. Wireless Comp. Lett.*, Vol. 17, No. 1, pp.22-24, Jan.2007.

[66] G. Zhai, W. Hong, J. Chen, P. Chen and H. Tang, "Half mode substrate integrated waveguide 3dB coupler," *IEEE Microw. Wireless Comp. Lett.*, Vol. 18, No. 12, pp.829-831, Aug. 2008.

[67] Y. Ding and K. Wu, "Substrate integrated waveguide-to-microstrip transition in multilayer substrate," *IEEE MTT-S*, pp. 1555-1558, June 2007.

[68] Y. Ding and K. Wu, “Miniaturization techniques of substrate integrated waveguide circuits,” *IEEE MTT-S*, pp.63-66, June 2008.

[69] Y. Ding and K. Wu, “Miniaturized hybrid ring circuits using T-type folded substrate integrated waveguide (TFSIW),” *IEEE MTT-S*, pp. 705-708, June 2009.

[70] S. Yamamoto, J. Hirokawa and M. Ando, “A beam switching slot array with a 4-way Butler matrix installed in a single layer post-wall waveguide,” *IEEE Antenna Propagat. Symp.*, pp. 138-141, June 2002.

[71] K. Morimoto, J. Hirokawa and M. Ando, “Design of a 180-degree single-layer divider to control sidelobe and crossover levels in Butler-matrix beam-switching antenna,” *Asia Pac. Microw. Conf.*, pp.1-4, Dec. 2007.

[72] P. Chen, Z. Kuai, J. Xu, H. Wang, J. Chen, H. Tang, J. Zhou and K. Wu, “A multibeam antenna based on substrate integrated waveguide technology for MIMO wireless communications,” *IEEE Antenna Propagat. Trans.*, Vol. 57, No. 6, pp. 1813-1821, June 2009.

[73] E. Sbarra, L. Marcaccioli, R. Gatti and R. Sorrentino, “A novel Rotman lens in SIW technology,” *Europ. Microw. Conf.*, pp. 1515-1518, Oct. 2007.

[74] Y.Cheng, W. Hong, K. Wu, Z. Kuai, C. Yu, J. Chen, J. Zhou, and H. Tang, “Substrate integrated waveguide (SIW) Rotman lens and its Ka-band multibeam array antenna applications,” *IEEE Antenna Propagat*. Trans., Vol. 56, No. 8, pp. 2504-2513, Aug. 2008.

[75] T. Djerafi, N. Fonseca and K. Wu, “Planar Ku-band 4×4 Nolen matrix in SIW technology,” *IEEE Trans. Microw. Theory Tech.*, Vol. 58, No. 2, pp. 259-266, Feb. 2010.

[76] P. Chen, W. Hong, Z. Kuai and J. Xu, “A double layer substrate integrated waveguide Blass matrix for beamforming applications,” *IEEE Microw. Wireless Comp. Lett.*, Vol. 19, No. 6, pp.374-376, June 2009.

[77] P. Meyer and. J. C. Kruger, “P. Meyer and J. C. Kruger, “Wideband crossed-guide waveguide directional couplers,” *IEEE MTT-S Int. Digest*, Vol. 1, pp.253–256, June 1998”

[78] P. Chen, G. Hua, D. Chen, Y. Wei and W. Hong, “A double layer crossed over substrate integrated waveguide wide band directional coupler,” *Asia Pac. Microw. Conf.*, pp. 1-4, Dec. 2008.

CHAPTER TWO

Multi-Layer Wideband SIW Phase Shifters

2.1. Introduction

Phase shifters are crucial components in microwave and millimeter-wave systems. Many research works have been focused on the development of fixed phase shifters featuring interesting characteristics in terms of arbitrary well-controlled differential phase shifts while maintaining low insertion loss and ease of integration. Such characteristics are major design constraints for phase shifters employed in beam-forming matrices. For such matrices when used to feed an antenna array, a well-controlled design for the phase dispersive characteristics, according to the adopted matrix configuration, is a key element in controlling and/or compensating the main beam squint.

One of the most famous wideband phase shifters is the Schiffman's differential phase shifter which was originally based on the coupled-strip transmission lines [1], designed also in microstrip form [2]. Another well-known technique is the stub-loading technique which can also achieve wideband relative phase shifts with low insertion losses [3]. Recently, some SIW phase shifters have been implemented based on different techniques, including the basic frequency dependent delay line [4] and inserted metallic posts [5]. However, these techniques suffer from poor dispersive phase characteristics and increased insertion loss. Another SIW-based promising implementation is realized by implementing different SIW sections and realizing the phase shift by simply varying their relative widths while maintaining the same length [6]-[8].

This chapter focuses on the development of novel waveguide-based structures suitable for the implementation of wideband phase shifters in SIW technology. Different structures are proposed and studied seeking the best candidate in terms of wideband performance, low insertion loss and ease of fabrication and integration within the foreseen beam-forming matrix. The chapter is organized as follows; Section 2.2 addresses the design of a novel waveguide-based Composite Right/Left Handed (CRLH) structure suitable for the implementation of wideband SIW phase shifters. Section 2.3.1 presents briefly the unequal width, equal length SIW phase shifters. Section 2.3.2 focuses on the development of multi-layered compensated-length, variable width SIW phase shifters based on an equivalent circuit model analysis of a developed novel low-loss two-layer E-plane SIW transition. Finally, conclusions are outlined in Section 2.4.

2.2. Composite Right/Left-Handed Phase-Shifter

2.2.1. Introduction

The first theoretical investigations for materials having simultaneous negative permittivity and permeability refer to the late 1960's [9]. However, it is only three decades later that these Left Handed (LH) meta-materials started to get growing attention owing to the leading experimental verifications demonstrated in [10]-[13].
In 2002, the transmission line approach to design LH material has been introduced, almost simultaneously, by three different groups [14]-[17], leading therefore to the Composite Right-Left Handed (CRLH) concept as a practical method to synthesize artificial meta-materials.

Different applications have been reported based on the CRLH propagation concept. In literature, two basic implementations for the artificial CRLH-TL can be identified. The best results in terms of low insertion losses and weak dispersion characteristics is the straightforward implementation using lumped elements with surface mount technology. Such applications include novel dual-band branch line coupler and ring resonator coupler employing quarter wavelength CRLH-TLs [18]. A compact broad-band hybrid ring including lumped element-based CRLH-TL has been demonstrated in [19]. Another well-known implementation for CRLH-TLs is based on microstrip, or coplanar waveguide, quasi-lumped implementation of the left-handed shunt inductance and series capacitance. A famous CRLH cell based on a

series interdigital capacitor and shunt shorted-stub inductor has been proposed by Caloz and Itoh in [20], and used in different applications, e.g. [21]. Other architectures for CRLH-TLs can also be found, such as in [22], where a miniaturized multi-layer TL is developed based on an original implementation for the CRLH cell which can be explored for numerous microwave applications.

In this section, a novel compact CRLH phase shifter is presented in a waveguide-based structure [23]. The proposed structure is suitable for the implementation using SIW technology. Related phase shifters are found in literature using other technologies [24]- [26], while analogous structures have been reported, shortly later, by two other groups [27], [28]. In this section, the design procedure through an eight-cell CRLH waveguide structure is first presented. Then the effect of varying the LH parameters is investigated by full-wave simulation results using HFSS. The simulation results revealed that the change in the left handed propagation parameters provide a well-controlled wideband arbitrary phase shift up to 270° over 5 GHz bandwidth centered at 18.5 GHz with insertion loss better than -2 dB over the entire band.

2.2.2. CRLH Transmission Line

This section gives a brief overview of the main characteristics of CRLH-TL propagation that will be used in the design procedure in the following section [29]. The infinitesimal circuit models for purely lossless RH and LH-TLs are shown in Fig. 2.1 (a) and (b), respectively. The purely LH TL is in fact the dual of the RH-TL with a series LH capacitance C_L and a shunt LH inductance L_L. In practical realizations, a pure LH structure is not possible due to the existence of the unavoidable series inductance and/or the shunt capacitance. Consequently, a practical CRLH-TL is artificially obtained by periodically loading a right handed propagation medium by the LH components in the form of lumped or quasi-lumped elements. Fig. 2.1(c) shows the infinitesimal circuit model for the practical CRLH unit cell. Fig. 2.1 (d), which is equivalent to that of Fig. 2.1 (a) in the balanced case condition, will be used to provide a direct physical insight for the CRLH-TL characteristics.

The propagation constant $\beta(\omega)$ is given by:

$$\gamma = j\beta = \sqrt{Z'Y'} \tag{2.1}$$

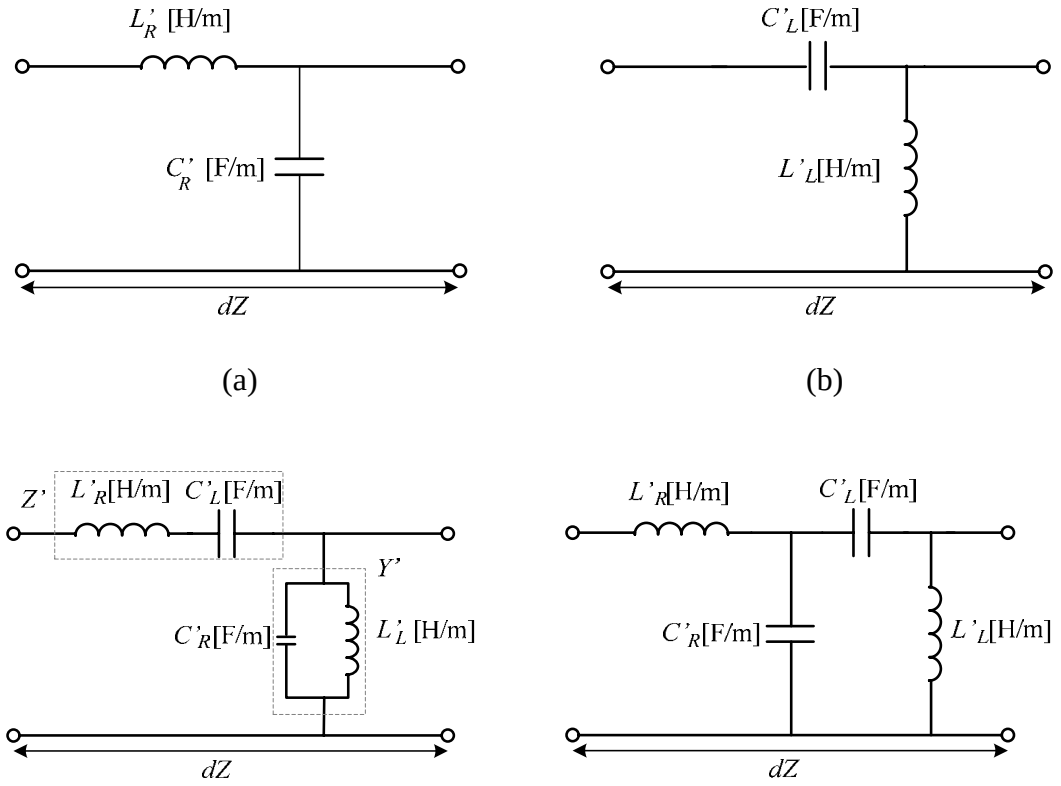

Fig. 2.1 Infinitesimal, lossless circuit models. (a) Purely RH TL. (b) Purely LH TL. (c) Ideal CRLH TL cell. (d) Equivalent CRLH cell for the balanced case.

where Z' and Y' are the per-unit length impedance and admittance, respectively and are given by:

$$Z' = j\omega L'_R + \frac{1}{j\omega C'_L} \qquad Y' = j\omega C'_R + \frac{1}{j\omega L'_L} \tag{2.2}$$

Therefore, β is given by

$$\beta = s(\omega)\sqrt{\omega^2 L'_R C'_R + \frac{1}{\omega^2 L'_L C'_L} - \left(\frac{L'_R}{L'_L} + \frac{C'_R}{C'_L}\right)} \tag{2.3}$$

where

$$s(\omega) = \begin{cases} -1, & if\ \omega < \omega_{\Gamma 1} = \min\left(\dfrac{1}{\sqrt{L'_R C'_L}}, \dfrac{1}{\sqrt{L'_L C'_R}}\right) \\ +1, & if\ \omega > \omega_{\Gamma 2} = \max\left(\dfrac{1}{\sqrt{L'_R C'_L}}, \dfrac{1}{\sqrt{L'_L C'_R}}\right) \end{cases} \tag{2.4}$$

For the balanced case, given by (2.5), (2.3) simplifies to:

$$L'_R C'_L = L'_L C'_R = L'C' \tag{2.5}$$

$$\beta = s(\omega)\sqrt{\omega^2 L'C' + \frac{1}{\omega^2 L'C'} - 2} = \omega\sqrt{L'C'} - \frac{1}{\omega\sqrt{L'C'}} \tag{2.6}$$

The phase constant β of Eq. (2.3) illustrates the double nature of the CRLH-TL. At low frequencies, the line is dominantly LH while at high frequencies it tends to be purely RH. The presence or absence of transmission gaps for the transition region from the LH to the RH propagation is evaluated based on determining whether there is a balanced or unbalanced condition. The balanced condition is characterized by a complete transmission of energy between the LH and RH ranges, thus a purely real β, which is obtained when the condition given by Eq. (2.5) is satisfied. The propagation constant of Eq. (2.6) clearly verifies the equivalence of the equivalent circuit of Fig. 2.1 (d) to that of Fig. 2.1 (c) under the balanced condition of Eq. (2.5). The unbalanced case is therefore obtained when $L_R'C_L' \neq L_L'C_R'$ for which β become imaginary over some frequency ranges as the radicand in Eq. (2.3) becomes negative, which introduces a stopband or a gap in the transition region. The transition frequency ω_o between the LH and RH ranges is obtained at β=0 and is given by:

$$\omega_0 = \frac{1}{\sqrt[4]{\left(L'_R\Delta z\right)\left(C'_R\Delta z\right)\left(\frac{L'_L}{\Delta z}\right)\left(\frac{C'_L}{\Delta z}\right)}} = \frac{1}{\sqrt[4]{L_R C_R L_L C_L}} \overset{balanced}{=} \frac{1}{\sqrt{LC}} \tag{2.7}$$

On the other hand, it has to be noted that, for the theoretical case of infinitely periodic RH and LH-TLs, the artificial CRLH of Fig. 2.1 (c) is a bandpass filter with a stopband from DC to the LH cutoff frequency F_{cR} and a stopband from the *RH* cutoff frequency F_{cR} to ∞, approximate expressions for F_{cL} and F_{cR} are given by Eq. (2.8) and Eq. (2.9), respectively.

$$F_{cL} = \frac{1}{4\pi\sqrt{L_L C_L}} \tag{2.8}$$

$$F_{cR} = \frac{1}{\pi\sqrt{L_R C_R}} \tag{2.9}$$

2.2.3. CRLH Phase Shifter: Structure and Design Considerations

Fig. 2.2 shows the developed novel waveguide-based CRLH structure for the case of symmetric eight cells. It consists of a rectangular waveguide, above cutoff, in which the LH shunt impedance L_L is realized by means of shunt inductive windows while the LH series capacitance C_L is the parallel equivalent of the capacitance due to the coupling between the successive metallic plates of the inductive windows and that introduced by transverse narrow slots in the waveguide broad wall placed in the center of each cell. The reactance X of the inductive widows is given by [30]:

$$\frac{X}{Z_o} \cong \frac{2a}{\lambda_g} \frac{\alpha^2}{0.429(1.56\alpha^2)(1-6.75\alpha^2 Q)+0.571(1-0.58\alpha^2)\sqrt{1-(2a_w/\lambda_g)^2}} \tag{2.10}$$

where a and a_w are the waveguide and the inductive window widths respectively, α and Q are given by

$$Q = 1-\sqrt{1-(\frac{2a}{3\lambda_g})^2}, \quad \alpha = \frac{a_w}{a} \tag{2.11}$$

The transverse slots have to be very narrow to minimize the surface conduction current perturbation on the waveguide broad wall, minimizing therefore the insertion loss. Moreover, the slots' length is chosen less than or equal to $a_w/2$ to minimize their series inductive effect due to the electric current rotation around them. The cell size dz between two successive windows is chosen in the order of $\lambda_g/10$ for the lowest operating frequency. The waveguide sections of length d on Fig. 2.2 are added to make sure that the evanescent modes, created at the discontinuity level, do not reach the excitation ports.

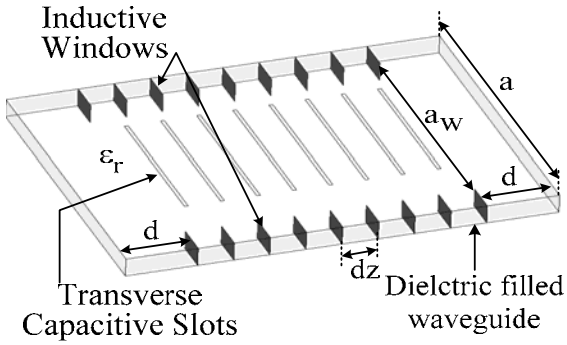

(a)

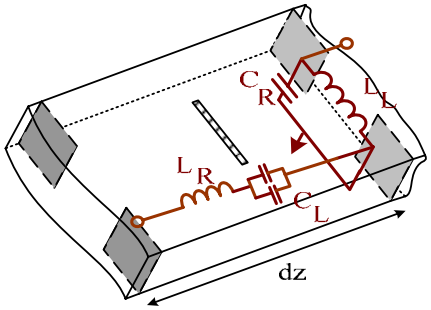

(b)

Fig. 2.2 (a) Layout of the developed waveguide-based CRLH structure (eight cells) (b) Layout of the unit cell of (b) with the equivalent circuit model.

The design procedure for the suggested phase shifter is based on a two-fold approach. First, the bandpass filter characteristics associated with the CRLH-TL propagation are determined such that the LH high pass and the RH low pass cutoff frequencies, F_{cL} and F_{cR} , respectively, bound the required frequency band in balanced-case propagation. This is done using a Matlab program by setting the values of F_{cL}, the transition frequency F_o between LH and RH propagations, ε_r, a and the RH impedance Z_{oR}. Z_{oR} is the waveguide characteristic impedance which is evaluated according to the power-voltage definition of Eq. (2.12), [30].

To force the balanced case to avoid gaps within the passband, Z_L is chosen equal to the RH impedance (Z_{oR}) evaluated at F_o. The used balanced condition is given by Eq. (2.5). Detailed expressions for F_{cL}, F_{cR} and F_o are given in Eqs. (2.7)-(2.9), from which Eq. (2.13) can be directly derived, to calculate C_L and L_L.

a_w is then calculated to synthesize a starting value for the required L_L using Eq. (2.10). All parameters are then optimized using HFSS with the previously calculated starting values to satisfy the balanced condition with the minimum

insertion loss while respecting that *dz* remains electrically small to maintain the validity of the used design equations.

Second, to achieve an arbitrary relative phase shift between different structures, the LH parameters are slightly modified. Since the left handed capacitance C_L is the parallel equivalent of two capacitances, it is more convenient to vary L_L by choosing different adjacent values of F_o and consequently F_{cL}. Then, the required phase shift ($\Delta\phi$) is obtained by comparing the different phase delays ($\phi(L_L, d)$) and choosing an appropriate reference length (d) as given by Eq. (2.14).

$$Z_{0R} = 2\sqrt{\frac{\mu}{\varepsilon}}\left(\frac{h}{a}\right);$$
$$L'_R = \mu\frac{Z_0}{\eta}, \quad C'_R = \varepsilon\frac{\eta}{Z_0}\left(1-\left(\frac{F_c}{F}\right)^2\right) \tag{2.12}$$

$$C_L = \frac{1}{4\pi Z_L}F_{cL} \tag{2.13}$$

$$\Delta\phi(F) = \phi(F, L_{L1}, d_1) - \phi(F, L_{L2}, d_2), \qquad F_{cL} < F < F_{cR} \tag{2.14}$$

2.2.4. Simulation Results

Based on the structure in Fig. 2.2 and the design procedure demonstrated in the previous section, an eight-cell phase shifter is designed and optimized. For all simulations, the structure is designed on a 0.762 mm thick Neltec NY9208 substrate with ε_r = 2.08, and the waveguide width a = 9.5 mm. The capacitive slots length is maintained half the waveguide width, with a wall thickness of 0.2mm, and their width is equal to 50 µm while *dz* is fixed to 2 mm. a_w and d are changed to satisfy arbitrary phase differences according to Eq. (2.14).

Fig. 2.3 shows the simulated S-parameters and transmission phase for the optimized eight-cell structure in the balanced case with a_w=6.5 mm and d=6mm. The band-pass filter response is clearly achieved with a -3 dB pass-band between 15.2 and 19 GHz and a sharp transmission zero at 27.5 GHz. The balanced condition is also quite satisfied with F_o (identified by the 0° phase shift in the de-embedded case)

almost equals to the geometric mean of the two later frequencies. The return loss is higher than 2 dB over the entire band and is due to the radiation losses by the transverse slots and the mismatch between Z_L and Z_{oR} due to the dispersive nature of Z_{oR} as well as the LH parameters.

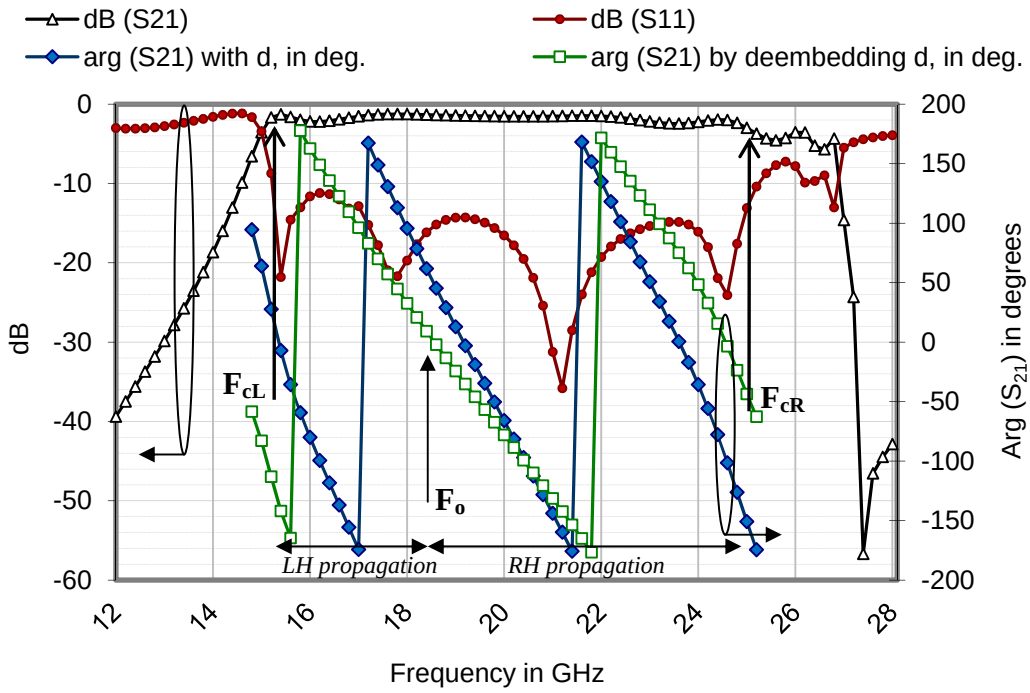

Fig. 2.3 Simulated S-parameters for the eight-cell structure of Fig. 2.1 with the transmission phase within the passband before and after de-embedding *d*, *d*=6mm.

Table 2.1 summarizes the different values of a_w and d with the associated simulation results for F_{cL}, F_o. F_{cR} and the sharp transmission zero values remain almost the same as that of Fig. 2.3. Fig. 2.4 shows the transmission phase curves for the common pass band between the different structures of Table 2.1. It can be seen from the results of Table 2.1 and Fig. 2.4 that a wideband arbitrary phase shift can be achieved over the frequency range from 16 GHz up to 21 GHz (the TE_{20} mode starts to propagate at 22 GHz) with phase curves having almost the same slope. The maximum achievable phase shift dynamic range is actually decided by (2.14) according to the maximum and minimum L_L values. While the minimum achievable phase shift will be rather controlled by the minimum step in the a_w variations which is governed by the technology. SIW technology with the selected substrate thickness can achieve 100 µm via-holes diameter with 200µm pitch size. It has to be noted that

further improvement in the relative phase slopes of Fig.2.4 can be achieved by adding *a* as a variable parameter to Eq. (2.14) and re-optimizing the structure.

Table 2.1. Parameters and simulation results for six different structures of Fig. 2.2 with the same length of the CRLH part and different values of a_w and *d*.

Structure No.	**1**	**2**	**3**	**4**
a_w **mm**	6.5	7.25	8.25	8.5
F_{cL} **GHz**	15.25	13.8	12.4	12.0
F_o **GHz**	19	17.6	16.6	16.4
d **mm**	6	8.1	9.1	9.35

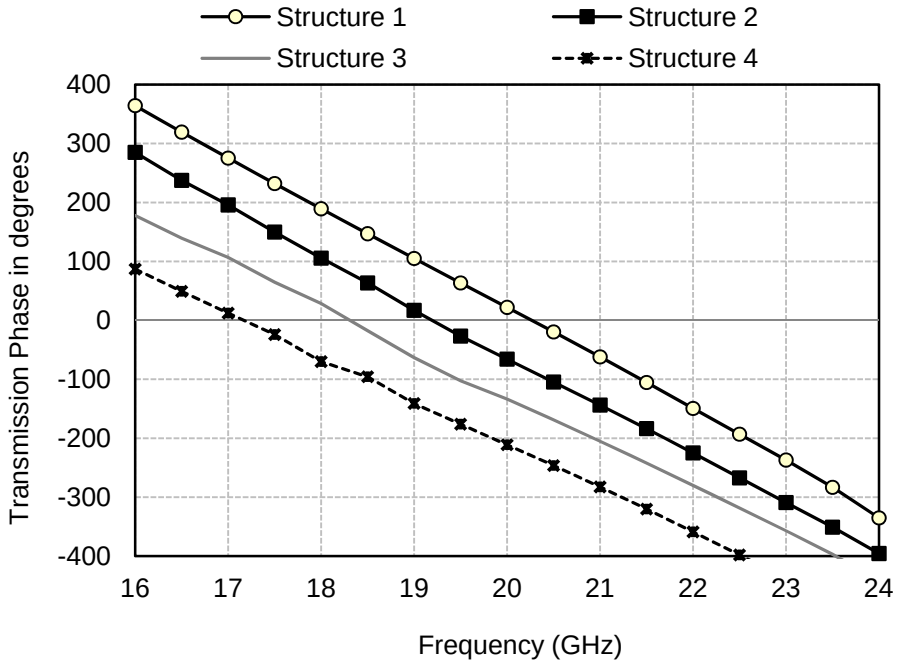

Fig. 2.4 Simulated results for phase shifts of the structures of Table 2.1.

2.2.5. Conclusion

In this section, a novel compact waveguide-based CRLH structure has been presented. The structure is suitable for compact phase shifter applications in SIW technology. A simple design procedure has been presented and verified by the simulation results based on the balanced CRL-TL equivalent circuit model. An eight-

cell structure has been designed and optimized offering up to 270° phase shift with a wideband performance over the frequency band (16 - 21 GHz).

Further improvement in the phase shifter characteristics can be obtained by adding the waveguide width as an optimization variable. The radiation losses through the transverse capacitive slots can also be reduced by employing a thin stacked substrate with metallic patches above the slots. The insertion losses of the proposed structure are within the same order of the semi-lumped implementations of CRLH structures. However, regarding these return loss values (~2 dB), beside the related technological aspect for SIW realization, this structure would not be the best candidate to be integrated in larger sub-systems as the beam-forming matrices.

2.3. Multi-Layer, Variable Width, Wideband Phase Shifter

2.3.1. Single Layer, Variable Width Phase Shifter

Equal length, unequal width SIW phase shifters have been introduced in 2007, by Wu et al. and shortly later by Sorrentino et al., and Ando et al., in [6]-[8], respectively. In this type of phase shifters, to achieve a specific phase difference ($\Delta\phi$) between two waveguide sections having the same length (l), the propagation constant (β) is modified by varying the corresponding widths accordingly, Fig. 2.5.

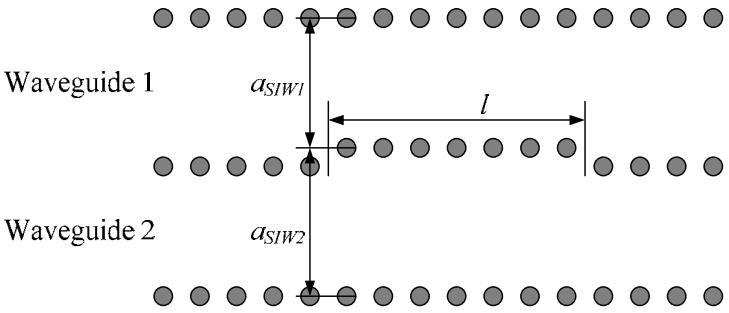

Fig. 2.5 Equal length, variable width SIW phase shifter configuration.

As a matter of fact, for rectangular waveguides and their SIW equivalent, the wider the width of the waveguide is, the higher value of the propagation constant β will be obtained at the same frequency. Therefore, the wave will propagate slower in

the wider waveguide achieving a phase delay with respect to the narrower one, which is given by Eq. (2.15).

$$\frac{\Delta\phi}{l} = \frac{\phi_1 - \phi_2}{l} = \beta_1 - \beta_2 = \sqrt{\left(\frac{2\pi}{\lambda}\right)^2 - \left(\frac{1}{a_2}\right)^2} \tag{2.15}$$

As the SIW is accurately synthesised in planar substrates, besides its flexibility in the design of low-loss curvatures and bends [31], this principle is easily realized in SIW technology for fixed phase shifters. By properly choosing the different values of the waveguides widths, the corresponding propagation factor curves are nearly parallel. A wideband phase shift can thus be obtained with a large phase shift dynamic range.

It has to be noted that the waveguide width variations of Eq. (2.15) are subject to two major constraints. First, they must ensure the fundamental mode propagation for a common frequency band corresponding to the band of interest. Second, the variations of these waveguides widths are naturally associated with impedance variations. These impedance variations result in a mismatch loss due to the change in the SIW widths. From Eq. (2.15), as the relative phase shift is normalised with respect to the common part of length (l) (Fig. 2.15), a compromise between the overall length (l) and the reflection loss can be obtained. This is done by employing small progressive variations in the waveguide width along relatively longer length (l) seeking minimum reflection losses with wideband performance. Therefore, the larger the required ($\Delta\phi$), the longer (l) would be.

Fig.2.6 illustrates an example of the differential phase shifts between different equal-length, unequal-width SIW sections. The designed phase shifters are optimized to ensure phase shifts of -45^o, -90^o, -135^o and -180^o when compared to a reference SIW section of the same length, at 12.5 GHz. The widths of these waveguides in SIW technology are 10.328, 10.7, 11.115 and 11.85 mm, respectively, with a reference 10.1 mm wide SIW section. The SIW sections of Fig. 2.6 have been designed on 0.762 mm thick substrate with relative permittivity of 2.08 and tan (δ) =6x10^{-4}. The SIW parameters are such that the via-hole diameter is 0.5 mm with a pitch size of 0.95 mm, while all SIW sections have the same length of 37.55 mm. It can be seen that these phase shifts are quite satisfied in the frequency band of 12 GHz to 13 GHz. The maximum phase error is of -1.3°, -4.9°, -6.8° and -12° for the

previously mentioned four phase shift values, respectively, over the required frequency range. Phase compensation is therefore needed to ensure better dispersive characteristics over wider frequency bandwidths.

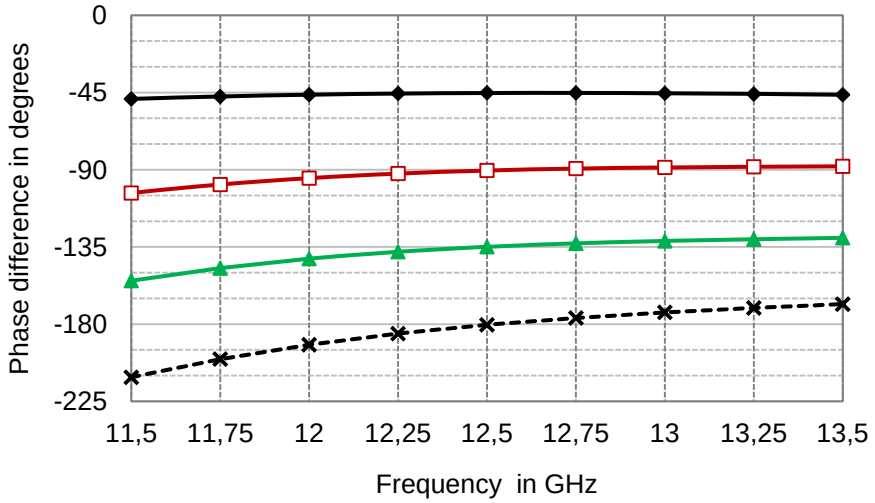

Fig. 2.6 Simulated results for differential phase shifts between different single-layer SIW sections with equal-length and variable-widths.

2.3.2. Multi-Layer, Variable Width Phase Shifter

This section deals with variable width, compensated length phase shifters in multi-layer topologies. First, a novel two-layer, low-loss SIW transition is introduced. This transition will be used together with SIW sections for the implementation of low-loss, two-layer phase shifters suitable for the implementation of two-layer beam-forming matrices, particularly the Butler matrix where path crossings can be avoided using such a transition. The transition is also exploited to develop a variable-width, compensated-length wideband phase shifter in a three-layer topology. This will be illustrated in details in the following sections.

2.3.2.1. Two-Layer SIW Transition

In this section, a novel two-layer SIW transition is presented. The transition is used as a low-loss connecting structure between two short-ended SIW sections in two different stacked substrate layers. Such a transition can be used in microwave components and sub-systems having multi-layered architectures. To identify the

phase characteristics as well as the insertion loss associated with the transition, the transition is analyzed based on the wide-band equivalent circuit model of [32].

Fig. 2.7 shows the structure of the two-level transition. The transition consists of two waveguides sharing a common broad wall with a narrow transverse coupling slot. The slot is bounded by two shorting walls at distances d_1 and d_2, from the slot center, each wall shorts its corresponding waveguide section.

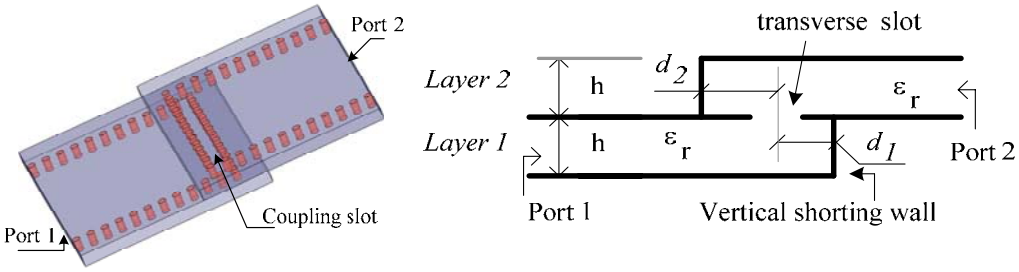

(a) (b)

Fig. 2.7 Two layer transverse slot-coupled waveguide transition.
(a) 3-D SIW structure. (b) Schematic longitudinal cross section.

Fig. 2.8 (a) illustrates the equivalent circuit model for the case of zero thickness wall waveguide. The slot (presented by the parallel *LC* resonator) is coupled to the upper and lower waveguides via an impedance transformer. The turns ratio of the impedance transformer depend on the slot thickness, which is the thickness of the wall within which the slot is etched in our case, as well as the impedance definition of the two coupled domains [33].

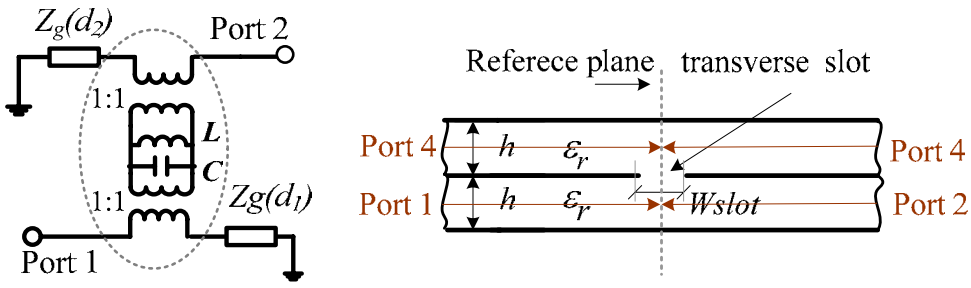

(a) (b)

Fig. 2.8 (a) Equivalent circuit model of transition of Fig. 2.7. (b) Longitudinal cross-section configuration of the parallel waveguide broadwall-slot coupler.

For the case of SIW implementation, the zero wall thickness model is a good approximation as the wall thickness is represented by that of the substrate copper coating. Since the structural parameters of both waveguides of the transition are the same and by neglecting the slot wall thickness, the impedance transformer turns ratio is unity.

Based on the wideband equivalent circuit model of the transverse slot given by the encircled part of Fig. 2.8 (a) that has been reported in [32], the slot inductance and capacitance can be accurately deduced. This is done by evaluating the reflection scattering parameter S_{11} at the input port of a two-layer, parallel waveguide coupler employing the same slot with the same waveguide structural parameters. The analytical expressions for L and C can thus be obtained from the analysis of the four-port network of the coupler (Fig. 2.8(b) and encircled part of Fig. 2.8 (a)), this is illustrated by Eq. (2.16) through Eq.(2.20).

$$S_{11} = \frac{1}{2(1+Y_{slot}Z_g)},\ Y_{slot} = j\omega C + \frac{1}{j\omega L} \tag{2.16}$$

where Y_{slot} and Z_g are the slot admittance and the waveguide wave impedance, and are given by Eqns. (2.17) and (2.18), respectively.

$$Y_{slot} = j\omega C + \frac{1}{j\omega L} \tag{2.17}$$

$$S_{11} = \frac{Z_e + Z_g(d_1) - Z_g}{Z_e + Z_g(d_1) + Z_g} \tag{2.18}$$

where F_c is the TE_{10} mode cutoff frequency, Z_o is a constant given by Eq. (2.19) for the power-voltage definition of the waveguide characteristic impedance [30].

$$Z_o = 2\sqrt{\frac{\mu}{\varepsilon}}\left(\frac{h}{a_{eq}}\right) \tag{2.19}$$

where a_{eq} is the SIW equivalent width, h is the waveguide height

From Eq. (2.16), it can be shown that

$$\omega C - \frac{1}{\omega L} = -\frac{1}{Z_g}\frac{\Im(S_{11})}{\Re(S_{11})} \tag{2.20}$$

Evaluating Eq. (2.20) at two different frequency points, *L* and *C* values can be obtained for different slot lengths, width, distances d_1 and d_2 for specific waveguide height, equivalent width and dielectric filling permittivity. The real and imaginary parts employed in Eq. (2.20) are obtained through HFSS simulation of the broad wall coupler problem using the same slot dimensions as well as the same waveguide structural parameters employed in the transition. It has to be noted that, in order to use HFSS simulation to evaluate the magnitude and phase of S_{11} of the coupler of Fig. 2.8 (b), the following two conditions must be satisfied. First, the reference plane in the simulation of all four ports of the coupler must be at the slot center level, as shown in Fig. 2.8 (b). Then, the waveguide impedance definition employed in (2.20) must be the same one employed in the simulation in defining the excitation ports.

For the equivalent circuit of Fig. 2.8 (a), the reflection and transmission scattering parameters are given by Eq. (2.21) and Eq. (2.22), respectively.

$$S_{11} = \frac{Z_e + Z_g(d_1) - Z_g}{Z_e + Z_g(d_1) + Z_g} \tag{2.21}$$

$$S_{21} = (1 + S_{11})\left\{ \frac{Z_g(d_2)(1 + Y_{slot} Z_g(d_1)) + Z_g(d_1)}{Z_e + Z_g(d_1)} - [1 + Z_g(d_2) Y_{slot}] \right\} \tag{2.22}$$

$$Z_e = \frac{[Z_g + Z_g(d_2)] Z_{slot}}{Z_g + Z_g(d_2) + Z_{slot}} \tag{2.23}$$

where $Z_g(d_1)$ and $Z_g(d_2)$ are the input impedances of short ended waveguide sections with waveguide impedance Z_g and lengths d_1 and d_2 respectively.

Fig. 2.9 shows the magnitude and phase transmission characteristics versus frequency for the transition of Fig. 2.8 (a) for different values of *h* available for the Rogers 6002 substrate. To avoid filtering effects and/or increased insertion losses that may be introduced by the shorted stubs at both sides of the transition slot, distances d_1 and d_2 have been kept constant and equal to the minimum distance allowed by the available technology, such that d_1=d_2=0.5 mm, while the slot dimensions are 0.5x9.11 mm^2.

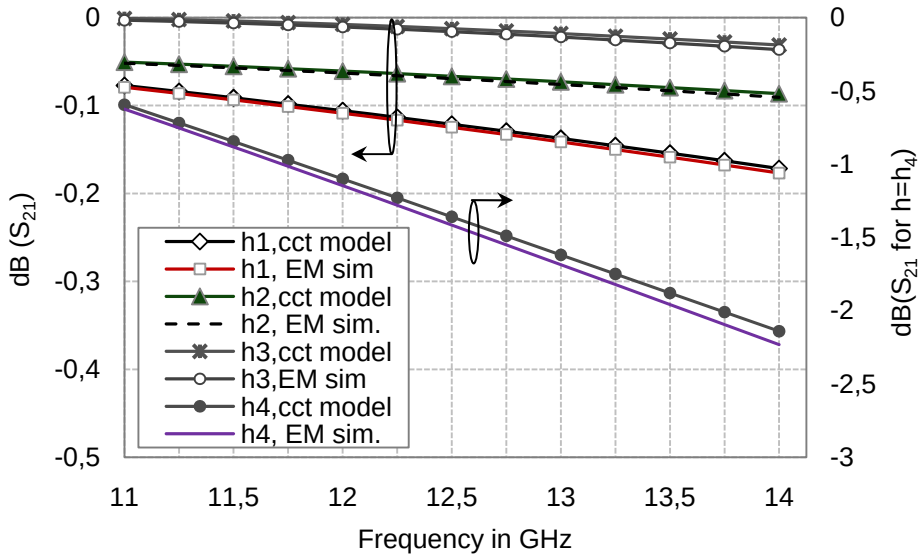

(a)

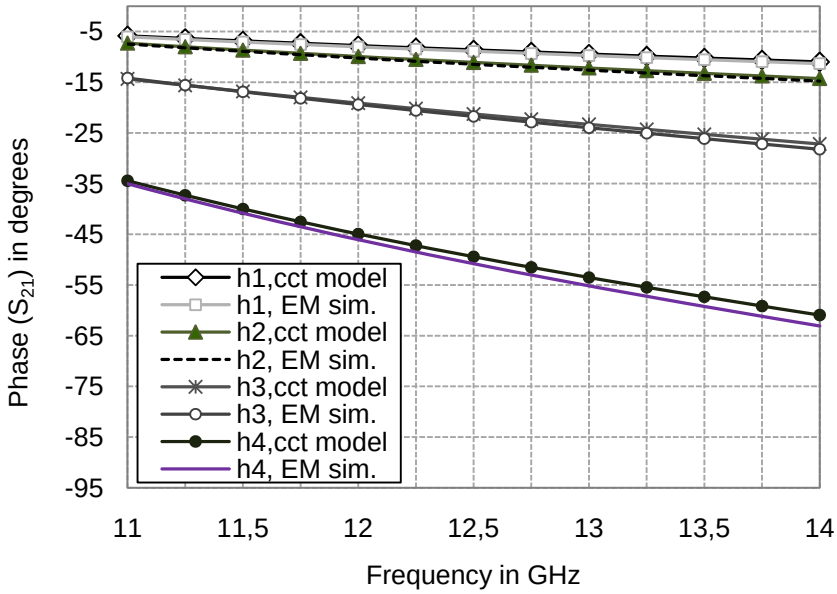

(b)

Fig. 2.9 Transmission coefficient versus frequency for the two-layer transition of Fig. 2.7 for different substrate heights, h_1=0.508mm, h_2=0.787mm, h_3=1.524mm, h_4=3.05mm. (a) Magnitude of S_{21}. (b) Phase of S_{21}.

The substrate parameters are those of the Rogers-Duroid 6002 with dielectric constant ε_r = 2.94, and loss tangent of 0.0017. The via hole diameter is 0.78 mm while the pitch size p = 1.3 mm and the SIW width a_{SIW} =10.4mm. The equivalent waveguide width a_{eq} used in Fig. 2.9 is therefore equal to 9.9 mm. The calculated values for L and C corresponding to the above mentioned slot dimensions with the

different values of h of Fig. 2.9 are summarized in Table 2.2. The calculated results of Fig. 2.9 are obtained upon determining the values of L and C using Eq. (2.16) through Eq. (2.20).

The calculated values based on the circuit model are in good agreement with those obtained from the full-wave HFSS simulations. The simulated phase results of Fig. 2.9 (b) are obtained by setting the reference planes of both ports at the center of the slot, thus accounting only for the phase introduced by the slot. By considering both magnitude and phase characteristics of Fig. 2.9, it can be seen that the thicknesses h_1 and h_2 are good candidates for the transition to be used in the foreseen Butler matrix owing to their low insertion loss together with the relatively small, low frequency-dependent associated transmission phase. Although the thickness h_3 has the minimum insertion loss, its main disadvantage for the foreseen matrix implementation would be its larger associated phase with larger slope of the phase curve. In fact, the lower the slope of the transmission phase-frequency curve with smaller absolute phase values is, the easier would be the integration of the corresponding transition in the phase delay arms of the matrix for wideband fixed phase shift.

Table 2.2 Transverse slot L and C values determined upon simulation of the parallel waveguide transverse slot broad wall coupler structure

	h_1= 0.508mm	h_2= 0.7787mm	h_3= 1.524mm	h_4= 3.05mm
L (nH)	8.50	3.49	2.14	1.29
C(fF)	12.73	64.93	131.14	224.72

2.3.2.2. Three-Layer, Variable-Width, Compensated-Length, Wideband Phase Shifter

This section addresses the design and analysis of a novel compact wideband phase shifter in three-layer SIW technology. The proposed structure exploits the previously developed low-loss two-level SIW transition in a multiply-folded three-layer compact SIW configuration.

Fig. 2.10 shows a cross-section longitudinal view of the developed phase shifter, together with an exploded view. The structure consists of a substrate integrated waveguide multiply folded along its length in a stacked three-layer topology. For each pair of waveguides, in two different stacked layers, the coupling is ensured via a narrow transverse slot in the common broad wall bounded by a common vertical shorting wall. From Fig. 2.10, the waveguide sections formed by the distances between the shorting walls and the corresponding coupling slots constitute short-circuited stubs. To avoid undesired filter effects or increased insertion losses, these distances d_1 and d_2 are chosen as small as the technology allows.

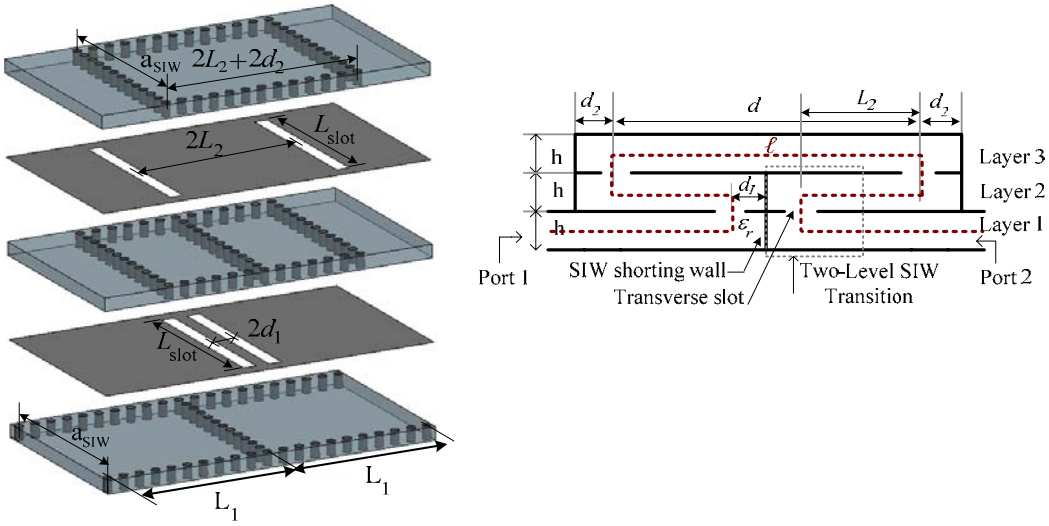

(a) (b)

Fig. 2.10 Three-layer SIW phase-shifter structure. (a) Exploded view. (b) Structure layout, longitudinal cross-section elevation view.

To achieve a specific phase difference $\Delta\phi$ between two similar structures, the propagation constant β is modified by varying the corresponding widths accordingly [23], such that:

$$\frac{\Delta\phi}{\ell} = \frac{\phi_1 - \phi_2}{\ell} = \beta_1 - \beta_2; \qquad \ell \cong 2(L_1 + 2L_2) \tag{2.24}$$

where ℓ is the effective propagation path length and ϕ_i is the transmission phase for the structure having the SIW width a_{SIWi}.

As previously discussed, the main drawback of the single-layer phase shifters based on the width variations of SIW sections is that it leads to relatively large sizes, as the larger the required ($\Delta\phi$) , the longer (ℓ) would be.

According to Fig. 2.10 and Eq. (2.24), it can be noticed that the proposed structure has the double advantage that its physical length $2L_1$ is different than its propagation path length achieving up to 66% area reduction (for L_1=L_2, with the limitation that L_2 must be sufficiently large to avoid coupling between the slots) compared to the latter phase shifters. On the other hand, the developed structure allows the introduction of slight length variations for different structures to compensate the relative slopes of the associated propagation factor curves, adding therefore one more design parameter to achieve well-controlled arbitrary wideband phase shifts while maintaining the same physical length. These slight variations are distributed over the two sections of length L_2 [34].

Fig. 2.11 shows the equivalent circuit model of the developed three-layer waveguide structure. Similarly to the previous section, the *LC* values are obtained by network analysis of the transverse slot broad-wall parallel waveguides coupler employing the same waveguide and slot parameters.

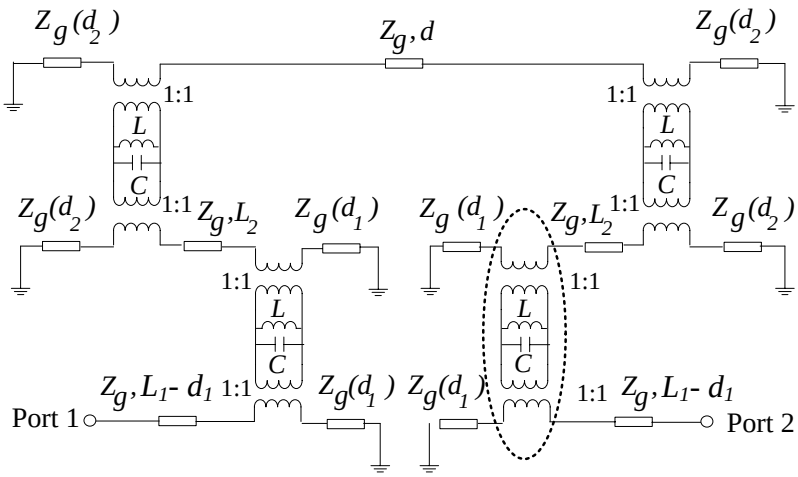

Fig.2.11 Equivalent-circuit model of the three-layer structure of Fig. 2.10, ($Z_g\ (d_i)$ is the input impedance of a shorted waveguide of length d_i with characteristic impedance Z_g).

By varying the SIW width of the structure of Fig. 2.10 together with the corresponding slot's length and the value of L_2, with respect to a reference similar structure, phase shifts up to 180° are achieved with wideband performance and low

insertion losses. The slots' width, d_1 and L_1 were kept constant in all designs and equal to 0.75 mm, 0.75 mm and 9 mm respectively, d_2=d_1. The structures have been designed on a 0.762 mm thick substrate with ε_r = 2.08 and tan δ =6×10^{-4}. The via-hole diameter d is 0.5 mm and the pitch is 0.95 mm.

Four different phase shifters are designed to ensure phase shifts of -45°, -90°, -135° and -180° with respect to a three-layer reference structure having the same physical length. Table 2.3 summarizes the optimized parameters of the different designed structures. Fig. 2.12 shows the simulated results for the reflection and transmission coefficients for structures 3 and 5 with the reference structure. The relative phase shifts between structures 2 to 5 of Table 2.3, with respect to the reference one are also shown. Electromagnetic simulations have been performed using HFSS simulator while Agilent ADS has been used to simulate the equivalent circuit of Fig. 2.11 upon determining the slot *LC* values as previously discussed.

From Fig. 2.12, a good agreement between the circuit simulations and the electromagnetic simulations is clearly verified. As expected, the insertion losses have slightly lower values for the circuit simulation compared to the full-wave simulations as the former ones do not account for losses through the lateral SIW walls. The wideband phase shift is clearly satisfied over the 11.5-13.5 GHz frequency band with maximum phase deviation less than 5° over the entire frequency band. These phase characteristics demonstrate a significant improvement over those previously mentioned in Section 2.3.1 with an area reduction of almost 50% with respct to the latter structure. The insertion losses do not exceed 0.4 dB with reflection losses below -12 dB over the entire band.

Table 2.3 Parameters and simulation results for four different phase shifters (three-layer SIW configuration) with the reference structure

Structure	$\Delta\phi$	a_{SIW} (mm)	L_2 (mm)	L (nH)	C (fF)	Maximum phase error over 11.5-13.5 GHz band
1	0°	10.10	5.7	19.17	9.04	Reference
2	-45°	10.28	5.94	23.18	8.91	+0.73°
3	-90°	10.46	5.94	23.06	6.96	-2.00°
4	-135°	10.64	6.00	25.63	7.19	-4.29°
5	-180°	10.90	6.17	24.76	7.76	-4.56°

For all structures, L_{slot}=a_{SIW}-d-0.25mm, d is the via-hole diameter.

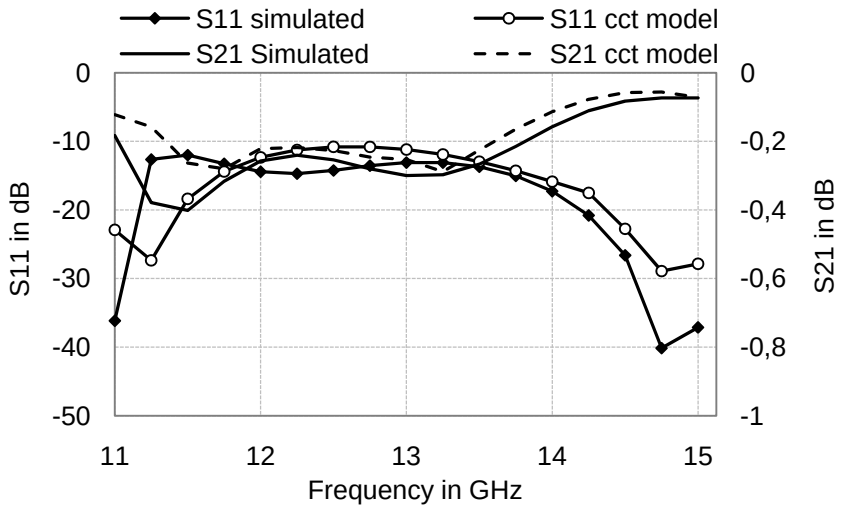
S11 simulated
S11 cct model
S21 Simulated
S21 cct model
0
-10
-20
-30
-40
-50
0
-0,2
-0,4
-0,6
-0,8
-1
S11 in dB
S21 in dB
11
12
13
14
15
Frequency in GHz

(a)

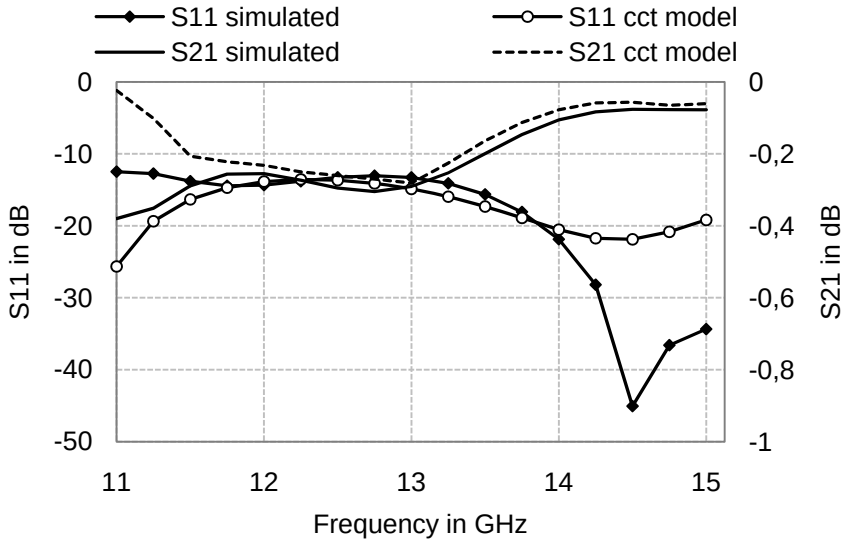
S11 simulated
S11 cct model
S21 simulated
S21 cct model
0
-10
-20
-30
-40
-50
0
-0,2
-0,4
-0,6
-0,8
-1
S11 in dB
S21 in dB
11
12
13
14
15
Frequency in GHz

(b)

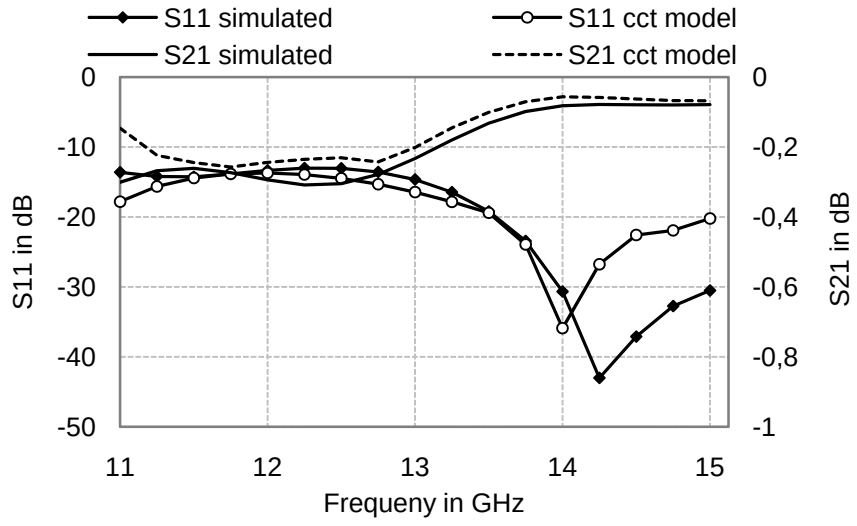
S11 simulated
S11 cct model
S21 simulated
S21 cct model
0
-10
-20
-30
-40
-50
0
-0,2
-0,4
-0,6
-0,8
-1
S11 in dB
S21 in dB
11
12
13
14
15
Frequeny in GHz

(c)

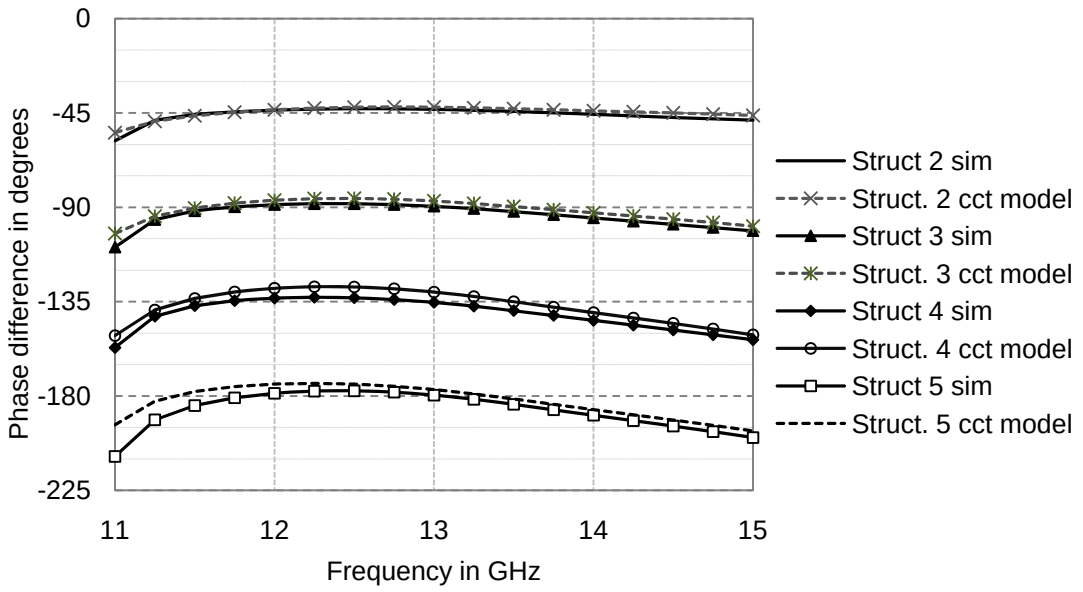

(d)

Fig.2.12 EM and equivalent circuit simulated (cct model) scattering parameters versus frequency for the structures of Table 2.3. (a) $|S_{11}|$ and $|S_{21}|$- reference structure. (b)$|S_{11}|$ and $|S_{21}|$- structure 3. (c) $|S_{11}|$ and $|S_{21}|$- structure 5. (d) Phase shifts with respect to the reference structure.

2.4. Conclusion

In this chapter, different techniques for the implementation of wideband fixed phase shifters in SIW technology have been presented. First, a novel CRLH structure has been proposed. The structure is based on a single-layer waveguide with shunt inductive windows (irises) and series transverse capacitive slots, suitable for SIW implementations for compact phase shifters. By varying both right-handed and left-handed parameters between different structures, wideband relative phase shifts can be obtained with a wide phase dynamic range. The main disadvantage of this structure is that it has relatively large insertion loss values especially in applications requiring many phase shifters as beam-forming matrices. These insertion loss values remain however within the typical range of non-lumped elements based CRLH implementations.

Second, the well-known equal length, unequal width SIW phase shifters have been discussed. These phase shifters are very suitable for SIW implementations as they fully exploit the flexibility of the SIW technology in different path shapes while offering wideband phase characteristics. To satisfy good return loss characteristics

with this type of phase shifters, the length has to be compromised with respect to the progressive width variations associated with the required phase shift values.

A two-layer, wideband low-loss SIW transition is then proposed. The transition is analyzed using its equivalent circuit model bringing a deeper understanding of its transmission characteristics for both amplitude and phase providing therefore the basic guidelines for electromagnetic optimization. Based on its equivalent circuit model, it can be shown that bandwidths up to 30% with insertions loss values lower than 0.2 dB can be achieved by properly calculating the transition parameters. This transition is then exploited to develop a three-layer low-loss SIW structure. The developed structure is indeed a waveguide, multiply-folded along its length in a low-loss three-layer topology. The structure is therefore a very attractive candidate for the implementation of variable width phase shifters with the double advantage of offering large dynamic range wideband phase shift characteristics with embedded compensated-length compact structure. The main disadvantage of such a structure is its relatively complex technological aspects. However, one can find several works in three-layer SIW structures showing the mature SIW technology for such implementations.

A good compromise would be to use the developed two-layer transition in the implementation of unequal-width, compensated-length wide-band phase shifters for the implementation of beam-forming matrices in two-layer topologies. Such phase shifters would be of particular interest for the implementation of two-layer SIW Butler matrices to avoid the path crossing problems while implementing the wideband phase shifts. This will be shown in the following chapter.

References of Chapter Two

[1] B. M. Schiffman, "A new class of broad-band microwave 90-degree phase shifters," *IRE Trans. Microw. Theory Tech.*, Vol. 6, pp. 232-237, April 1958.

[2] B. Schiek and J. Kohler, "A method for broad-band matching of microstrip differential phase shifters," *IEEE Trans. Microw. Theory Tech.*, Vol. 41, pp. 9-14, Jan. 1993.

[3] J. Dittlof, F. Arndt, D. Grauerholtz, "Optimum design of waveguide E-plane stub loaded phase shifters," *IEEE Trans. Microw. Theory Tech.*, Vol. 36, pp. 582-587, March 1988.

[4] X. Xu, R. G. Bosisio and K. Wu, "A new six-port junction based on substrate integrated waveguide technology," *IEEE Trans. Microw. Theory Tech.*, Vol. 53, pp. 2267-2273, July 2005.

[5] K. Sellal, L. Talbi, T. A. Denidni and J. Lebel, "Design and implementation of a substrate integrated waveguide phase shifter," *IET Microw. Antennas Propagat.*, Vol. 2, No. 2, pp.194-199, March 2008.

[6] Y. Cheng, W. Hong and K.Wu, "Novel Substrate Integrated Waveguide Phase Shifter for 180-degree Directional Coupler," *IEEE MTT-S Int. Microw. Symp.*, June 2007.

[7] E. Sbarra, L. Marcaccioli, R. V. Gatti and R. Sorrentino, "A novel Rotman lens in SIW technology," *IEEE Europ. Microw. Conf.*, Munich, pp. 1515-1518, Oct. 2007.

[8] K. Morimoto, J. Hirokawa and M. Ando, "Design of a 180 single-layer divider to control side-lobe and crossover levels in Butler matrix beam-switching antenna," *IEEE Asia Pac. Microw. Conf.*, Thailand, pp.1-4, Dec. 2007.

[9] V. G. Veselago, "The electromagnetic of substances with simultaneously negative values of ε and μ," *Soviet. Phys. Uspekhi*, vol. 10, no.4, pp. 509-514, Jan.-Feb. 1968.

[10] D. R. Smith, W. J. Padilla, D.C. Vier, S. C. Nemat-Nasser, and S. Schlutz, "Composite medium with simultaneously negative permeability and permittivity," *Phys. Rev. Lett.*, vol. 84, no. 18, pp. 4184-4187, May 2000.

[11] R. A. Shelby, D. R. Smith and S. Schlutz, "Experimental verification of a negative index refraction," *Science*, vol. 292, pp. 77-79, Apr. 2001.

[12] J. B. Pendry, A. J. Holden, W.J. Stewart, and I. Youngs, "Extremely low frequency plasmons in metallic mesostructures," *IEEE Phys. Rev. Lett*. vol. 76, no. 25, pp. 4773-4776, June, 1996.

[13] D. R. Smith, D.C. Vier, W. Padilla, S. C. Nemat-Nasser, and S. Schlutz, "Loop-wire medium for investigating plasmons and at microwave frequencies," *App. Phy. Lett*. vol. 75., no. 10, pp. 1425-1427, Sept. 1999.

[14] A. A. Oliner, “A periodic-structure negative-refractive index medium with resonant elements,” *USNC/URSI National Radio Science Meeting*, San Antonio, TX, p. 41, June 2002.

[15] A. K. Iyer, G. V. Eleftheriades, “Negative refractive index metamaterials supporting 2-D waves,” *IEEE MTT-S Int. Symp*., vol. 2, San Antonio, TX, pp. 1067-1070, June 2002.

[16] C. Caloz, H. Okabe, T. Iwai, and T. Itoh, “Transmission line approach of left-handed (LH) materials,” *USNC/URSI National Radio Science Meeting*, San Antonio, TX, p. 39, June 2002.

[17] C. Caloz and T. Itoh, “Application of the transmission line theory of left-handed (LH) materials to the realization of microstrip LH transmission line,” *IEEE AP-S Int. Symp*., San Antonio, TX, pp. 412-415, June 2002.

[18] I. Hsiang, M.D. Vincentis, C. Caloz and T. Itoh, “Arbitrary dual-band components using composite right/left-handed transmission lines,” *IEEE Trans. Microw. Theory Tech.*, vol. 52, no. 4, pp.1142-1149, April 2004.

[19] H. Okabe, C. Caloz and T. Itoh, “A compact enhanced-bandwidth hybrid ring using an artificial lumped-element left-handed transmission-line section,” *IEEE Trans. Microw. Theory Tech.*, vol. 52, no. 3, pp.798-804, March. 2004.

[20] C. Caloz and T. Itoh, “Transmission line approach of left-handed (LH) materials and microstrip implementation of an artificial LH transmission line,” *IEEE Trans. Microw. Theory Tech.*, vol. 52, no. 5, pp.1159-1166, May. 2004.

[21] C. Caloz, A. Sanada and T. Itoh, “A novel composite right-/left-handed coupled-line directional coupler with arbitrary coupling level and broadbandwidth,” *IEEE Trans. Microw. Theory Tech.*, vol. 52, no. 3, pp.980-992, March. 2004.

[22] Y. Horii, C. Caloz and T. Itoh, “Super-compact multilayered left-handed transmission line and diplexer application,” *IEEE Trans. Microw. Theory Tech.*, vol. 53, no. 4, pp.1527-1533, April 2005.

[23] A. Ali, H. Aubert, N. Fonseca and F. Coccetti, “Novel compact waveguide-based composite right/left-handed phase shifter with arbitrary phase shift and broad bandwidth: analysis and design,” *IEEE AP-S Int. Symp.*, San Diego, June 2009.

[24] M. A. Anioniades and G. V. Eleftheriades, “Compact linear lead/lag metamaterial phase shifters for broadband applications,” *IEEE Antennas Wireless Propag. Lett.*, vol.2, no. 7, pp. 103-106, Jul. 2003.

[25] J. Perruisseau and A. Skrivervik, “Composite Right/ Left-Handed transmission line metamaterial phase shifters in MMIC technology,” *IEEE Trans. Microw. Theory and Tech.*, vol. 54, No. 4, April, 2004.

[26] O. G. Vendik, I. B. Vendik, D.V. Kholodnyak, S. P. Zubbko and E. V. Serebryakova, “Electronically controlled phase shifters based on right/left-handed transmission lines,” *Europ. Microw. Conf.*, Paris, Oct. 2005.

[27] K. Okubo, M. Kishihara, A. Yamamoto, J. Yamakita and I. Ohta, “New composite right/left-handed transmission line using substrate integrated waveguide and metal-patches,” *IEEE MTT-S Int. Symp*., Boston, pp. 41-44, June 2009.

[28] Y. D. Dong and T. Itoh, “Composite right/left-handed substrate integrated waveguide and half-mode substrate integrated waveguide,” *IEEE MTT-S Int. Symp*., Boston, pp. 49-52, June 2009.

[29] C. Caloz and T. Itoh, “Electromagnetic metamaterials: transmission line theory and microwave applications,” John Wiley & Sons, 2006.

[30] N. Marcuvitz, “Waveguide handbook”, Peter Peregrinus, London, 1986.

[31] D. Deslandes and K. Wu, “Design consideration and performance analysis of substrate integrated waveguide components,” *Europ. Microw. Conf.*, Milan, Oct. 2002.

[32] I. A. Eshrah, A. A. Kishk, A. B. Yakovlev, A. W. Glisson and C. E. Smith, “Analysis of Waveguide Slot-based structures using-wideband equivalent circuit model,” *IEEE Trans. Microw. Theory Tech*., Vol. 52, No. 12, pp.2691-2696, Dec. 2004.

[33] I. A. Eshrah, A. A. Kishk, A. B. Yakovlev, A. W. Glisson, “Generalized equivalent circuit model for transverse waveguide slots and applications,” *Progress in Electromagn. Research*, Vol.69, pp.1-20, 2007.

[34] A. Ali, H. Aubert, N. Fonseca and F. Coccetti, “Novel compact three-layer wideband phase shifter in SIW technology,” *Progress in Electromagn. Research. Symp.*, pp. 500-501, Aug. 2009.

CHAPTER THREE

Multi-Layer Wideband SIW Couplers

3.1. Introduction

This chapter addresses the design of novel structures of wideband waveguide-based couplers in SIW technology. As a matter of fact, couplers are a key component of nowadays communication systems where low cost, small area, system integration and wideband characteristics are of great interest.

This chapter addresses the design of two novel, waveguide-based couplers exploiting the SIW characteristics in multilayer substrate topologies. The first structure is for a 90° SIW coupler based on the coupling between two-parallel waveguides through a pair of offset, inclined resonant slots. The structure has the advantage of providing a large dynamic coupling range with wideband performances for both phase and magnitudes characteristics with low insertion losses. Such characteristics make the developed coupler a good candidate for the design of SIW subsystems as beam-forming matrices in compact two-layer topologies.

For dual-band operation, a novel structure for a concentric hybrid ring coupler is developed. The structure employs a Ridged Substrate Integrated Waveguide (RSIW) providing a wideband performance with a compact design. The structure is endowed with an integrated demultiplexer scheme based on a periodic defect in the outer ring coupler. Owing to the coupler structure, an arbitrary band separation can be achieved within the fundamental mode operation bandwidth of the employed ridged waveguide. A low loss C/K dual band operation is demonstrated with relatively large bandwidths over both frequency bands.

The chapter is organized as follows; Section 3.2 shows the two-layer parallel-waveguide 90° coupler, where Section 3.2.1 gives a complete description of the coupler structure and design considerations. In Section 3.2.1.1 the effects of the slot parameters on the coupling and the transmission phase are illustrated followed by the transmission phase compensation in Section 3.2.1.2. Section 3.3 describes the stub-loaded ridge waveguide based dual band ring coupler. First, Section 3.3.1 gives the structure description, and then, Section 3.3.2 gives the design procedures and considerations, where results and responses are shown in Section 3.3.3 and finally the conclusion is outlined in Section 3.3.4.

3.2. Novel Two-Layer Parallel-Waveguide 90° Coupler

This section presents a novel two-layer broadband coupler in SIW technology. The proposed coupler is realized by two parallel waveguides having a pair of parallel inclined-offset resonant slots in their common broad wall. A detailed parametric study of the coupler is carried out including the effect of the slot length, inclination angle and offset on both the coupling level and the transmission phase.

The proposed coupler has the advantage of providing a wide coupling dynamic range with wideband performance by varying the slot parameters allowing the design of wideband SIW Butler matrix in two-layer topology [1]. In addition, previously published SIW couplers (see, e.g. [2]) suffer from direct correlation between the transmission phase and the coupling level, while the coupler hereby proposed allows controlling the transmission phase without significantly affecting the coupling level. Owing to these features, the proposed coupler is a good candidate for the design of beam-forming matrices in two-layer topologies.

On the other hand, by comparing the hereby presented coupler to that of the narrow wall waveguide coupler, although the latter one has a simpler design, it suffers from larger area (almost the double). Two-layer designs of the narrow-wall SIW coupler have been recently developed to reduce its area [3] by using the folded waveguide reported in [4]. Such designs meet similar technological challenges as the proposed coupler while the transmission phase compensation will be more delicate.

3.2.1. Coupler Structure and Design Considerations

The structure of the proposed coupler is illustrated in Fig. 3.1. The coupler consists of two parallel rectangular waveguides sharing a common broad wall in which a pair of compound (offset and inclined) coupling slots is etched.

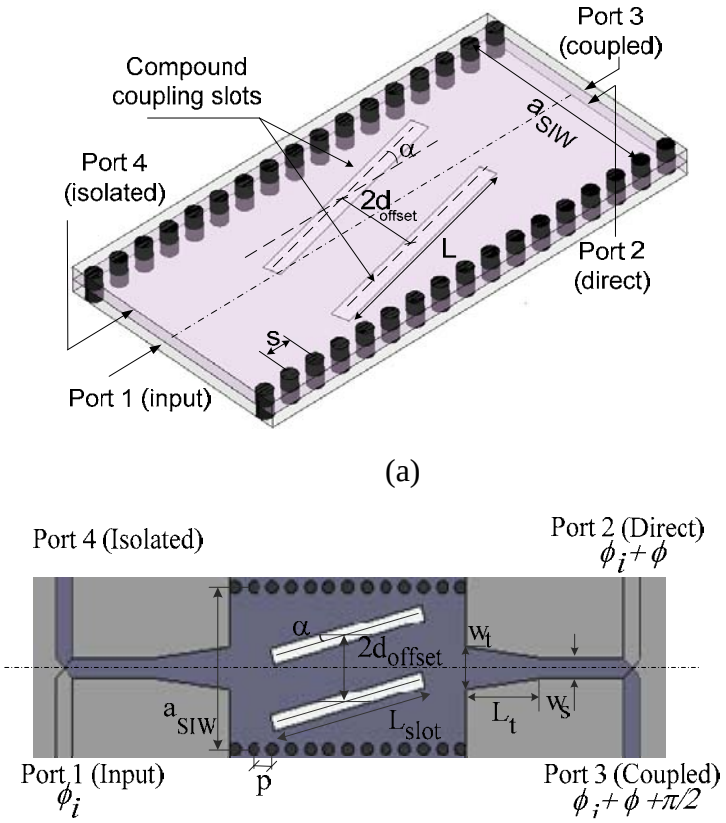

Fig. 3.1. Layout of the developed two-layer SIW coupler.
(a) 3-D view. (b) top view showing microstrip access transitions.

The design of the coupler is straightforward: the coupler width is calculated based on the well established waveguide theory for the TE_{10} mode propagation over the entire frequency band. The equivalent SIW width is then calculated based on the formulas given in [5]. The cutoff frequency F_{c10} of the TE_{10}-mode is chosen lower than the smallest operating frequency in order to obtain a relatively stable coupling level in the band of interest and to offer a larger width for the coupler waveguide. A relatively wider waveguide width provides higher design flexibility in the slots offset, length and inclination angle and therefore a wider coupling dynamic range as shown later.

The best matching conditions are reached when the slot length (L_{slot}) corresponds to the resonant length calculated at the design center frequency as a function of the tilt angle (α) and offset (d_{offset}) with respect to the longitudinal axis of the waveguide together with the waveguide height [6]. The electrical equivalent circuit of the proposed coupler is not simple to find, as it employs compound coupling slots and therefore the forward and backward scattered fields are neither in phase nor out of phase. A detailed parametric study is then very useful to study the effect of the slot parameters on both the coupling level and the transmission phase.

3.2.1.1 Effect of the Slot Parameters on the Coupling and the Transmission Phase

In this section, a parametric study is presented by varying the slot offset and inclination angle while optimizing the slot length to obtain good matching conditions with reflection losses below -20 dB over the 11.5-13.5 GHz frequency band. (L_{slot} is expressed in terms of the waveguide wavelength at 12.5 GHz).

Fig. 3.2 shows the variation of the coupling level and the associated transmission phase (Arg (S_{21})) versus d_{offset} for different values of α and L_{slot}, while the slots width is kept constant at 0.5 mm. Increasing the slot width results in a slight increase in the coupling but on the expense of an increased return loss as well. These results are obtained using the FEM-based Ansoft HFSS for a coupler structure designed on a 0.762 mm thick Neltec NY9208 substrate with ε_r=2.08 and tan δ =6.10^{-4}.The via hole diameter is 0.5 mm and the pitch is s=0.95 mm. The coupler SIW width is a_{SIW} =11.85 mm. With the selected SIW parameters, the first higher order mode is the TE_{20} mode with a cutoff frequency F_{c20}=18 GHz.

It can be seen that a wide coupling dynamic range can be obtained by varying the slot parameters with a large variation in the transmission phase. As expected, the same coupling level, as well as the transmission phase, can be obtained by different sets of α, d_{offset} and L_{slot}. Moreover, it should be noted that among all of the slot parameters, the offset distance has a critical effect. This is due to its direct impact on the field within the slots as it causes a rapid variation with α for small offsets and slow variations for larger ones. This explains the higher gradient of the coupling, as well as the phase delay, with respect to α, and L for smaller offsets than for larger ones.

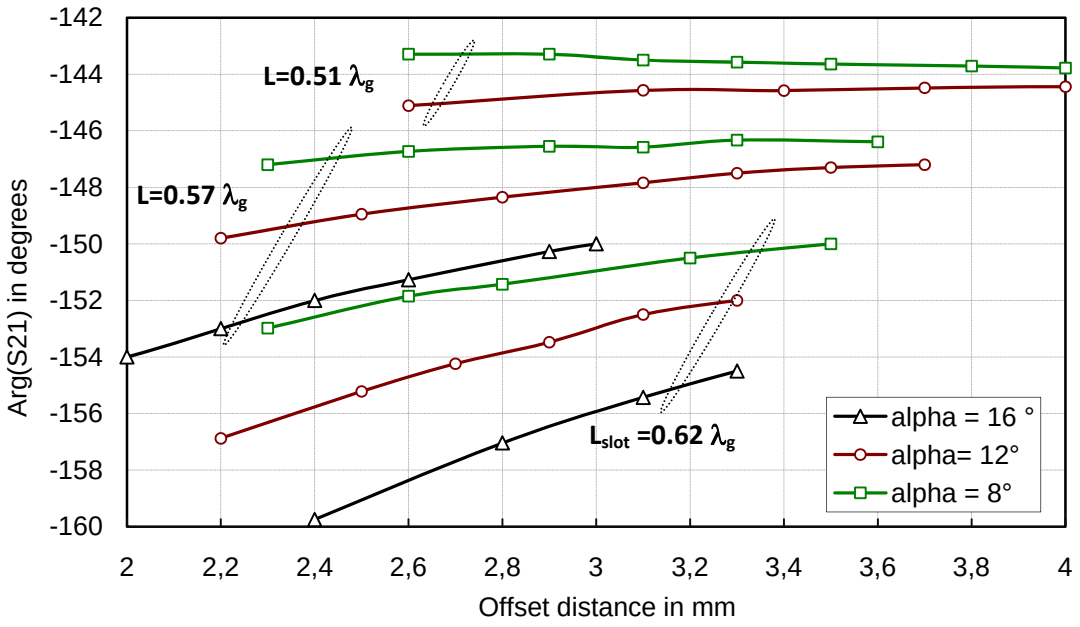

(a)

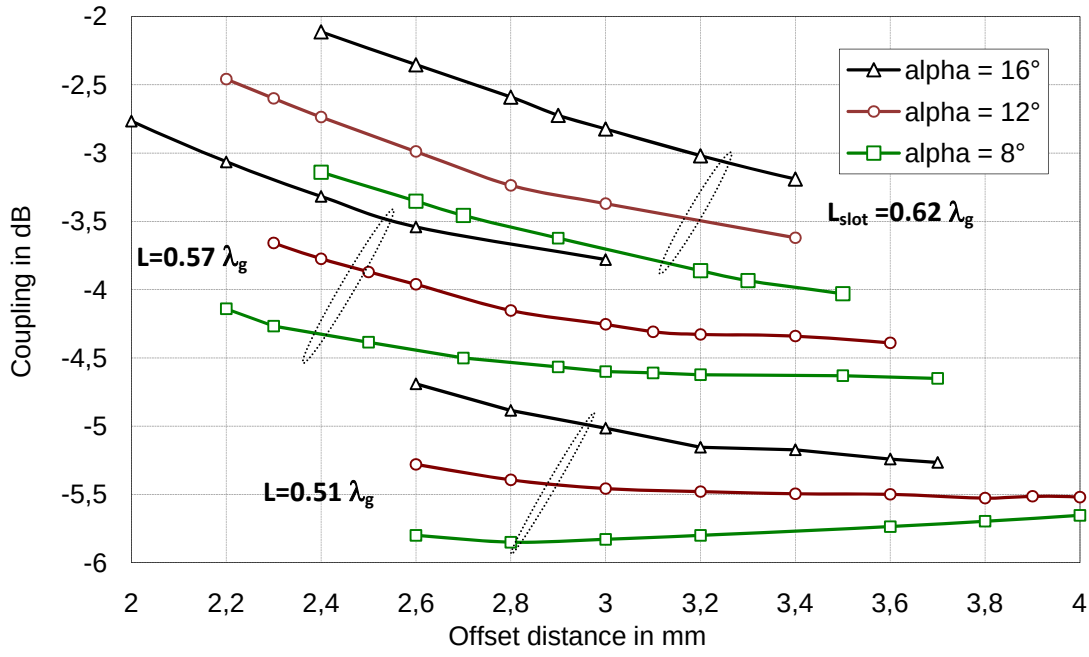

(b)

Fig.3.2 Simulation results at 12.5 GHz for the two-layer SIW coupler versus slot offset for different values of α and L_{slot}: (a) Transmission phase for a total coupler length of 29.95 mm (32 vias). (b) Coupling level variation.

3.2.1.2 Transmission Phase Compensation

In this section, phase compensation means the achievement of different coupling levels while maintaining the same transmission phase delay. It has been shown so far that the phase delay naturally varies according to the slot parameters. This is not convenient in applications where both amplitude and phase characteristics

are major design constraints such as beam-forming matrices employing different couplers such as the Nolen matrix [7].

Three different couplers have been designed and optimized. The same material and SIW parameters of the previous section have been used in the design. The structural parameters and simulation results over the 12-13 GHz frequency band are summarized in Table 3.1.

Table 3.1 Optimized parameters and results for different SIW couplers.
The phase-compensated parameters are given inside the brackets […].

Coupling (dB)	**3.02**	**4.77**	**6.02**
a_{SIW} **(mm)**	11.85 [11.5]	11.85 [11.72]	11.85 [11.85]
L **(mm)**	13.05 [12.95]	11.2 (11.15)	10.6
α **(°)**	15 [4]	16 (6)	9
d **(mm)**	2.65 [2.7]	3 (3.2)	3.2
$\|S_{31}\|$ peak to peak error (dB)	0.04/0 [0.14/0.05]	0.12/-0.07 [0.16/-0.12]	0.29/ -0.26
Arg(S21) at 12.5 GHz (°)	-159.35 [-144.27]	-149.29 [-144.14]	-144.2
arg(S_{21}) peak to peak error (°)	[1.43/-1.65]	[0.88/-0.83]	Reference

Fig. 3.3 shows the transmission phase versus frequency for the three couplers. It can be seen that although the slot parameters affect the transmission phase values, the phase slopes remain almost the same in a relative wide band. This wideband performance can be explored together with the previously discussed coupling level and transmission phase in the phase compensation process. This can be accomplished by varying the couplers width-therefore introduce one more parameter to change the propagation constant and re-optimizing the slots parameters to reach the required coupling with the same phase delay. This is shown in Table 3.1 taking the 6.02 dB coupler as the phase reference case.

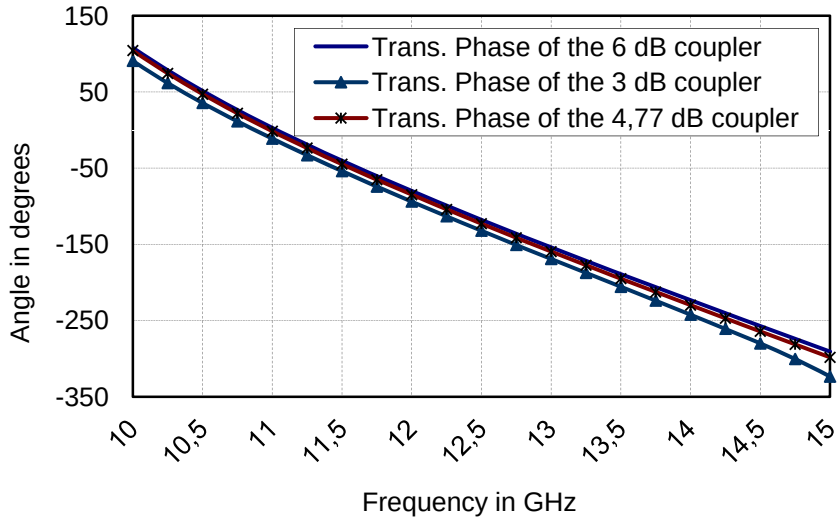

Fig.3.3 Transmission phase versus frequency for the 3.02 dB, 4.77 dB and 6.02 dB couplers without phase compensation.

3.2.2. Experimental Results and Discussion

In this section, a 6 dB coupler is optimized with the same aforementioned SIW parameters. The slot parameters are d_{offset}=3.5 mm, L_{slot}=11 mm and α=12°. In order to measure the designed coupler, wideband SIW to microstrip transitions [8] together with 90° SIW bends are used, which is expected to increase the insertion loss of the circuit.

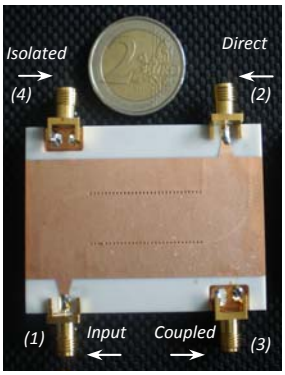

Fig.3.4 Photograph of the fabricated two-layer SIW coupler.

Fig.3.5 shows the simulated and measured magnitudes of the S-parameters. while the simulated and measured phase difference between the direct and coupled ports is illustrated in Fig.3.6. Simulated results account for conductor and dielectric losses. The simulated results show a peak-to-peak error for the coupling coefficient of +0.09/-0.29 dB over the frequency band (12-13 GHz) and +0.23/-0.47 dB over (11.5-13.5 GHz) band, while both isolation and reflection coefficients are below -20

dB. The simulated phase difference remains almost constant at -90° over the (11.5-13.5 GHz) frequency band.

Measured results are in good agreement with the simulated ones. The measured reflection coefficient is lower than -15 dB over the frequency band (11.5-13.5 GHz) and below -20 dB over the band (12-13 GHz) while the isolation is below -18 dB. On the other hand, the measured and simulated phase differences shown in Fig. 3.6 are also in good agreement with a maximum deviation of 6°. The peaks observed in the measured phase are due to the presence of un-metalized via holes whose effect is not observed in the amplitudes measurements. The waving effect observed in the measured results especially the phase is due to the non-linear phase characteristics of the microstrip-SIW transition.

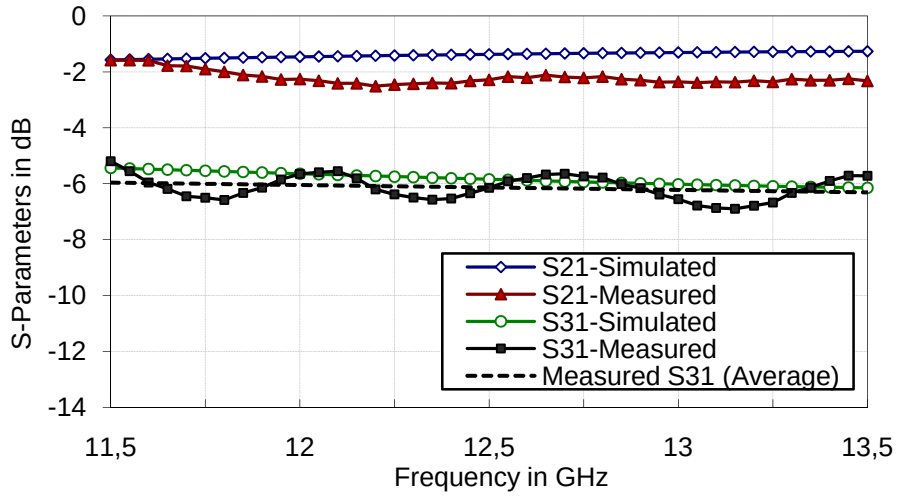

(a)

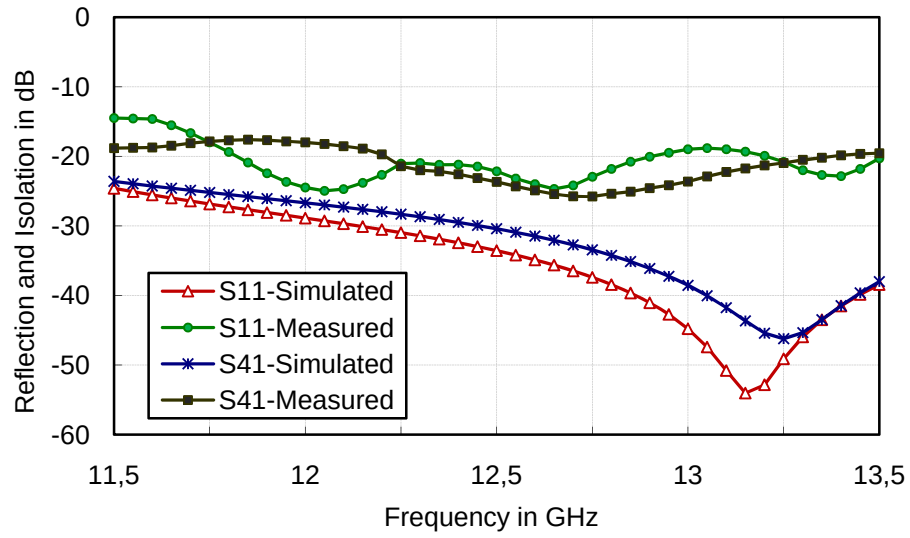

(b)

Fig. 3.5 Simulated and measured results of the 6dB SIW coupler. (a) Direct and coupling amplitudes. (b) Reflection and isolation amplitudes.

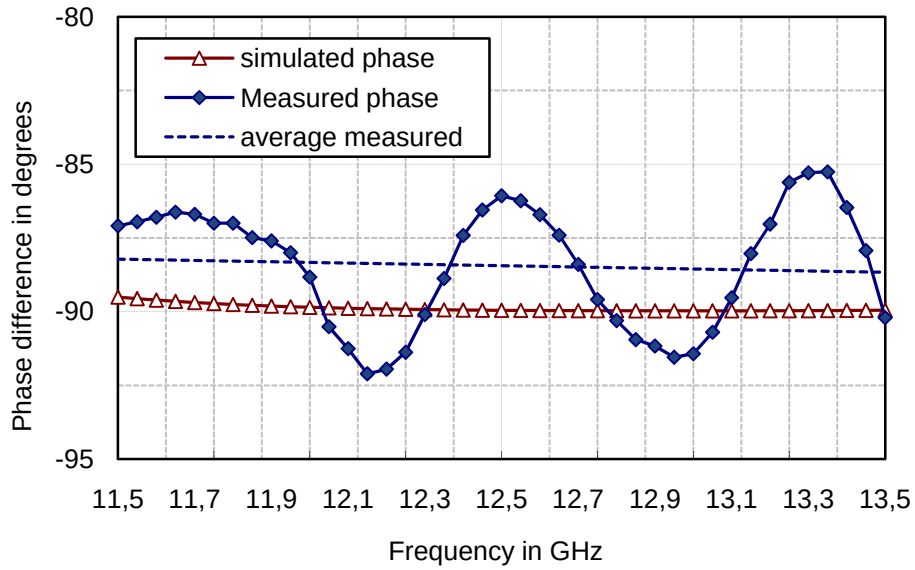

Fig. 3.6 Simulated and measured phase difference between ports 2 and 3.

3.2.3 Conclusion

A wideband SIW directional coupler is developed in a two-layer SIW topology. A detailed parametric study is presented proving a wide coupling dynamic range. The wideband performance of the coupler in terms of coupling magnitudes and phase difference between the direct and coupled ports besides its low insertion loss represents very promising characteristics for the implementation of beam-forming matrices in two-layer topologies. The proposed structure allows phase compensation for different coupling levels. A 6 dB coupler is verified experimentally, showing a 16% coupling bandwidth at 12.5 GHz with good isolation and reflection performances.

3.3. Stub-Loaded Ridge-Waveguide Based Dual-Band Ring Coupler

This section presents a novel dual-band concentric 180° ring coupler. The coupler is designed to cover two independent frequency bands. The lower frequency band lies in the C-band with a bandwidth more than 8.5% centered at 7.2 GHz while the upper band lies in the K-band with a coupling bandwidth of 14.6% centered at 20.5 GHz. The presented coupler ensures low dispersive 3-dB coupling with almost the same characteristics over both frequency bands while the upper frequency band is

about three times the lower one. The structure is based on Ridge SIW (RSIW) which ensures the wide band operation. The structure is also endowed with a low insertion loss demultiplexing scheme and a wideband microstrip to RSIW transition.

3.3.1. Structure Description

Fig. 3.7 shows the proposed coupler structure. The structure consists of two concentric hybrid ring couplers with the outer coupler responsible of the low frequency band while the coupling at the higher frequency band is ensured by the smaller inner one. The same access waveguides are used for both bands. These waveguides are the outermost waveguide sections in Fig. 3.7. A fundamental mode operation must be therefore ensured by these waveguides over the entire frequency band between the lowest operation frequency of the lower frequency band and the highest frequency in the upper band which makes a relatively large bandwidth for classical rectangular waveguides even for those with reduced heights implemented in SIW technology.

Therefore the use of ridge-waveguide appears as a very good candidate for such a structure to resolve the bandwidth problem. For single and double ridged waveguides, having the same ratios for the ridge depth and width with respect to the waveguide height and width, respectively, there is no great difference in the achievable maximum bandwidth [9], [10]. Therefore, for simpler design and realization, a single ridged waveguide will be used in the design of the foreseen coupler. On the other hand, as the feeding waveguides allow the propagation of both frequency bands and since the outer ring must be designed such that its waveguide impedance is $\sqrt{2}$ times that of its feeding waveguide sections, exciting the coupler at the upper frequency band would lead to undesired propagation in the outer coupler instead of the inner one. In order to maintain the coupler operational in two independent arbitrary frequency bands (lying within the bandwidth of the ridge waveguide), a demultiplexing scheme is needed to forbid the propagation of the upper frequency band within the outer coupler. In other words, the outer coupler should act as a bandpass filter with the lower frequency band within the pass-band and the outer frequency band cutoff by the stopband. This filter effect is hereby achieved by periodically stub-loading the outer coupler through periodic radial transverse slots in its un-ridged waveguide wall.

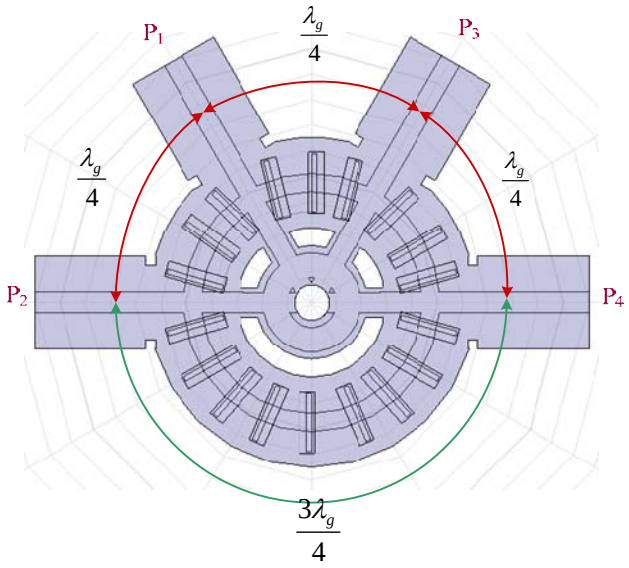

Fig. 3.7 Layout of the developed dual-band concentric ridged-waveguide ring coupler.

3.3.2. Design Procedure and Consideration

The design of the proposed ring coupler follows a twofold approach. First, the impedance and bandwidth curves are calculated for different ratios of ridge width and depth with respect to the waveguide width and height. These curves are calculated based on the Transverse Resonance Method (TRM) design equations of the ridged-waveguide for acceptable variations of the ridge's parameters. Upon calculating these curves, the parameters of the outer-most ridged-waveguide are determined by satisfying the required bandwidth and space constraints. The parameters of the ridge waveguide constituting the ring are calculated by using the previously calculated design curves subject to the known impedance ratio of the ring coupler, such that the impedance of the ring is $\sqrt{2}$ times that of its feeding waveguide section. This is accomplished for both rings. Second, the outer ring is periodically loaded by short-circuited stubs via radial transverse slots centered above the ridge. These stubs and their spacing are optimized such that to produce an upper stopband in the transmission response of the outer ridge waveguide. This stopband has to provide a sufficiently high rejection for the upper frequency band, therefore forbidding it from propagating through the outer ring. The parameters calculated upon this procedure together with other structural parameters at the different junctions are then subject to optimization using Ansoft HFSS.

3.3.2.1. TRM for Ridged Waveguides

The characteristic impedance, cutoff wavelength and fundamental mode bandwidth are in fact the major parameters of a ridged waveguide. These parameters have been the subject of several full-wave based works [11]-[13]. However, the TRM has the advantage of providing approximate analytical expressions for the characteristic impedance and bandwidth. These expressions are very useful to have a good understanding of their performance corresponding to the ridge waveguide parameters [9], [10], [14] and [15]. This section addresses the analytical expressions based on the TRM for a single-ridged waveguide which will be used to calculate the design curves used through the design of the foreseen coupler.

Fig. 3.8 shows a cross-section view of single and double-ridged waveguide. Both waveguide types have the equivalent circuit model shown in Fig. 3.9. The circuit model of Fig. 3.9 is that of a parallel-plate transmission line representing the ridge of width *W* and height *S* connected at both sides to short-ended sections of similar transmission lines with width $(a-W)/2$ and height *b*.

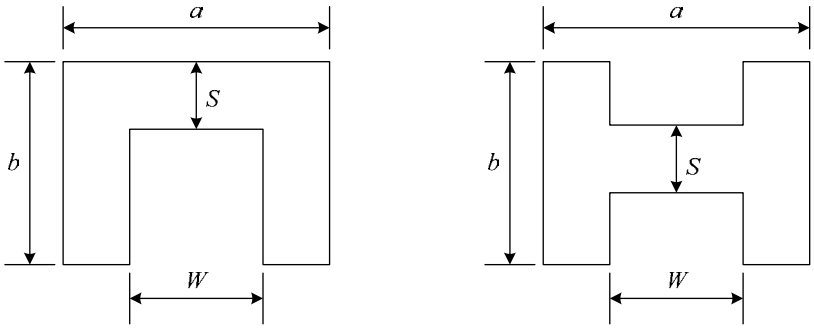

(a) (b)

Fig. 3.8 Cross-section of ridged-waveguide and equivalent circuit model. (a) Single-ridge waveguide. (b) Double-ridge waveguide.

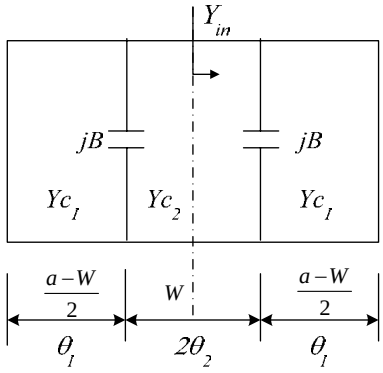

(c)

Fig. 3.9 Equivalent circuit model of a ridged waveguide, annotations refer to Fig. 3.8.

The shunt capacitive susceptance *jB* accounts for the energy stored in the fringing fields at the step junction between the two different heights [9], [10] and [16]. According to the equivalent circuit of Fig. 3.9, the input admittance seen at the center of the middle section Y_{in} is given by:

$$Y_{in} = Y_{c2}\frac{Y + jY_{c2}\tan(\theta_2)}{Y_{c2} + jY\tan(\theta_2)} \tag{3.1}$$

Where Y_{c1} and Y_{c2} are the characteristic admittances of the parallel-plate transmission line sections with heights *b* and *S*, respectively. *Y* is the parallel equivalent admittance and is given by Eq. (3.2) while θ_1 and θ_2 are the electrical lengths with respect to the cutoff wavelength and are given by Eqns. (3.3) and (3.4), respectively.

$$Y_{in} = jB - jY_{c1}\cot(\theta_1) \tag{3.2}$$

$$\theta_1 = k_c\frac{a-W}{2}, \quad k_c = \frac{2\pi}{\lambda_c} \tag{3.3}$$

$$\theta_2 = k_c\frac{W}{2} \tag{3.4}$$

From Eq. (3.1), the ratio Y_{c2}/Y_{c1} can be substituted by the inverse ratio of the corresponding heights *b/S* since the admittance of a parallel-plate TL is inversely proportional to its height. The cutoff conditions for the TE_{10} and TE_{20} modes propagations are directly obtained according their corresponding field patterns. The TE_{10} mode corresponds to a maximum electric field with zero current at the center of the middle section of the ridged waveguide of Fig. 3.9 which corresponds to setting Eq. (3.1) to zero (numerator = 0). For even TE_{n0} modes, the electric field vanishes at the latter position which can be described by setting Eqn. (3.1) to infinity (denominator = 0). The cutoff conditions for the TE_{10} and TE_{20} modes can be therefore given by [9]:

$$\cot(\theta_1) - \frac{b}{s}\tan(\theta_2) - \frac{B}{Y_{c1}} = 0 \tag{3.5}$$

$$\cot(\theta_1)+\frac{b}{s}\tan(\theta_2)-\frac{B}{Y_{c1}}=0 \tag{3.6}$$

Eq. (3.5) applies to the odd TE_{n0} modes while Eq. (3.6) applies for the even TE_{n0}. An approximate expression for the normalized shunt susceptance has been reported in [16] based on the calculated curves presented in [17], and is given by Eq. (3.7).

$$\frac{B}{Y_1}=\frac{2b}{\lambda_c}\left[1-\ln(4u)+\frac{1}{3}u^2+\frac{1}{2}(1-u^2)^4\frac{b^2}{\lambda_c^2}\right],\ u=\frac{s}{b}<0.5 \tag{3.7}$$

Approximate expressions for the characteristic impedance Z_{oR} for a single ridge waveguide, based on the power-voltage impedance definition, have been also reported in [9], which is given by:

$$\frac{Z_{oR}}{Z_\infty}=\frac{1}{\sqrt{1-\left(\frac{F_c}{F}\right)^2}} \tag{3.8}$$

$$Z_\infty=\frac{\eta\, k_c S}{2\left(\sin(\theta_2)+u\cos(\theta_2)\tan\left(\frac{\theta_1}{2}\right)\right)} \tag{3.9}$$

3.3.2.2. Design Curves and Design Procedure

Based on the formulas presented in the previous section, the normalized cutoff wavelength with respect to the ridge waveguide width *(λ_c/a)* is calculated for different values of ridge normalized width *(W/a)* and depth *(u=S/b)*. This is achieved for both the fundamental TE_{10} mode and the first higher order mode, the TE_{20} mode using Eq. (3.3) through (3.7). For a ridge waveguide with width *a* and height *b*, it is well-know that there is no significant effect for the chosen ratio of *b/a* upon the corresponding bandwidth curves for different values of *u*. In other words, the choice of the ridge waveguide width would rather affect the cutoff frequencies which shifts the whole fundamental mode bandwidth without a significant change in the separation between the TE_{10} and the first higher order mode.

On the other hand, regarding the operational fundamental mode bandwidth, for the same values of b/a and W/a, the bandwidths increases significantly by reducing the ratio $u=S/b$ [9], [10]. Therefore, in our study, b has been chosen equal to 1.524 mm which represents a relatively thick available substrate allowing therefore a good flexibility in the choice of u. For this choice of substrate thickness, approaching small values of u less than 0.2 provides reasonable values for the substrate thickness that will be employed for the implementation of the microstrip access transition.

Fig. 3.10 shows the calculated normalized cutoff wavelength λ_{c10}/a as a function of W/a for different values of S/b. To obtain the bandwidth of the fundamental mode propagation, analogous curves are calculated for the TE_{20} mode for the same variations of S/b. The curves of Fig. 3.10 and Fig. 3.11 are calculated based on Eq. (3.5) and Eq. (3.6), respectively and the ratio of b/a is chosen approximately 0.2. In order to use the calculated curves of Fig. 3.10 through Fig. 3.12, frequencies F_1 and F_2 bounding the frequency band of interest are such that F_1 is smaller than the lowest frequency in the lower band and F_2 is larger than the highest desired operation frequency in the upper band. To cover the previously mentioned C/K dual band operation, frequencies F_1 and F_2 are set to 6.5 GHz and 26 GHz respectively. Therefore the ratio $\lambda_{c10}/\lambda_{c20}$ would be about 0.96. According to the choice of F_1, and for a value of a = 7mm, the ratio λ_{c10}/a would be 3.8.

For the lower frequency band to start propagating at a frequency F_1 of 6.5 GHz and for a value of a = 7 mm, the ratio λ_{c10}/a will be 3.8. To ensure a TE_{10} propagation up to a frequency F_2 such that F_2= 26 GHz, the ratio $\lambda_{c10}/\lambda_{c20}$ should have a value of 4. A ratio of W/a in the range between 0.2 up to 0.49 for $u=S/b$=1/6 can therefore satisfy these constraints. For simpler design and easier realization, the ridge width (W) has been kept almost constant for the outermost waveguide section and the outer ring. Therefore, to satisfy the impedance constraint of the ring coupler, this implies the decrease of the width of the ridge waveguide constituting the ring. Therefore, the value of W/a is preferable to be chosen in the positive slope part of the bandwidth curve of Fig. 3.12 (between 0.2 to 0.3 in our case) rather than the negative slope part. A similar procedure is followed to obtain primary dimensions for the inner ring coupler with its ridge waveguides feeding sections between the two rings. The inner r_{in} and outer r_{out} radii of each ring coupler are therefore given by Eq. (3.10) and Eq. (3.11), respectively.

$$r_{in(i)} = \frac{3\lambda_{g(i)}}{4\pi} - \frac{a_{(i)}}{2} \tag{3.10}$$

$$r_{out(i)} = \frac{3\lambda_{g(i)}}{4\pi} + \frac{a_{(i)}}{2} \tag{3.11}$$

Where the suffix i denotes each specific ring coupler with its corresponding waveguide wavelength $\lambda_{g(i)}$ and its width $a_{(i)}$.

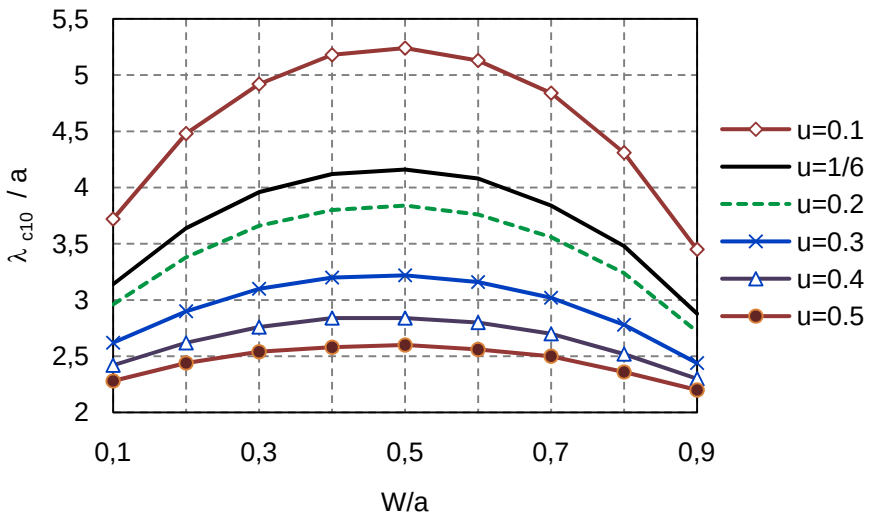

Fig. 3.10 TE_{10} mode normalized cutoff wavelength versus *W/a* for different values of *u=S/b*, *b/a*=0.2.

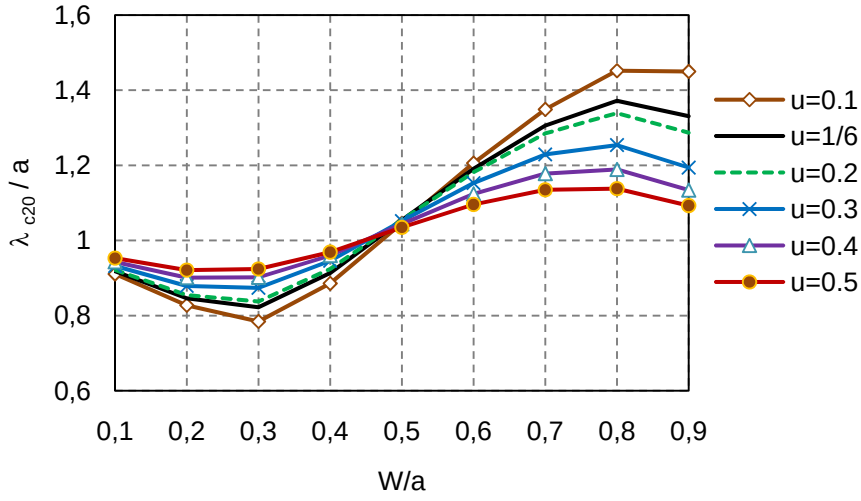

Fig. 3.11 TE_{20} mode normalized cutoff wavelength versus *W/a* for different values of *u=S/b*, *b/a*=0.2.

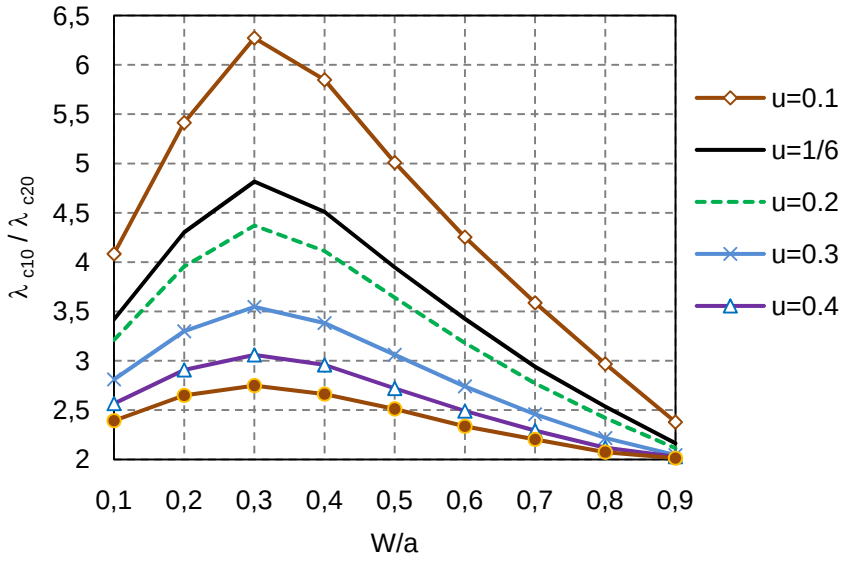

Fig. 3.12 Ratio between the fundamental mode cutoff and the first higher order mode versus *W/a* for different values of *u*.

Fig. 3.13 Phase constants of the ridged waveguide illustrating the cutoff frequencies of the TE_{10} and the TE_{20} modes.

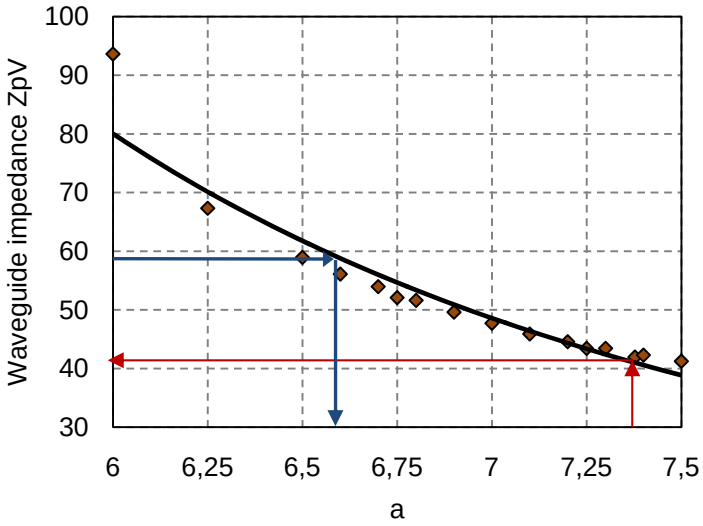

Fig. 3.14 Impedance variation of the ridged waveguide versus the width *a* (*b*=1.524mm, *S/b*=1/6, *W*=1.6mm). HFSS simulation is given by the continuous line while points curve represents calculated values.

As previously mentioned, the higher frequency band has to be guided towards the inner ring while forbidding its propagation in the outer one. This is achieved in the proposed design by loading the waveguide of the outer ring with equally spaced radial transverse slots centered above the quasi uniform field in the ridge section. These slots are loaded by short-ended stubs, Fig. 3.7.

The use of such defects to produce the required stopband has the double advantage to control the position of the bandgap by selecting the period between the slots (measured radially from the center of two successive slots) and controlling the effect of the slot defect by the loading waveguide. In fact, the spacing between the slots is chosen around half the waveguide wavelength corresponding to the center frequency of the stopband [18], [19]. On the other hand, for further control of the slots effect without disturbing the propagation characteristics for the lower band, the slots are loaded by a waveguide such that the waveguide is under cutoff for the lower band and starts propagation at a frequency that limits the lower bound of the stopband. To avoid radiation at the waveguide ends and therefore coupling between the different loading waveguide sections, the waveguides are short-ended. Such waveguide stubs in the used configuration are very compatible to the space constraints as well as to the SIW technology.

To measure the developed coupler, wideband microstrip to SIW transitions are need as shown in Fig. 3.15. As a matter of fact, the field distribution for a ridge

waveguide operating in the fundamental mode has a similar pattern at the center region as that of the quasi-TEM of the microstrip line. This pattern match becomes more obvious for the upper band case as the field becomes more confined in the ridged region. The optimization of the transition parameters follows therefore a similar procedure as that of [8] and concerns more the lower frequency band.

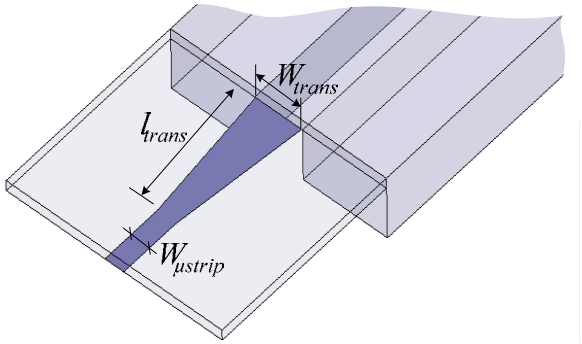

Fig. 3.15 Excitation of the RSIW using a wideband tapered microstrip transition.

3.3.3. Results and Discussion

Based on the primary values of the different design parameters obtained according to the previously discussed design procedure, the overall structure is optimized using Ansoft HFSS simulator. For a better control of the impedance characteristics seeking better improvement of the return loss and bandwidth, H-plane notches are introduced at junctions between the arms and the ring to the optimization parameters besides modifying the shape of the inner conductor of the smaller coupler. Analogous modifications are reported for SIW ring coupler [20] and T-type folded SIW ring coupler [21].

Table 3.2 summarizes the different dimensions of the overall structure after its optimization using HFSS. In Table 3.2, RSIW1, RSIW2, RSIW3 and RSIW4 refer to the ridged waveguide sections of the outermost arms, the outer ring coupler, the RSIW connecting the two rings and the inner ring, respectively. The H-plane notch at the junction between the outermost arm and the bigger ring has $\delta_x \times \delta_y$ dimensions of 0.83×0.83 mm^2. The stub length (L_s) and width (W_s) are 1.24 mm and 4.82 mm, respectively while the transverse coupling slots are 0.4 mm wide and 4.6 mm long and have a radial pitch size (P_s) of 2.84 mm. The separation distance (d) between the inner and outer rings is equal to 1.36 mm. The inner wall of the smaller ring coupler is modified as shown in Fig. 3.15 with $\delta_\theta = \pi/6$ rad and δ_r = 0.62 mm.

All RSIW sections have S=0.254 mm with b=1.524 mm and the coupler is designed on a 1.524 mm thick Rogers 6002 substrate with a relative permittivity of 2.94 and loss tangent tan (δ)=1.4×10^{-3}.

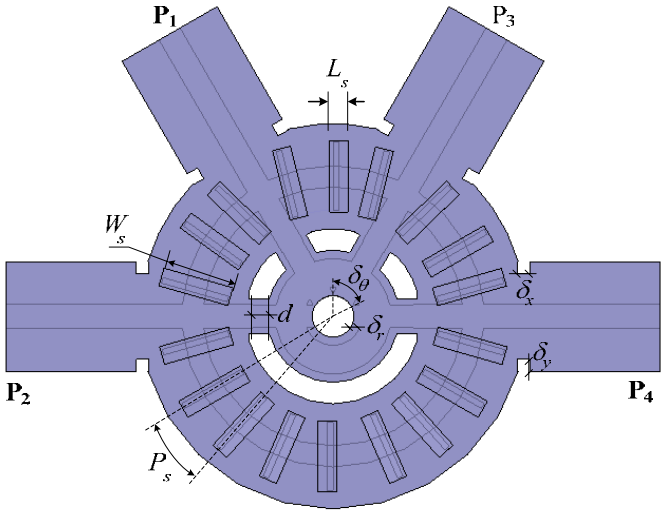

(a)

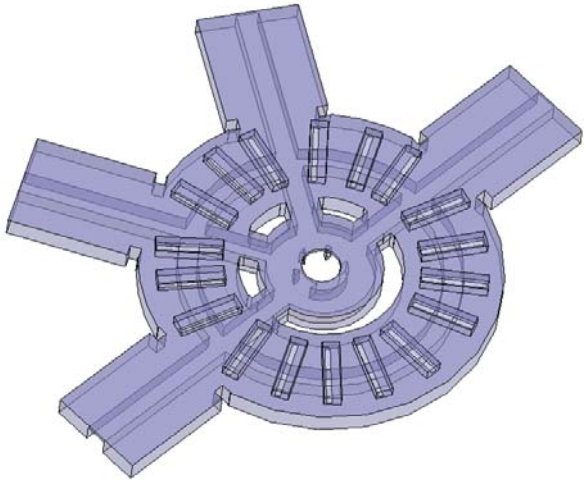

(b)

Fig. 3.16 Final optimized ridged waveguide concentric hybrid ring coupler.
(a) Top view. (b) 3-D view.

Table 3.2 Dimensions of the different ridged waveguide sections of the optimized dual band coupler of Fig. 3.16.

	RSIW1	RSIW2	RSIW3	RSIW4
a (mm)	7.377	7.087	2.350	3.410
W (mm)	1.627	1.43	1.547	1.947
W/a	0.22	0.20	0.67	0.57

Fig. 3.17 shows the stopband effect introduced by the transverse stub-loaded radial slots in the outer ring coupler at the upper frequency band. The simulation results correspond to the previously mentioned optimized dimensions for the outer loaded ring only (see the inset in Fig. 3.17). The subs are implemented within the same dielectric material with a height of 0.762 mm. According to the width of the employed waveguide stubs, the cutoff frequency of these latter ones is about 18 GHz which limits the lower bound of the stopband. Coupling values below -12 dB are observed over the frequency range from 19 GHz up to the cutoff frequency of the TE_{20} mode around 28 GHz.

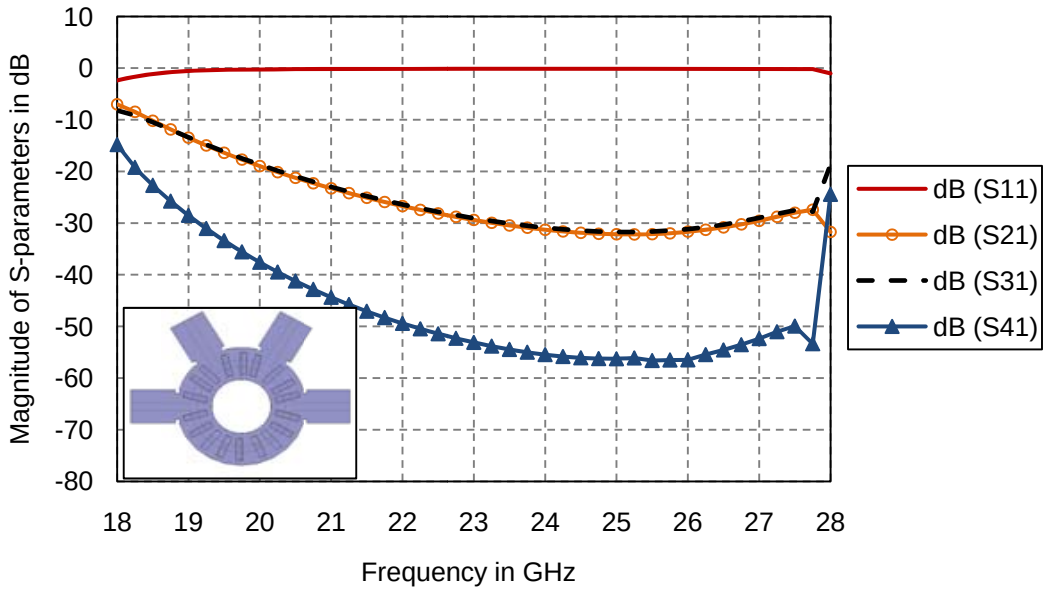

Fig. 3.17 Simulated magnitudes of the S-parameters illustrating the stopband introduced in the upper frequency band response of the outer ring.

Simulated results for the coupler structure of Fig. 3.16 are shown in Fig. 3.18 through Fig. 3.20. For the C-band operation, a bandwidth of about 9% around a center frequency of 7.2 GHz is achieved. The bandwidth is calculated with reference to -20 dB reflection loss. The insertion loss at the coupled ports undergoes less than 1 dB maximum dispersion, with respect to the theoretical -3 dB, over the entire frequency band (6.84 GHz -7.5 GHz). The isolation level remains below 20 dB over the entire band. The phase differences between the coupled ports are 0±10° and 180°±10° when feeding from port 1 and 2, respectively.

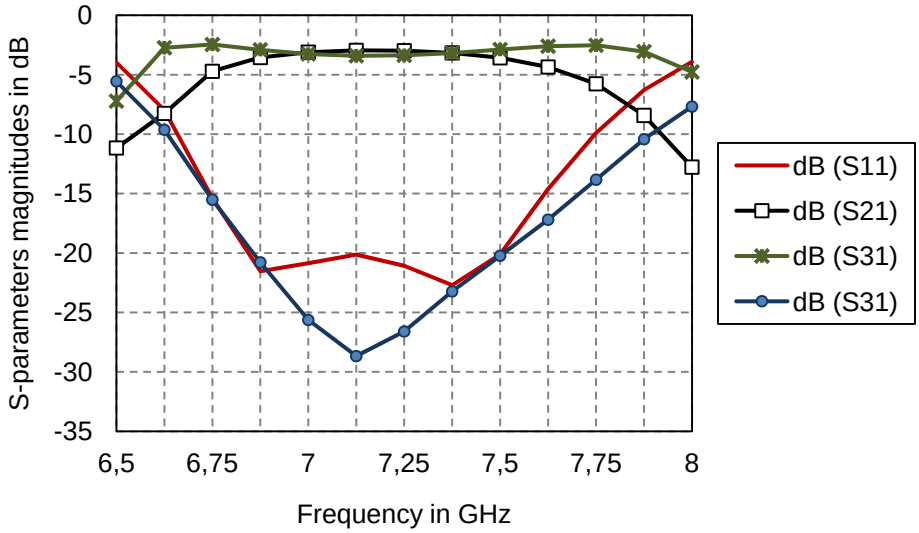

Fig. 3.18 Simulated S-parameters magnitudes for feeding from port 1 for C-band operation.

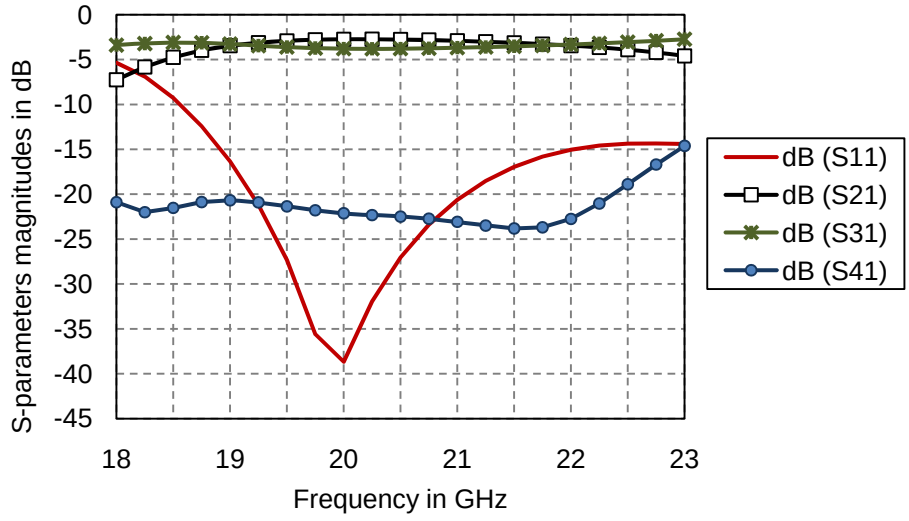

Fig. 3.19 Simulated S-parameters magnitudes feeding from port 1 for K-band operation.

For K-band operation, a bandwidth of 9.3% with a center frequency around 20 GHz is obtained for the -20 dB reflection loss. Wider performance is observed regarding a maximum dispersion in the insertion loss values at the coupled ports which remain less than 1 dB over a bandwidth of 14.6% around 20.5 GHz. The reflection and isolation losses remain lower than -15 dB and -20 dB, respectively, over the extended band. The phase differences between the coupled ports are 0±10° and 180°±10° when feeding from port 1 and 2, respectively, over the extended band.

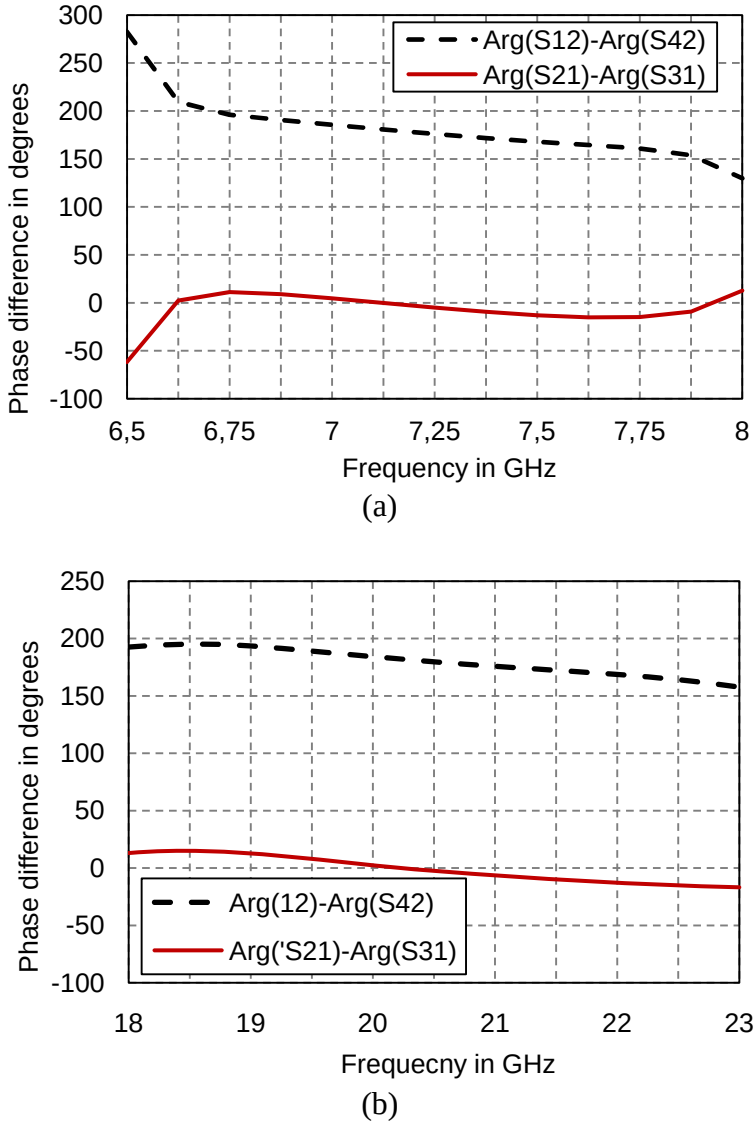

Fig. 3.20 Simulated phase differences between the coupled ports for excitations at ports 1 and 2. (a) C-band operation. (b) K-band operation.

Fig. 3.21 illustrates the field patterns for the electric field magnitudes at both frequency bands obtained using Ansoft HFSS. It can be seen that a good confinement of the field is achieved at each frequency band with equal power split between the coupled ports.

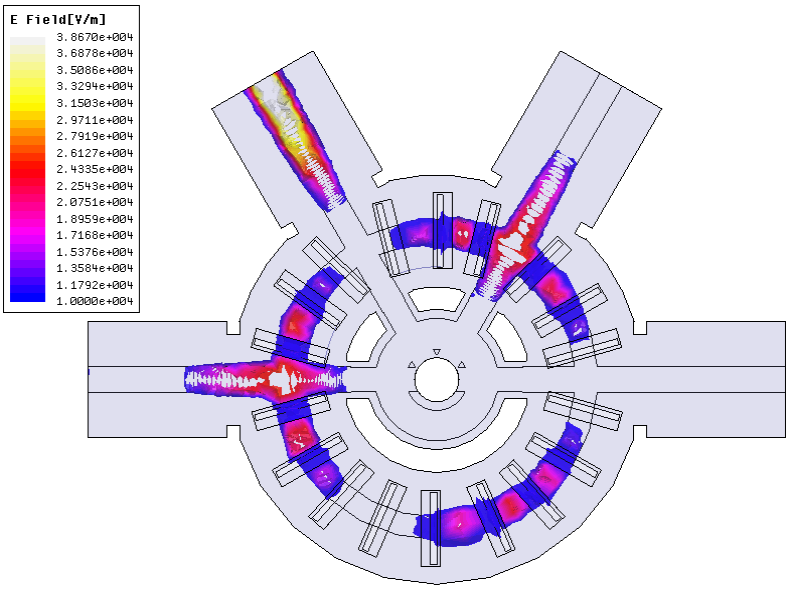

(a)

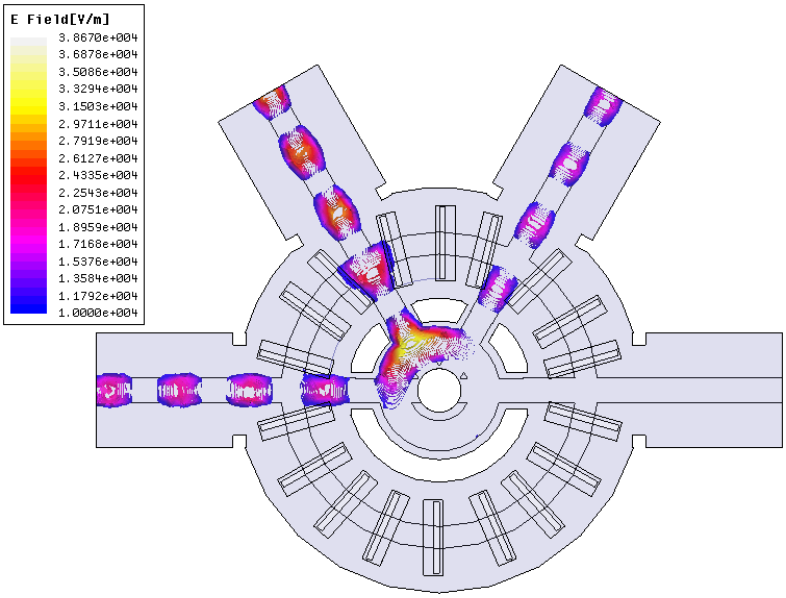

(b)

Fig. 3.21 Simulated electric field magnitude patterns.
(a) Field pattern at 7.2 GHz. (b) Field pattern at 20.5 GHz.

3.3.4. Conclusion

A novel dual-band hybrid ring coupler is developed in multi-layer RSIW technology. The coupler has an original structure based on two concentric rings in RSIW topology with the outer ring loaded with radial, equally spaced stub-loaded transverse slots. A design procedure is presented based on the TRM of the ridged waveguide together with the simple design rules of the hybrid ring coupler. The coupler provides independent dual band operation with low-dispersive wideband characteristics. The maximum separation between the lower and upper frequency bands is limited by the employed ridged waveguide maximum operational bandwidth. The minimum separation between two separate adjacent frequency bands is compromised by the occupied are of the coupler. When the two required frequency bands are close to each other, one additional waveguide wavelength can be added to the outer ring coupler extending the distance between its adjacent arms from $\lambda_g/4$ to $5\lambda_g/4$ allowing a larger degree of freedom for the inner ring coupler.

Future work will first focus on mapping the design of the ridged waveguide coupler into a multi-layer design for simpler fabrication and measurement. The coupler design adopted so far has been based on an implementation employing a thick substrate while the ridge is mechanically grooved in it. Although this technique has the advantage of a simpler mapping between the waveguide structure and its analogous SIW realization, it has a main disadvantage which is the alignment of the microstrip access transitions that are realized separately and then soldered to the access ridge waveguides. Mapping this structure into a multilayered design, in which the microstrip line, microstrip taper and the horizontal part of the ridge are printed over the same substrate while synthesizing the vertical wall of the ridge by metalized via holes or grooves, seems more promising for a robust and reliable realization.

References of Chapter Three

[1] A. Ali, N. Fonseca, F. Coccetti and H. Aubert, "Novel two-layer broadband 4x4 Butler matrix in SIW technology for Ku-band applications," *Asia-Pacific Microwave Conf.*, Dec. 2008.

[2] T. Djerafi and K. Wu, "Super-compact substrate integrated waveguide cruciform directional coupler," *IEEE Microwave Wireless Compon. Lett.*, vol.17, pp. 757-759, Nov. 2007.

[3] G. Zhai, W. Hong, K. Wu, J. Chen, P. Chen and H. Tang, "Substrate integrated folded waveguide (SIFW) narrow wall directional coupler," *International Conf. on Microw. and Millimeter Wave Technology*, April 2008.

[4] N. Grigoropoulos, B. S. Izquierdo and P. R. Young, "Substrate integrated folded waveguides (SIFW) and filters," *IEEE Microwave Wireless Compon. Lett.*, Vol.15, No. 12, pp. 829-831, Dec. 2005.

[5] L. Yan, W. Hong, G. Hua, J. Chen, K. Wu, and T. Cui, "Simulation and experiment on SIW slot array antennas," *IEEE Microwave Wireless Compon. Lett.*, Vol.14, pp. 446-448, Sept. 2004.

[6] S. R. Rengarajan, "Compound radiating slots in a broad wall of a rectangular waveguide, " *IEEE Trans. Antennas Propagat.*, Vol. 37, No. 9, pp. 1116-1123, Sept. 1989.

[7] J. Nolen, "Synthesis of multiple beam networks for arbitrary illuminations," *Ph. D. thesis*, Bendix corporation, radio division, Baltimore, April 1965.

[8] D. Deslandes and K. Wu, "Integrated microstrip and rectangular waveguide in planar form," *IEEE Microwave Compon. Lett.*, vol. 11, pp. 68-70, Feb. 2001.

[9] S. B. Cohn, "Properties of ridge wave guide," *Proceedings of the IRE*, Vol. 35, No. 8, pp. 783-788, Aug. 1947.

[10] S. Hopfer, "The design of ridged waveguides," *IRE Trans. Microw. Theory Techn.*, Vol. 3, No. 5, pp. 20-29, Oct. 1955.

[11] Y. Utsumi, "Variational analysis of ridged waveguide modes," *IEEE Trans. Microw. Theory Tech.*, Vol. 33, No. 2, pp. 111-120, Feb. 1985.

[12] T. Kitazawa and R. Mittra, "Analysis of finline with finite metallization thickness," *IEEE Trans. Microw. Theory Tech.*, Vol. 32, No. 11, pp. 1484-1487, Nov. 1984.

[13] W. Sun and C. Balanis, "MFIE analysis and design of ridged waveguide," *IEEE Trans. Microw. Theory Tech.*, Vol. 41, No. 11, pp. 1965-1971, Nov. 1993.

[14] T. S. Chen, "Calculation of the parameters of ridge waveguide," IRE *Trans. Microw. Theory Techn.*, Vol. 5, No. 1, pp. 12-17, Jan. 1957.

[15] W. Hoefer and M. Burton, “Closed form expressions for the parameters of finned and ridged waveguides,” *IEEE Trans. Microw. Theory Tech.*, Vol. 30, No. 12, pp. 2190-2194, Dec. 1982.

[16] N. Marcuvitz, “Waveguide handbook,” MIT Rad. Lab. Series, Vol. 10, pp. 399-402.

[17] J. R. Whinery and H. W. Jamieson, “Equivalent circuits for discontinuities in transmission lines,” Proceeding of the IRE, Vol. 32, pp. 98-116, Feb. 1944.

[18] V. Radisic, Y. Qian, R. Coccioli, and T. Itoh, “Novel 2-D Photonic Bandgap Structures for Microstrip Lines,” *IEEE Microw. Guided Wave Lett.*, Vol. 8, No.2, pp.69-71, Feb., 1998.

[19] F. R. Yang, K. P. Ma, Y. Qian, and T. Itoh, “A novel TEM waveguide using uniplanar compact photonic-bandgap (UC-PBG) structure,” *IEEE Trans. Microw. Theory Tech.*, Vol. 47, No. 11, pp. 2092–2098, Nov. 1999.

[20] W. Che, K. Deng, E. K. N. Yung and K. Wu, “H-plane hybrid ring of high isolation in substrate-integrated rectangular waveguide,” *Microw. Opt. Tech. Lett.*, Vol. 48, No. 3, pp. 502-505, March 2006.

[21] Y. Ding and K. Wu, “Miniaturized hybrid ring circuits using T-type folded substrate integrated waveguide,” *IEEE MTT-S*, pp.705-708, June 2009.

CHAPTER FOUR

Two-Layer Wideband SIW Beam-Forming Matrices

4.1. Introduction

Multi-beam antennas have become a key element in nowadays wireless terrestrial and spatial communication systems where increased channel capacity, improved transmission quality with minimum interference and multipath phenomena are severe design constraints. These antennas are classified in two main categories namely adaptive smart antennas and switched-beam antennas.

Switched-beam antennas consist of an elementary antenna array connected to a Multiple Beam Forming Network (M-BFN) characterized by a number of inputs equal to the number of beams to produce and a number of outputs equal to the number of elementary radiators in the antenna array [1]. Such antennas are extensively used in Space Division Multiple Access (SDMA) applications [2]. The M-BFN subsystem can also be used in Multi-Port Amplifiers (MPA) for distributed amplification. This technique is used in satellite communication systems to ensure similar optimum efficiency for all amplifiers [3]. Since the early 1960's, different solutions have been proposed, such as Blass matrix [4], Nolen matrix [5], Rotman lense [6] and Butler matrix [7].

This chapter focuses on the design of a wideband, compact, Butler matrix employing the previously developed SIW components. Prior to the Butler matrix design, the phase compensation of the previously designed two layer coupler is investigated, and then an SIW two-layer layout for a 4x4 Nolen matrix is presented where the design limitations are identified. Due to the bandwidth limitations facing

the Nolen configuration and its numerous components, the Butler matrix attracted our attention especially for the investigation of the two-layer SIW design.

As a matter of fact, among the different types of BFNs, the Butler matrix has received particular attention in literature as it is theoretically lossless and employs the minimum number of components to generate a given set of orthogonal beams, provided that the number of beams is a power of 2. However, the Butler matrix has a main design problem which is the presence of path crossings. To overcome this problem, some specific designs have been suggested but they are not easily scalable for larger matrices [8], [9]. Another well-known method for single-layer realizations is to employ extra 0dB couplers by means of back-to-back pairs of 3 dB couplers to produce the crossover transfer function [3], [10]. This leads therefore to an increased number of components with increased losses especially for larger matrices. In [11] a Lange coupler is used to replace the crossover offering therefore an interesting planar design with wideband performances. However, the complete structure is rather adapted to micro strip technology as it requires wire bonding.

Two-layer designs are also found in literature ensuring a solution for the crossing arms problem. In [12], a complete waveguide-based structure has been reported for a narrow-band Butler matrix. Although a compact area layout was proposed, the use of classical waveguides leads to a bulky structure. Good performances have also been obtained using a multilayered design with suspended stripline technology [13]. However, the circuit suffers from a linear phase variation with frequency despite its fabrication complexity. A coplanar waveguide-based two-layer structure is suggested in [14]. However, this solution suffers from being narrow band for both transmission magnitude and phase consequently, it is very sensitive to technological inaccuracies.

In this chapter, a two-layer compact 4x4 Butler matrix is proposed in SIW technology offering wideband performances for both transmission magnitudes and phases with good isolation and input reflection characteristics. The use of SIW technology appears as a good compromise as it combines the advantages of classical rectangular waveguides while being compatible with standard low-cost printed circuit board technology [15]. Owing to its attractive features, a number of implementations for BFNs have been recently developed in SIW technology [16-19]. The structure is therefore suitable for both waveguide-like and planar structures.

The use of the two-layer SIW implementation is explored through a two-fold enhancement approach for both the matrix electrical and physical characteristics. On one hand, the two-layer topology allows an inherent solution for the crossing problem allowing therefore more flexibility for phase compensation over a wide frequency band. This is achieved by proper geometrical optimization of the surface on each layer and exploiting the SIW technology in the realization of variable width waveguides sections with the corresponding SIW bends. On the other hand, the two-layer SIW technology is exploited for an optimized space saving design by implementing common SIW lateral walls for the matrix adjacent components seeking maximum size reduction.

The two-layer transverse slot-coupled SIW transition is used as a low-loss guiding element between the two layers of the matrix. To demonstrate the validity of our design, two different configurations of the 4x4 Butler matrix are designed, optimized and implemented. Simulated and measured results are in good agreement for the separate constituting elements as well as for the complete matrix.

This chapter is organized as follows. Section 4.2 presents a brief overview on the Nolen matrix architecture and design considerations. A two-layer layout is developed and bandwidth limitations are shown through the simulated results of a developed two-layer layout. Section 4.3 presents the Butler matrix, where Section 4.3.1 presents the architecture and design considerations of the Butler matrix. Section 4.3.2 focuses on the design and realization of two different configurations of 4x4 Butler matrices employing the previously developed components. Experimental results are presented in details for both matrix prototypes. Measured transmission magnitudes and phases are then used to calculate the radiation pattern for a theoretical 4-element antenna array followed by conclusions in Section 4.3.3.

4.2. Two-Layer 4x4 SIW Nolen Matrix

This section presents an investigation of the possibility to use the previously designed components for the design of compact Nolen matrix and the associated limitations. A layout of a 4×4 Nolen matrix is proposed in two-layer topology. Magnitude and phase characteristics of the matrix are investigated through Agilent ADS simulations by cascading the scattering matrices of the matrix elements according to the presented layout.

4.2.1. Nolen Matrix Architecture

The general form of a Nolen matrix is illustrated in Fig. 4.1, where the *N* output ports are coupled to *M* input ports [20], [21]. This matrix has been introduced by J. Nolen few years later than the Blass [4], and Butler [7] matrices as a modification to the Blass matrix. The Nolen matrix combines properties from both latter matrices, as it is a series feed network, as the Blass matrix, and it is lossless (produces orthogonal beams), as the Butler matrix. Each node in Fig. 4.1 consists of a directional coupler, represented by a coupling value $\sin\theta_{ij}$, and a phase shifter with a phase shift of ϕ_{ij}. These parameters have been studied in [22] for the calculations of Blass matrices then used in the particular case of orthogonal beams, producing therefore the Nolen matrix, in [23]. Theoretical parameters for the directional couplers and phase shifters for the matrix of Fig. 4.1 are summarized in Table 4.1.

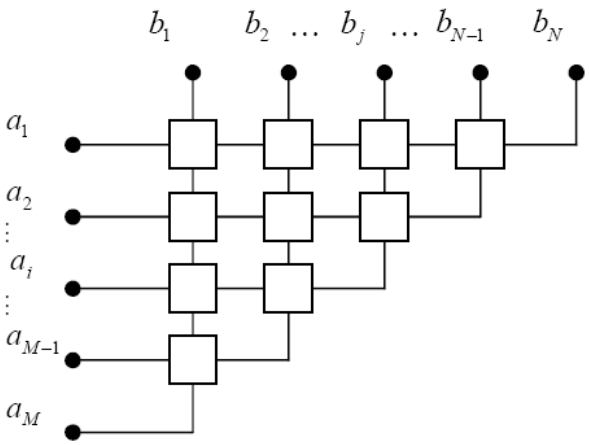

(a)

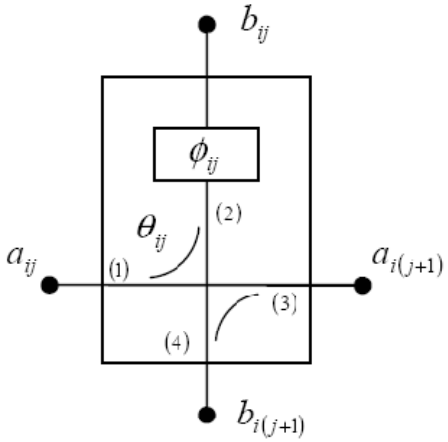

(b)

Fig.4.1 (a) General form of a Nolen matrix. (b) Detailed node, [22], and [23].

Table 4.1 Design parameters of the directional couplers ($\sin\theta_{ij}$) and phase shifters (ϕ_{ij}) for a 4×4 Nolen matrix

	1	2	3	4
1	0.500 0°	0.577 45°	0.707 90°	1.000 135°
2	0.577 180°	0.500 0°	1.000 180°	
3	0.707 90°	1.000 0°		
4	1.000 0°			

4.2.2. Two-Layer SIW Nolen Matrix

According to Table 4.1, three different couplers and 4 different phase shifters are needed to realize the 4x4 Nolen matrix. The matrix is designed to operate at 12.5 GHz center frequency. The two-layer coupler presented in chapter three will be used together with the equal-length, variable width phase shifters and the two-layer transition discussed in chapter two. The simulated scattering parameters of the three couplers are shown in Fig. 4.2 and their performances are summarized in Table 4.2.

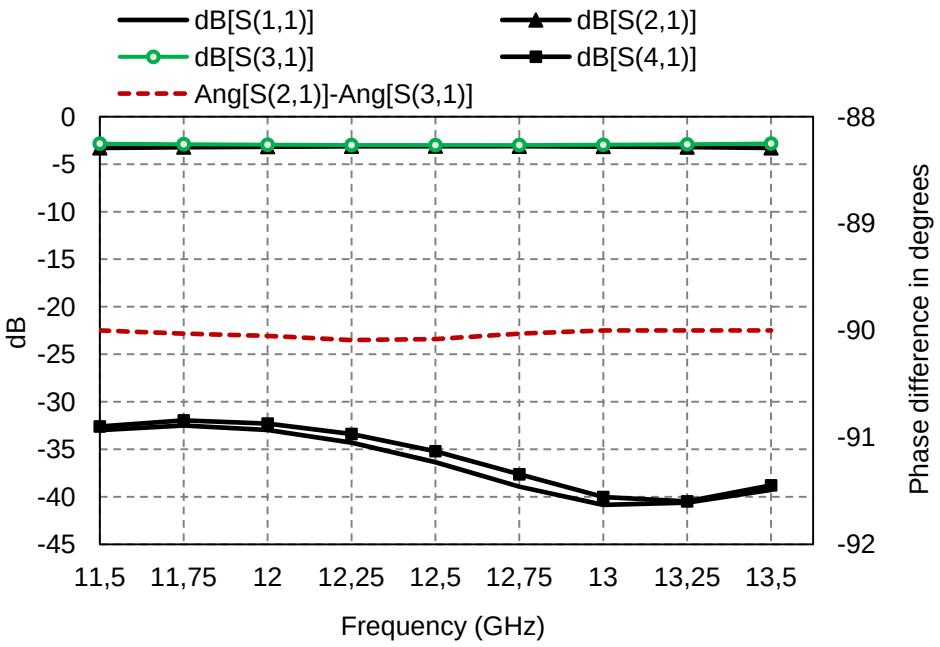

(a)

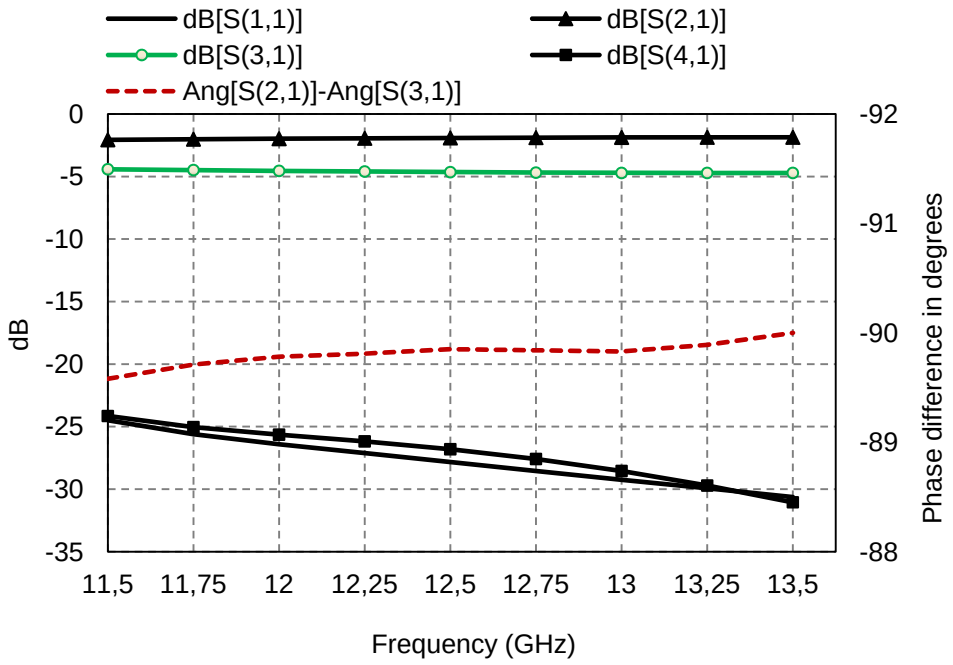

(b)

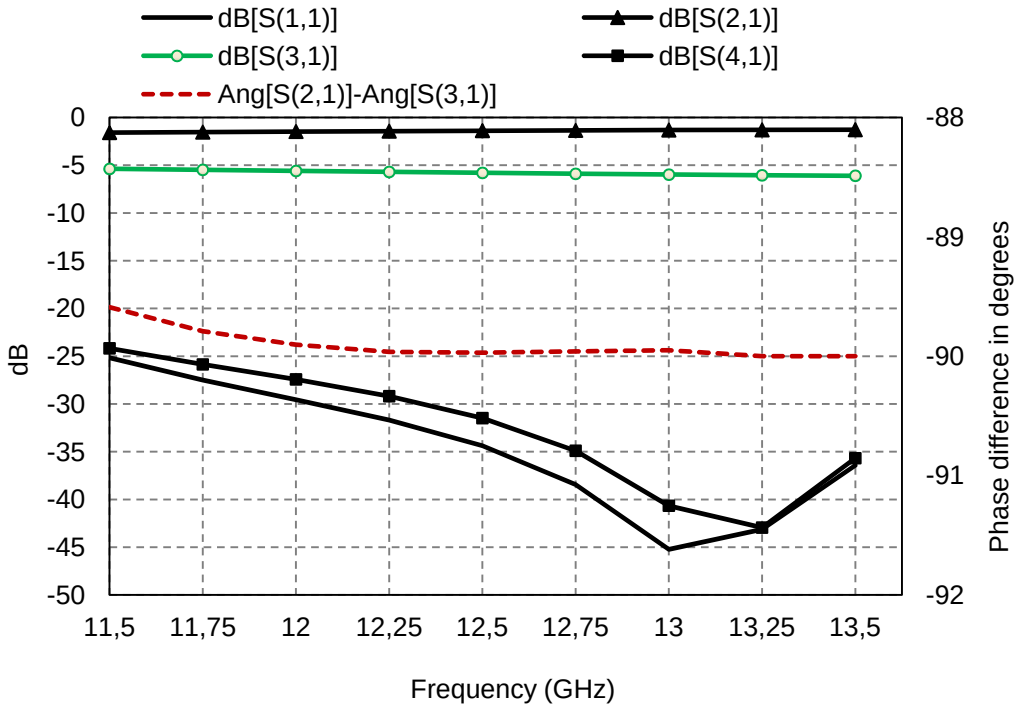

(c)

Fig. 4.2 Scattering parameters and phase difference between the direct and coupled ports for different coupling levels (a) 3.02 dB coupler. (b) 4.77 dB coupler. (c) 6.02 dB coupler.

Fig. 4.3 shows the proposed layout for 4x4 Nolen matrix. Ports 1 to 4 are the input ports while ports 5 to 8 are the output ones. The hollow circles in Fig.4.3 indicate the SIW lateral walls of the bottom layer while the black ones are used for the upper layer with the two-layer transition being used at the end of each input line of the matrix. Therefore, the matrix consists of 6 couplers used in the horizontal direction with SIW connecting sections between the different couplers as well as wideband equal length variable width SIW phase shifters used in the vertical direction. The used phase shifters are those presented in chapter two.

Tracing the phase progression along the different stages of the matrix, for instance for feeding from port 1, and by considering the phase quadrature between the direct and coupled ports of the coupler, the phases at the output ports of the matrix of Fig. 4.3 will be ϕ_c+90°, $2\phi_c$+$\Delta\phi$+45°, $3\phi_c$+2$\Delta\phi$ and $4\phi_c$+3$\Delta\phi$-45° for ports 5 to 8 respectively, where ϕ_c is the transmission phase of the coupler, that is ϕ_c = Arg (S_{21}) and $\Delta\phi$ is the propagation phase delay of the SIW sections connecting two successive couplers in the same horizontal line, Fig. 4.3. These phase values are obtained such that, to maintain a systematic design, the branch with the 0 dB coupler at the end of each line introduces a phase delay given by $\Delta\phi$ + ϕ_c. In fact, these values have a linear dependence with frequency due to the series feed topology of the matrix. On the other hand, to satisfy the relative phases given by Table 4.1 at the design center frequency, all couplers must provide almost similar values of ϕ_c. Therefore, the phase compensation discussed in chapter three for the parallel waveguide coupler is needed for the matrix design; Table 4.2 summarizes the different parameters of the couplers with and without phase compensation. Then SIW sections whose phase propagation delay is $\Delta\phi$ have lengths such that ϕ_c+$\Delta\phi$ is an integer multiple of 2π.

The simulated scattering amplitude and phase parameters at the output ports of the matrix are shown in Table 4.3 and Table 4.4, respectively, for different input ports, while simulated isolation and return loss amplitudes are shown in Table 4.5. By comparing both theoretical and simulated results of Tables 4.3 and 4.4, there is a great agreement with maximum amplitude error of 0.054 and maximum phase error of 1.6°. The highest return loss value is for an input at port 3 and corresponds to 16 dB losses.

Table 4.2 Parameters and simulation results for the three SIW couplers over the 12-13 GHz band

Coupling Level (*dB*)	**3.02**	**4.77**	**6.02**
SIW width "a_{SIW}" *(mm)*	11.85 (11.5)	11.85 (11.72)	11.85
Slot Length *(mm)*	13.05 (12.95)	11.2 (11.15)	10.6
α°	15 (4)	16 (6)	9
d_offset *(mm)*	2.65 (2.7)	3 (3.2)	3.2
Coupling peak-to-peak error *dB*	+0.04/0 (+0.14/-0.05)	+0.12/-0.07 (+0.16/-0.12)	+0.29/-0.26
Arg (S21) at 12.5 GHz *(°)*	-159.35 (-144.27)	-149.29 (-144.14)	-144.19

Table 4.3 Simulated Amplitude Output Excitation Laws at 12.5 GHz

	5	**6**	**7**	**8**
1	0.510	0.491	0.485	0.469
2	0.475	0.472	0.448	0.463
3	0.446	0.449	0.466	0.455
4	0.469	0.458	0.488	0.470

Table 4.4 Simulated phase output excitation laws at 12.5 GHz (Theoretical Values)

	5	**6**	**7**	**8**
1	0 (0)	-45.314 (-45)	-91.063 (-90)	-134.915 (-135)
2	0 (0)	135.287 (135)	269.064 (270)	44.096 (45)
3	0 (0)	-135.621 (135)	88.406 (90)	-46.251 (-45)
4	0 (0)	45.182 (45)	89.75 (90)	134.752 (135)

Table 4.5 Simulated isolation and return loss at 12.5 GHz

	1	**2**	**3**	**4**
1	0.098	0.141	0.037	0.034
2	0.143	0.113	0.045	0.123
3	0.037	0.044	0.151	0.142
4	0.035	0.124	0.144	0.113

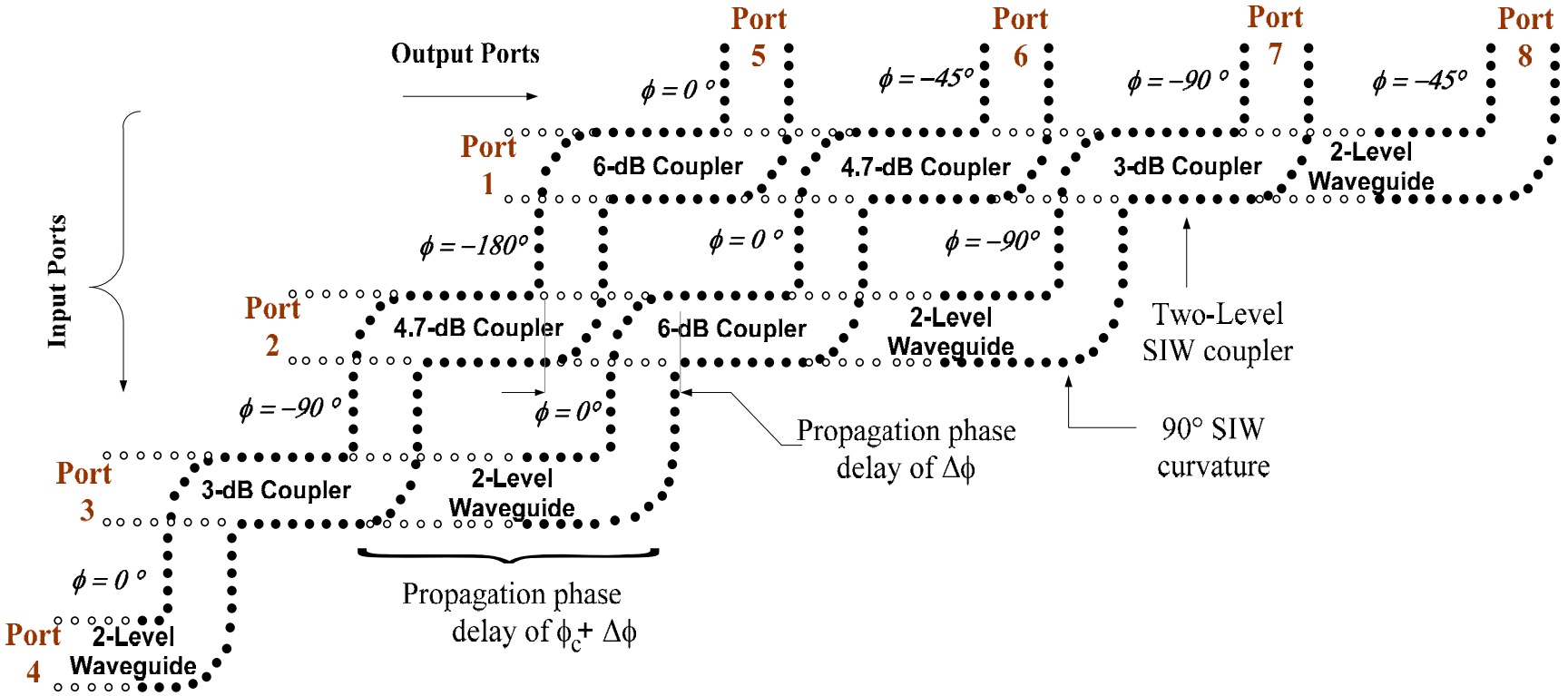

Fig.4.3 Schematic layout of the proposed double-layer 4x4 SIW Nolen matrix.

4.2.3. Conclusion

A two-layer layout for a 4x4 Nolen matrix is presented in SIW technology. The previously studied parallel waveguide coupler is used in the design. The use of the wideband coupler offers a good flexibility in the design of the Nolen matrix, while satisfying both amplitude and phase laws at its outputs at a specific frequency. However, due to the series feed type used in such a matrix, the phase gradients at the matrix output exhibit linear phase dependence, limiting the bandwidth. Such frequency dependence may be exploited to compensate the beam-squint of the matrix when used to feed a linear antenna array. Some investigations about such compensation have been addressed in [23]. The two-layer design together with the developed coupler topology appears as a good candidate for the implementation of two-layer wideband Butler matrices.

4.3. Two-Layer Compact Wideband Butler Matrices

4.3.1. Butler Matrix: Architecture and Design Considerations

Fig. 4.4 shows the basic layout of a 4x4 Butler matrix using 3dB/90° hybrids. The figure is a direct schematic mapping for the matrix general layout in a two-layer topology. The Butler matrix, being square, has N input ports coupled to N output ports ($N=2^n$) through a certain number of hybrid couplers and phase shifters. Being theoretically lossless [26], the Butler matrix produces N orthogonal beams when associated with a linear antenna array [20].

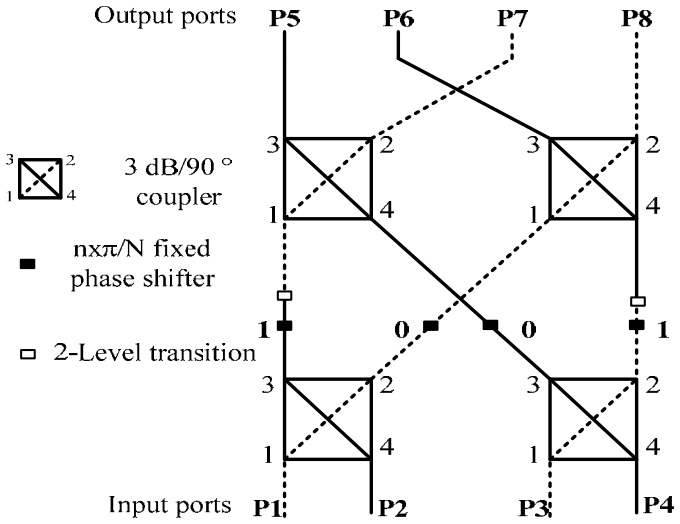

Fig. 4.4 General block diagram of a 4x4 Butler matrix with 3dB/90° couplers schematically mapped to a two-layer topology.

For an $N \times N$ matrix employing 90° hybrid couplers, the total number of phase shifters is $N(n\text{-}1)/2$, used in a symmetrical matrix topology. Each input port is associated to a specific linear phase gradient (φ) at the output ports orienting, therefore, the main beam towards a corresponding direction (θ_o) such that:

$$\varphi = (2m-1)\frac{\pi}{N}, \quad m \text{ integer}, m \in \left[1 - N/2, N/2\right] \tag{4.1}$$

$$\theta_o = \sin^{-1}\left(\frac{\lambda}{d_s}\frac{\varphi}{2\pi}\right) \tag{4.2}$$

One value of m is assigned for each input port. d_s is the inter-element spacing of the antenna array and λ is the free space wavelength.

It is noteworthy that, the phase gradient values of Eq. (4.1) as well as the number of phase shifters would be different for the case of the Butler matrix employing 180° hybrids, resulting in an asymmetric distribution of the phase shifters. The number of couplers remains however the same for both cases and is equal to $Nn/2$ for both matrices. The theoretical scattering parameters relating the outputs to the inputs of the matrix of Fig. 4.4 is given by:

$$S = \frac{1}{2}\begin{bmatrix} 1 & e^{-j\frac{3\pi}{4}} & e^{-j\frac{\pi}{2}} & e^{-j\pi} \\ e^{-j\frac{\pi}{4}} & 1 & e^{-j\frac{5\pi}{4}} & e^{-j\frac{3\pi}{4}} \\ e^{-j\frac{\pi}{2}} & e^{-j\frac{5\pi}{4}} & 1 & e^{-j\frac{\pi}{2}} \\ e^{-j\frac{3\pi}{4}} & e^{-j\frac{\pi}{2}} & e^{-j\frac{3\pi}{4}} & e^{-j\frac{\pi}{4}} \end{bmatrix} \tag{4.3}$$

Regarding the matrix dimensions and its numerous components, each component is first designed and optimized separately according to the required specifications and a properly optimized geometrical layout to reduce the computational burden of the electromagnetic simulation and optimization of the complete matrix. The matrix components are the wideband two-layer SIW coupler, variable width, compensated length wideband SIW phase shifters and the low-loss SIW layer transition. The optimized components are presented in the following sections.

For the Butler matrix, hereby presented, the separate components as well as the complete matrix is simulated and optimized using the FEM-based Ansoft HFSS simulator. The substrate used is the Rogers-Duroid 6002 with dielectric constant ε_r = 2.94, thickness h = 0.508mm and loss tangent tan δ = 1.7×10^{-3}. The via hole diameter is 0.78mm while the pitch size p = 1.3 mm. Conductor and dielectric losses are taken into account in the electromagnetic simulations, while the added microstrip to SIW access transitions are de-embedded in the measurements [15]. For all the measurements presented in this work, an Anritsu 37397D network analyzer is used with standard TRL calibration.

4.3.2. Developed 4×4 Butler Matrix

Fig. 4.5 shows the structure of the used two-layer SIW coupler. This coupler has been presented in details in chapter three. Based on the parametric study and performance, the coupler is optimized for a 3dB coupling value in the 11-14 GHz frequency band with 90° phase lead of the coupled port with respect to the direct one. The theoretical scattering matrix is given by Eq. (4.4), where ϕ is the propagation phase delay between an input port and its corresponding direct port.

$$S=\frac{e^{j\phi}}{\sqrt{2}}\begin{bmatrix} 0 & 1 & e^{j\pi/2} & 0 \\ 1 & 0 & 0 & e^{j\pi/2} \\ e^{j\pi/2} & 0 & 0 & 1 \\ 0 & e^{j\pi/2} & 1 & 0 \end{bmatrix} \tag{4.4}$$

Simulated and measured S-parameters of the designed coupler are shown in Fig. 4.6. The simulated results (access transitions are not included in the simulations) show a peak-to-peak error for the coupling coefficient less than 0.5 dB over the 11-14 GHz frequency band, while both isolation and reflection coefficients are below -20 dB with a relative phase difference which is almost constant at -90°.Measured results are in good agreement with the simulated ones. The measured reflection and isolation coefficients are lower than -20 dB over the entire band with a measured peak-to-peak error of 0.6 dB for the coupling coefficient. On the other hand, the measured and simulated phase differences are also in good agreement with less than 5° peak-to peak error over the entire frequency band.

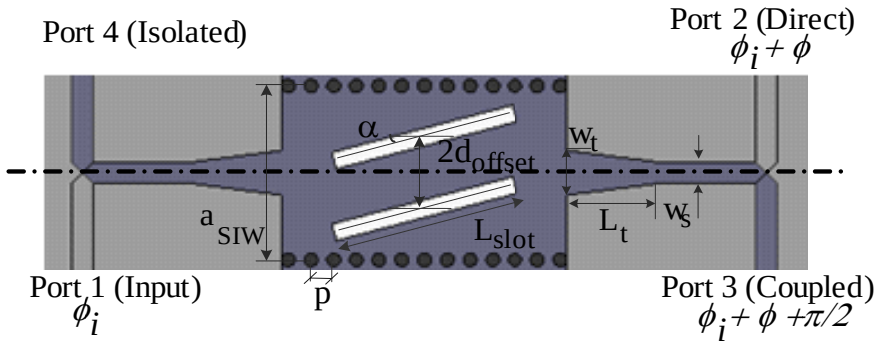

Fig. 4.5 The developed two-layer SIW coupler structure with microstrip to SIW transitions. a_{SIW} = 10.2 mm, L_{slot} = 10.7mm, d_{offset}=2.1mm, α=15°, slot width 1 mm, w_t=2.6mm, L_t=4.9mm and w_s=1.29mm.

In this section, the previously designed components are combined to form the foreseen two-layer 4x4 Butler matrix. Seeking wideband performance, for both magnitude and phase, implies wideband characteristics for all matrix elements. The phase shifter becomes therefore a crucial component in the matrix in order to provide the required wideband phase shift with low insertion loss.

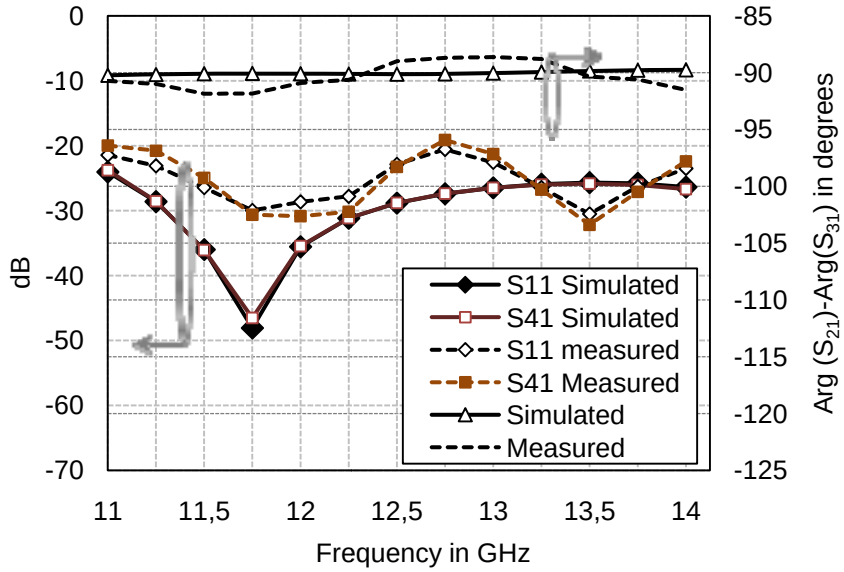

(a)

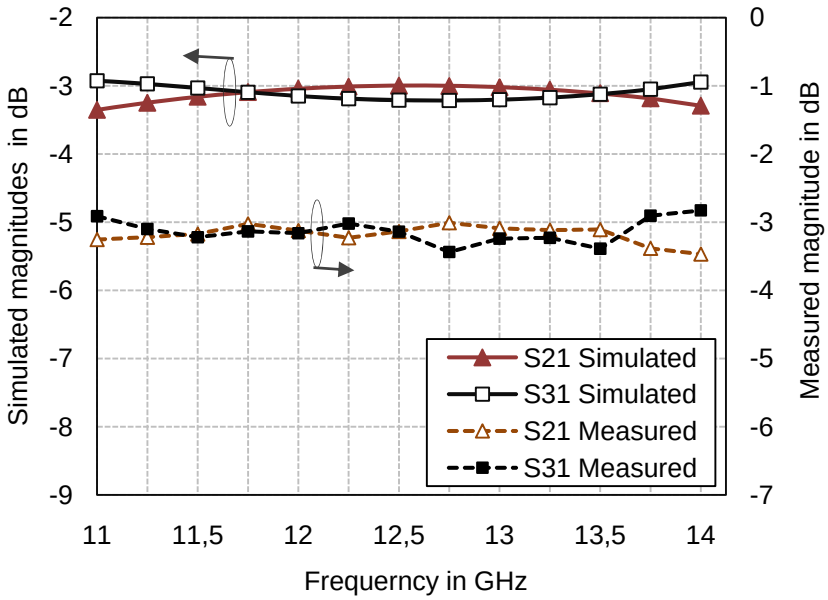

(b)

Fig. 4.6 Simulated and measured S-parameters for the two-layer SIW hybrid coupler: (a) Reflection and isolation magnitudes. (b) Direct and coupled magnitudes with the phase difference between the direct and coupled ports.

Referring to Fig. 4.4, the required phase delay can be achieved by properly increasing the SIW width of the outer arms a_{SIWo} with respect to that of the inner ones, denoted by a_{SIWi}. The phase curves of both arms will maintain almost the same slope over a wide frequency range [16], [25]. However, as the two-level transition is integrated within the former SIW arms, additional frequency-dependent phase delay with a different slope due to the transverse slot will be added to their transmission phases degrading the bandwidth of the relative phase shift. Owing to the phase characteristics of the transition studied in the chapter two, the frequency dependent phase delay of the employed slot for a specific substrate thickness (the 0.508 mm in our case) and slot dimensions can be compensated by properly modifying the effective length of the outer SIW. Upon determining the proper substrate thickness, the two-level transition is integrated to the SIW arms and then optimized together for wideband relative phase shift with respect to the matrix inner reference SIW arms to fit the overall geometrical design. This phase shift $\Delta\phi = \phi_o - \phi_t$ can be given by Eq. (4.10).

$$\Delta\phi = \phi_0 - \phi_2 = \left\{ l_0 \sqrt{\left(\frac{2\pi}{\lambda}\right)^2 - \left(\frac{\pi}{a_{0eff}}\right)^2} + \arg\left(S_{21}|_{slot}\right) \right\} - \left\{ l_i \sqrt{\left(\frac{2\pi}{\lambda}\right)^2 - \left(\frac{\pi}{a_{ieff}}\right)^2} \right\} \quad (4.10)$$

Where a_{oeff} and a_{ieff} are the effective widths of the rectangular waveguides equivalent to the SIW outer and inner arms, respectively. arg($S_{21}|_{slot}$) is the phase delay of the transition transverse slot which is the argument of Eq.(4.8). l_o and l_i are the effective path lengths of the outer and inner SIW arms, respectively.

As mentioned before, two different 4×4 wideband Butler matrix configurations are designed and optimized. Both matrices are designed to operate in the 11-14 GHz frequency band, the substrate being used and the SIW parameters are those mentioned in Section 4.3.1. The SIW widths of the outer arms of the phase shifters of *configuration 1* and *configuration 2* will be denoted by a_{SIWo1} and a_{SIWo2}, respectively. The width of the inner arms a_{SIWi} will be fixed for both configurations to the same value as that of the employed coupler, therefore $a_{SIWi} = a_{SIW}$. Both configurations are described, illustrating their corresponding simulation and measurement results in the following subsections. Simulation results account only for the central part of the matrix, whose length and width will be denoted by L_m and W_m respectively, the microstrip transitions are not considered either.

4.3.2.1. Configuration One

Owing to the two-layer design, this configuration is a direct two-layer mapping of the typical block diagram of Fig. 4.4. Fig. 4.7 illustrates the developed layout of the overall matrix while Fig. 4.8 (a) shows that of the employed SIW phase shifters. Exploiting the two-layer topology, the proposed design of the Butler matrix ensures a geometrical flexibility by exploring the lateral dimension on each layer while keeping the same physical longitudinal length L_1 for the matrix phase shifting arms.

Fig. 4.8 (b) shows the simulated and measured results for the insertion loss of the employed phase shifting arms together with the associated phase difference $\Delta\phi$. Simulated results show a wideband performance for the relative phase shift over the 11-14 GHz frequency band with a phase peak-to-peak error of 10° with respect to the required 45° phase difference. The optimized simulated insertion loss is kept below 0.6 dB for both arms over the entire frequency band. The additional insertion loss

observed for the outer arm with respect to that of the inner one is due to the presence of the two-level transition in the former one. Measured results are in good agreement with the simulated ones for both magnitude and phase. The slight increase observed in the measured insertion loss is due to the dispersive dielectric loss whose value was considered constant in the simulations.

Fig. 4.9 shows the simulated and measured results for transmission phase and magnitude parameters versus frequency when port 1 is fed. The wideband performance is clearly verified over the frequency band from 11 GHz to 14 GHz with a good agreement between the simulations and measurements. The maximum dispersion in the simulated transmission magnitudes is less than 1 dB, with an average value of -6.5 dB. Measured transmission magnitudes have almost the same dispersion characteristic of the simulated ones with an average value around -7 dB. Simulated and measured phase characteristics have peak-to peak dispersions less than 7° and 10°, respectively, with respect to the required theoretical scattering parameters given by Eq. (4.1). Moreover, the simulated reflection and isolation losses are below -15 dB over the entire frequency band, Fig. 4.10. The measured reflection coefficient is lower than -12 dB while the isolation coefficients are below -15 dB over the entire band.

Due to the symmetrical physical structure of the hybrid coupler used and the geometry of the matrix, the transmission dispersion characteristics as well as the reflection and isolation losses discussed above are expected to be almost the same when feeding from the other ports. This is verified from the results of Fig. 4.11 which also shows good agreement between the simulated and measured results. A slight increase in the measured insertion loss is observed for both cases (feed at port 1 and feed at port 2). This is attributed to the dispersive substrate losses, as well as, possible minor misalignment between the two layers.

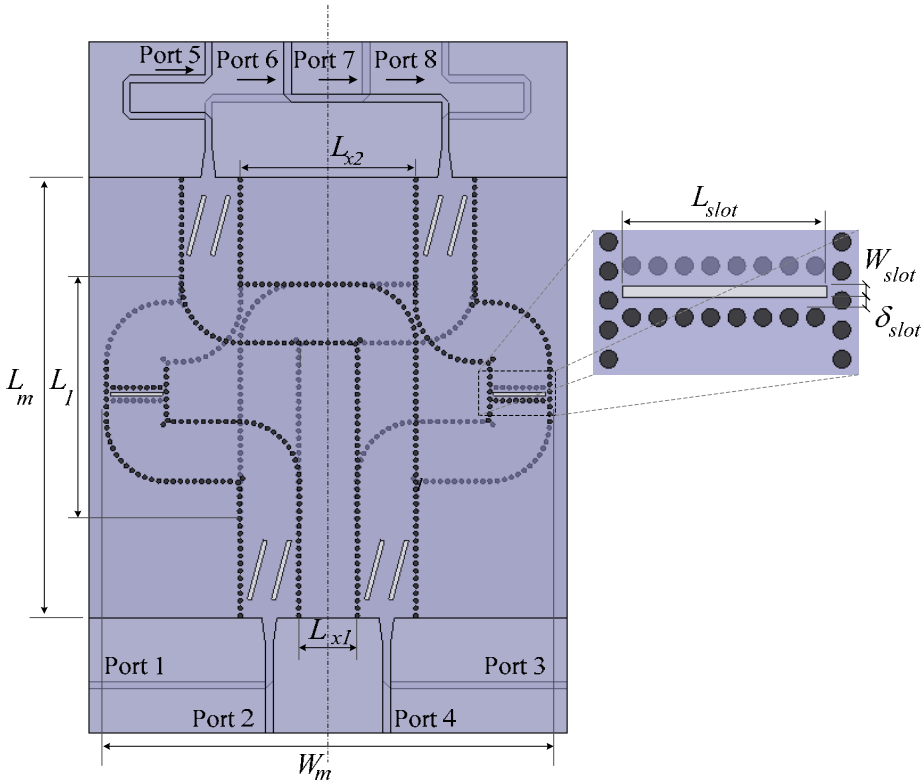

Fig.4.7 Complete layout of the developed configuration 1 for the 4x4 two-layer SIW Butler matrix, including phase-compensated (at the outputs) microstrip to SIW transitions. L_m=76.67mm (~$3\lambda_g|_{12.5GHz}$), W_m=77.2mm (~$3\lambda_g|_{12.5GHz}$), L_{x1}=10.2mm, L_{x2} =30.6mm, L_{slot}=9.11mm, W_{slot}= 0.5mm, δ_{slot}= 0.5mm. $\lambda_g|_{12.5GHz}$ is the waveguide wavelength at 12.5 GHz and is equal to 25.8 mm.

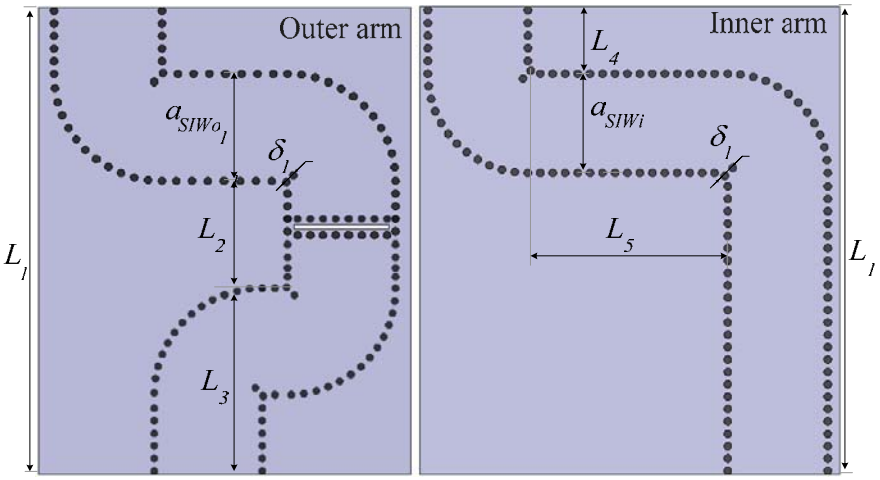

(a)

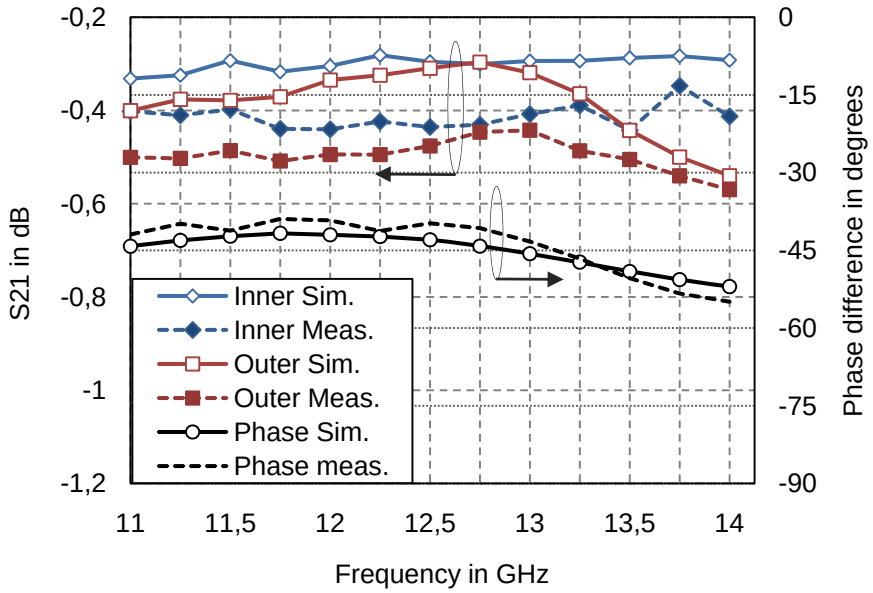

(b)

Fig.4.8 (a) Layout of the SIW phase shifting arms employed in *configuration 1*. L_1=51.2mm, L_2=10.4mm, L_3=19.32mm, L_4=5.84mm, L_5=20.4mm, a_{SIWo1}=10.4mm, a_{SIWi}=10.2mm, δ_1=1.06mm. (b) Simulated and measured insertion loss for the inner and outer arms together with the corresponding simulated and measured phase difference $\Delta\phi$ versus frequency.

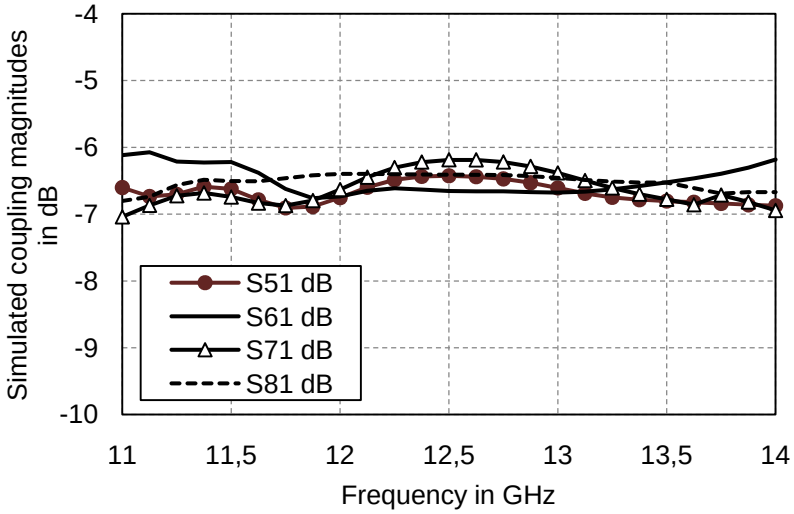

(a)

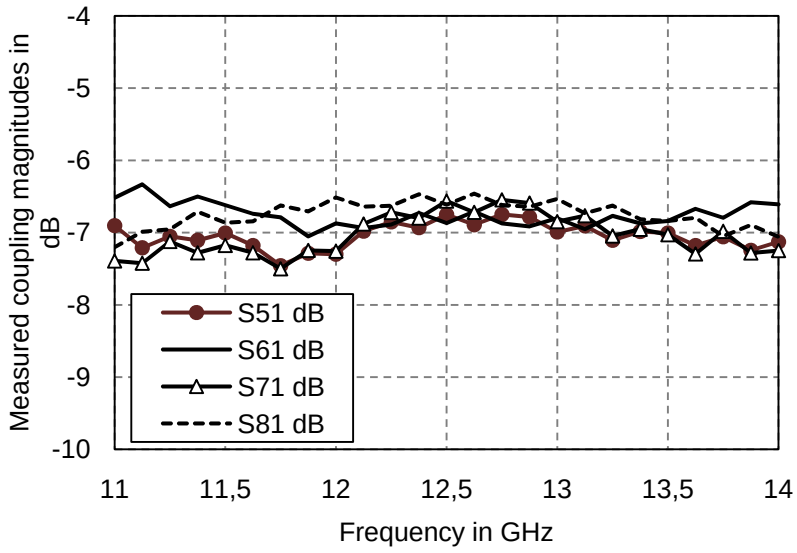

(b)

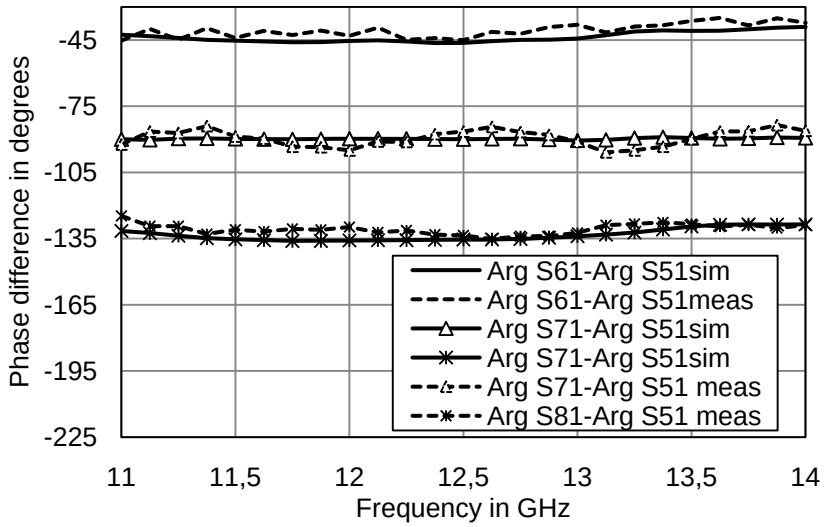

(c)

Fig. 4.9 Simulated and measured results for the coupling magnitudes and relative phase differences at the outputs versus frequency for the matrix *configuration 1* for feeding from port 1. (a) Simulated coupling magnitudes (b) Measured coupling magnitudes (c) Simulated and measured phase characteristics at the output ports with respect to that of port 5.

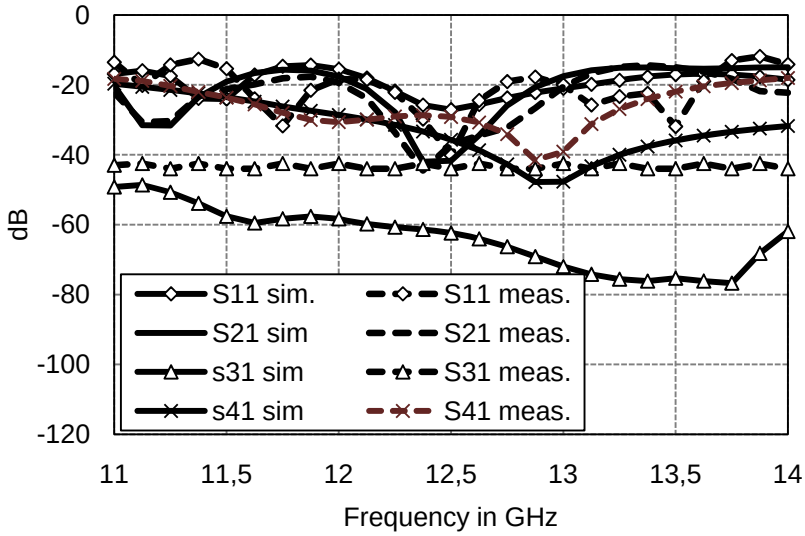

Fig. 4.10 Simulated and measured results for the isolation and reflection amplitudes versus frequency when feeding from port 1 for *configuration 1*.

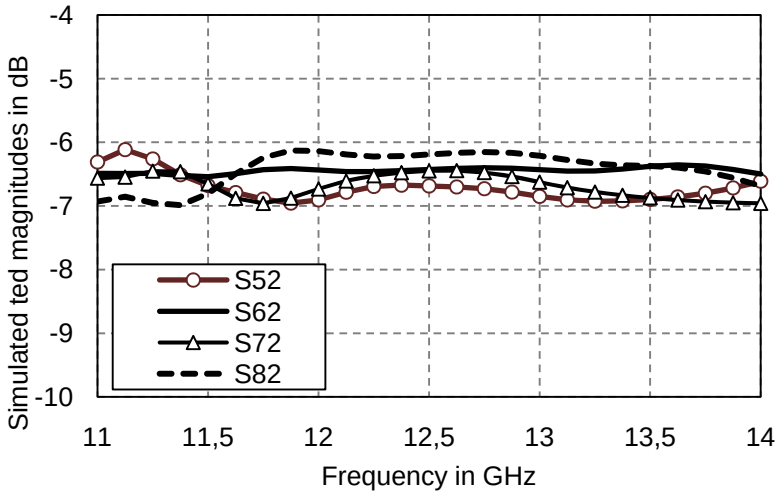

(a)

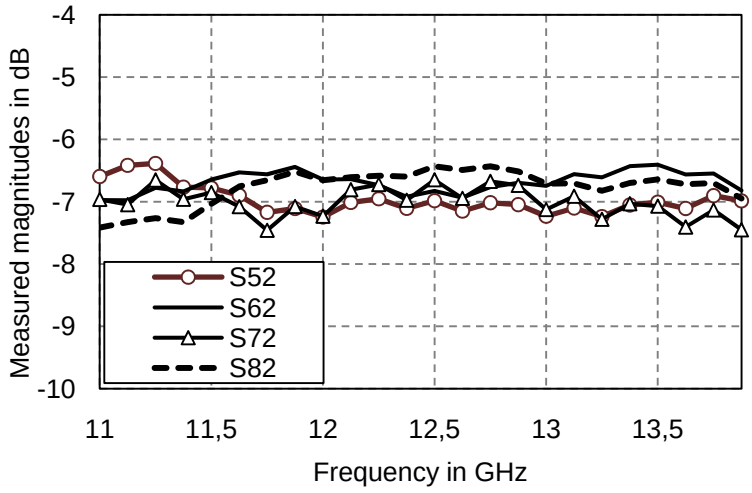

(b)

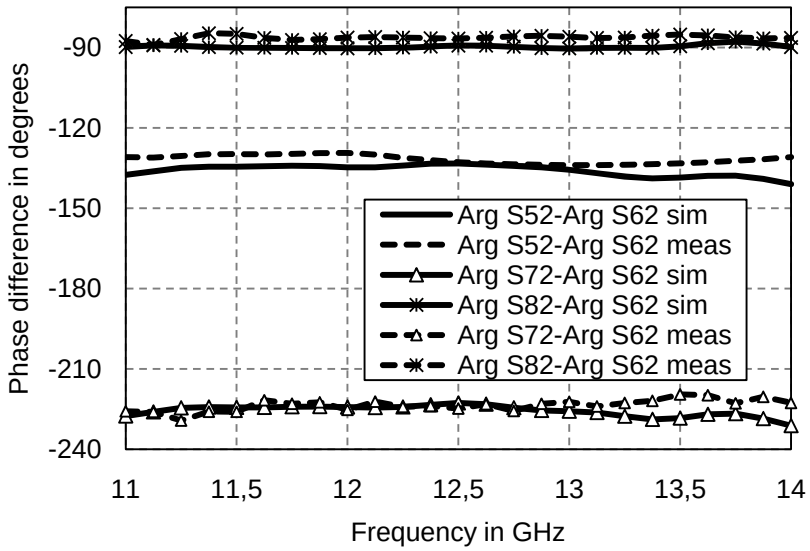

(c)

Fig. 4.11 Simulated and measured results for the coupling magnitudes and relative phase differences at the outputs versus frequency for the matrix *configuration 1* for feeding from port 2. (a) Simulated coupling magnitudes (b) Measured coupling magnitudes (c) Simulated and measured phase characteristics at the output ports with respect to that of port 6.

4.3.2.2. Configuration Two

Fig. 4.12 illustrates the proposed layout for *configuration 2*. In this configuration, a further improvement in the matrix layout is achieved by the implementation of common SIW walls between the adjacent hybrid couplers and parts of the SIW phase shifters. As they have the same SIW width of that of the hybrids, the central part of the inner SIW phase shifting arms are in fact a replica of the coupler waveguides shifted by $a_{SIW}/2$ in the lateral direction, Fig. 4.12. This allows a two-layer overlapped implementation of these arms; therefore, each arm is a mirrored image of the other with respect to the matrix geometrical central line, each in a separate layer. The outer arms are slightly shifted by the distance δ_2 for low insertion loss, relative wideband phase shift, and do share one of the SIW walls of the inner arms. Therefore, the overall width is reduced to half its value leading therefore to a size reduction of almost 50% with respect to *configuration 1*. The two-level transition parameters are shown in the insets in Fig. 4.12.

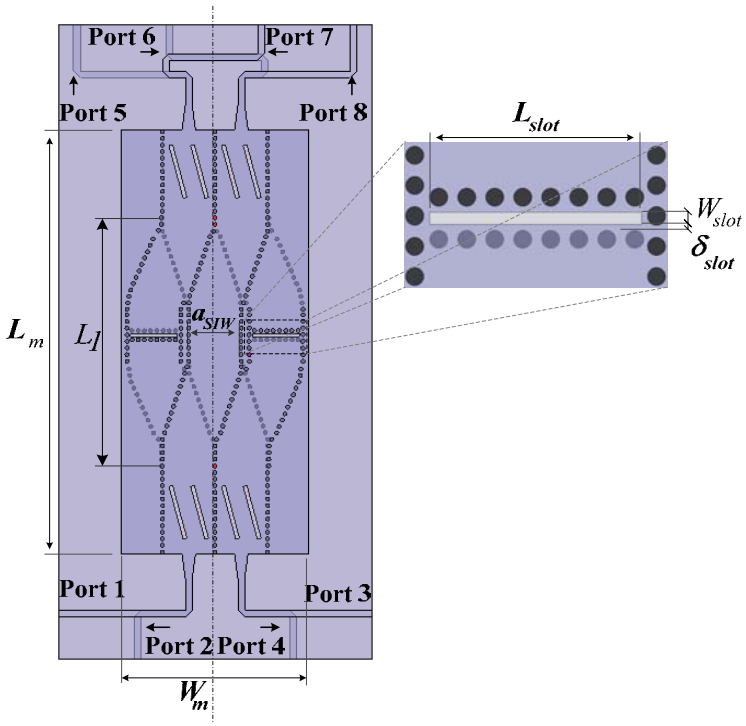

Fig. 4.12 Complete layout of the developed 4x4 two-layer SIW Butler matrix, *configuration 2*, including microstrip to SIW transitions. (b) Layout of the employed SIW phase shifting arms. L_m=83.18mm (~$3.2\lambda_g|_{12.5GHz}$), W_m=36.25mm (~$1.4\lambda_g|_{12.5GHz}$), L_{slot}=9.15mm, W_{slot}= 0.5mm, δ_{slot}= 0.25mm.

Fig. 4.13 (a) shows the layout of the employed phase shifting arms, while Fig. 4.13 (b) presents their corresponding simulated and measured results for the insertion loss and the associated phase difference $\Delta\phi$. Fig. 4.14 and Fig. 4.16 show the simulated and measured results for transmission phase and magnitude parameters versus frequency when feeding from ports 1 and 2 respectively. The simulated and measured reflection and isolation parameters are shown in Fig. 4.15. By considering the results of Fig. 4.13 (b) to Fig. 4.16, the wideband behavior is clearly verified with a good agreement between simulation and measurement results. As it can be expected, the matrix performances are quite similar to those of *configuration 1*. A slight enhancement (~0.2 dB) in the measured insertion losses for this configuration is generally observed compared to those of the former one validating the losses introduced due to slight misalignment between the two different layers of the matrix.

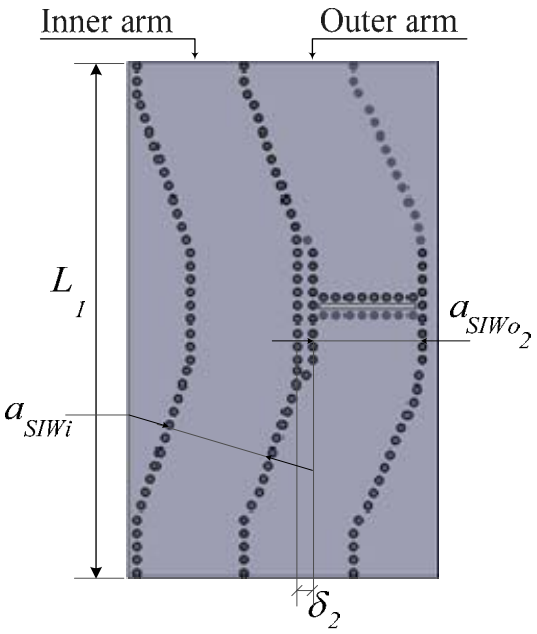

(a)

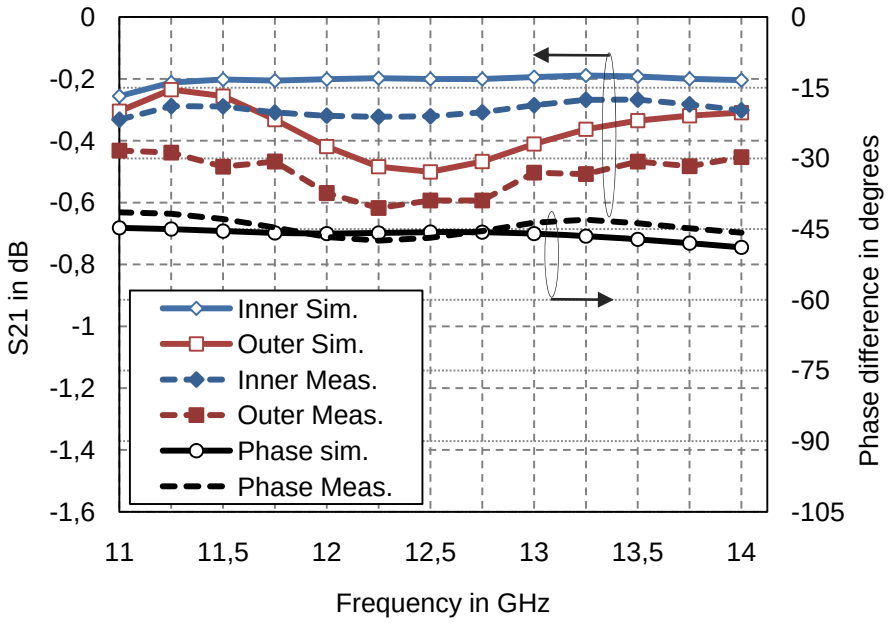

(b)

Fig. 4.13 (a) Layout of the SIW phase shifting arms employed in *configuration 2*. L_1=51.2mm, a_{SIWo2}=10.44mm, δ_2 =1.53mm. (b) Simulated and measured insertion loss for the inner and outer arms together with the corresponding simulated and measured phase difference $\Delta\phi$ versus frequency.

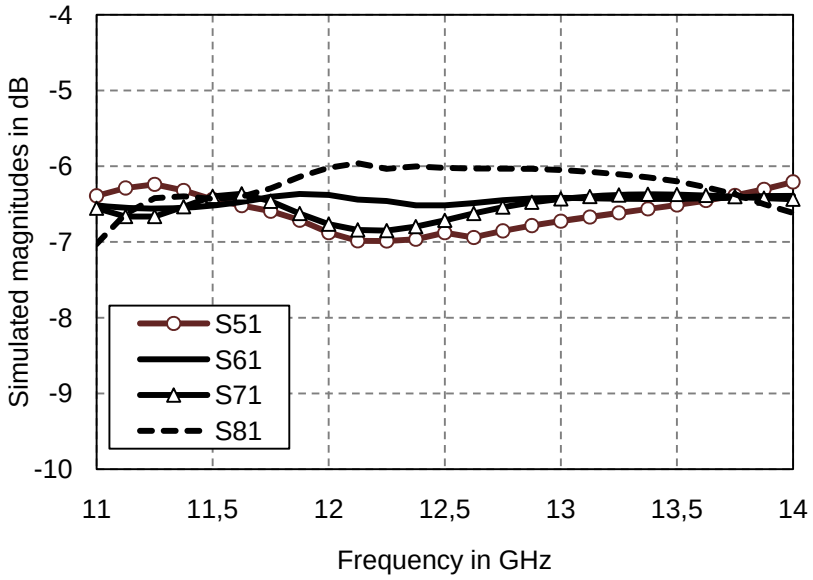
-4
-5
-6
-7
-8
-9
-10
Simulated magnitudes in dB
S51
S61
S71
S81
11
11,5
12
12,5
13
13,5
14
Frequency in GHz

(a)

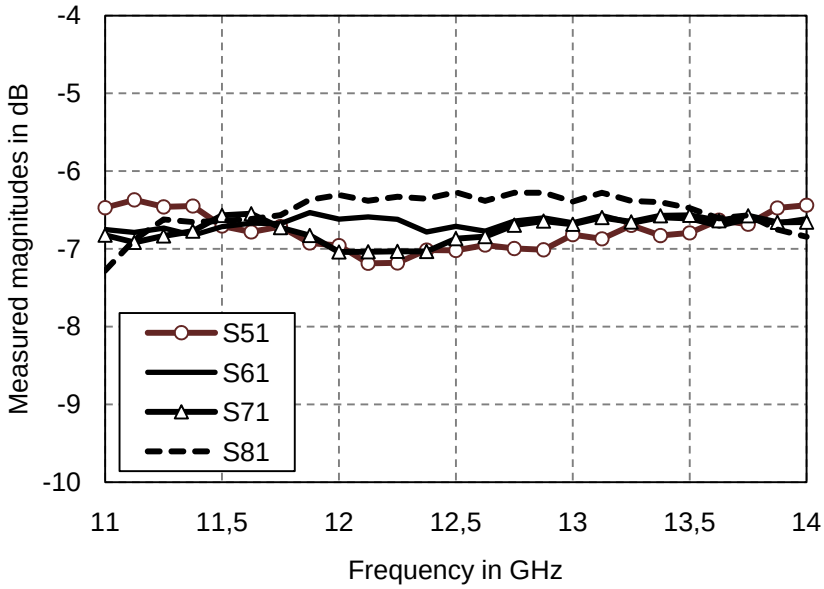
-4
-5
-6
-7
-8
-9
-10
Measured magnitudes in dB
S51
S61
S71
S81
11
11,5
12
12,5
13
13,5
14
Frequency in GHz

(b)

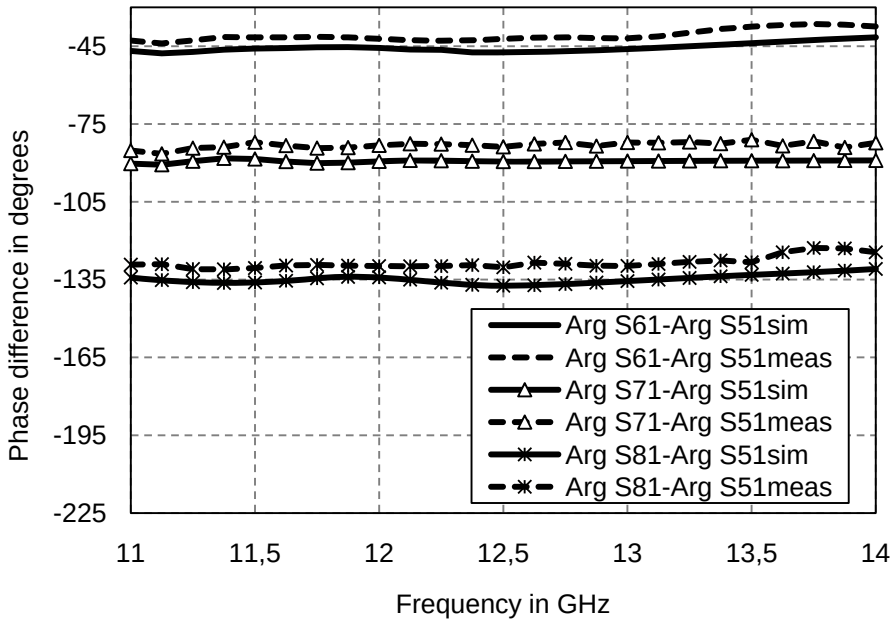

(c)

Fig. 4.14 Simulated and measured results for the coupling magnitudes and relative phase differences at the outputs versus frequency for the matrix *configuration 2* for feeding from port 1. (a) Simulated coupling magnitudes (b) Measured coupling magnitudes (c) Simulated and measured phase characteristics at the output ports with respect to that of port 5.

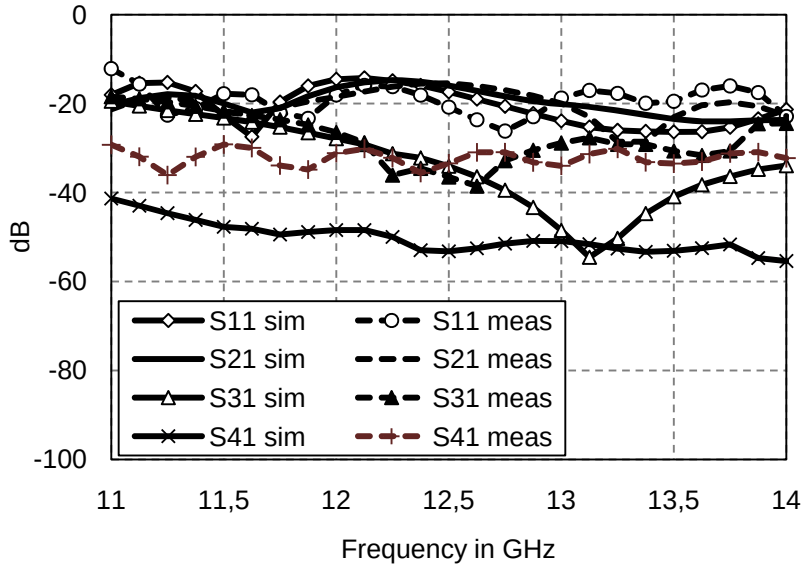

Fig. 4.15 Simulated and measured results for the isolation and reflection magnitudes versus frequency when feeding from port 1, *configuration 2*.

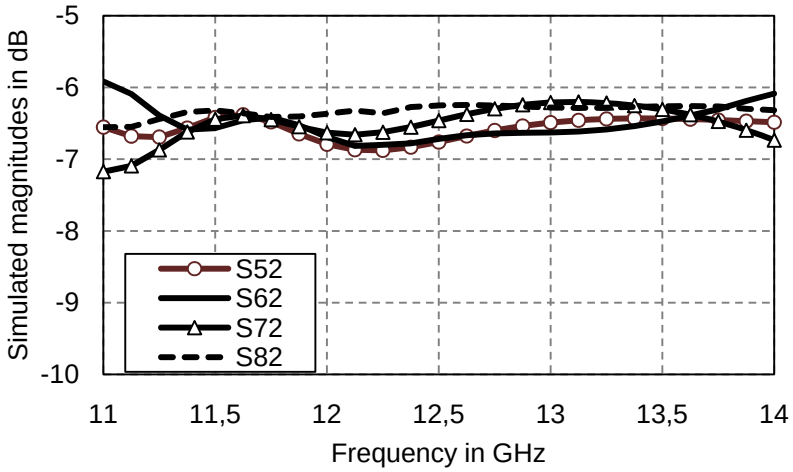

(a)

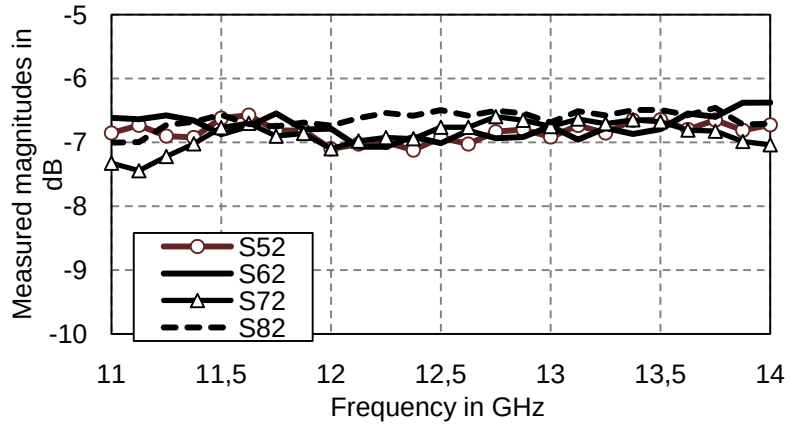

(b)

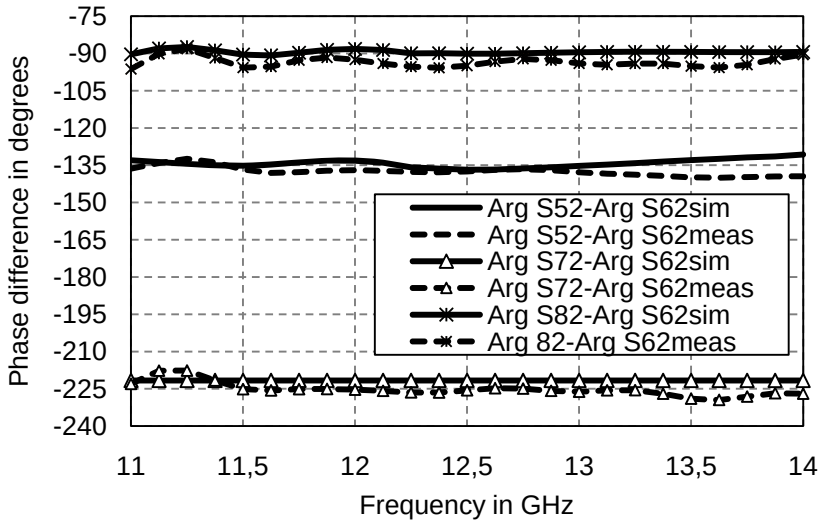

(c)

Fig. 4.16 Results for the coupling magnitudes and relative phase differences at the outputs versus frequency for the matrix *configuration 2* for feeding from port 2. (a) Simulated and (b) Measured coupling magnitudes (c) Simulated and measured phase characteristics at the output ports with respect to that of port 6.

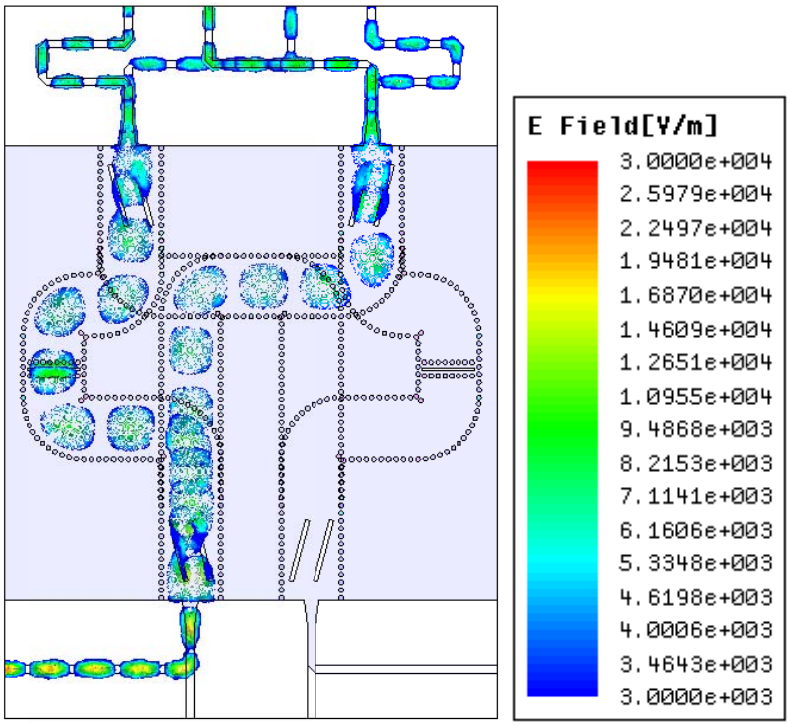

(a)

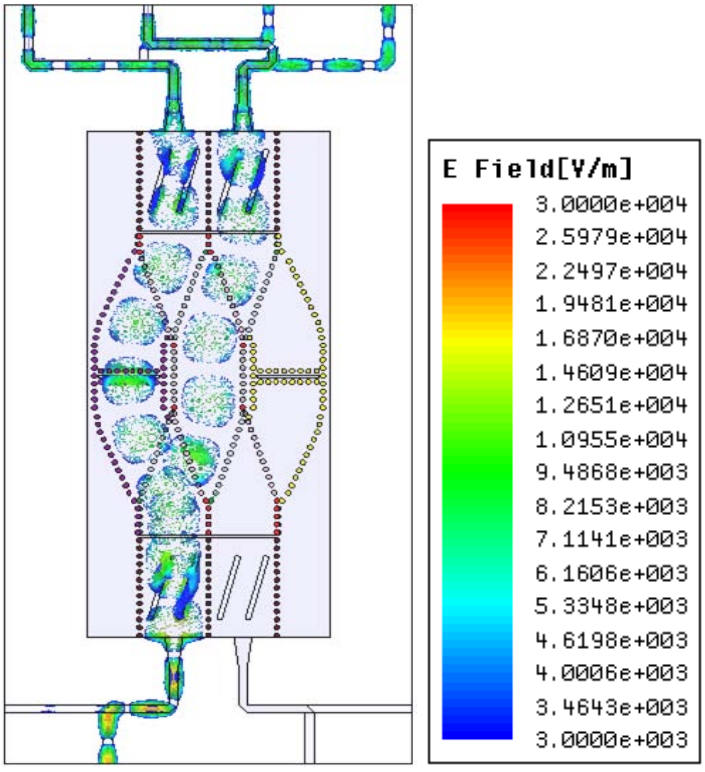

(b)

Fig. 4.17 Electric field magnitude pattern for the matrix excited at 12.5 GHz. (a) *Configuration 1*. (b) *Configuration 2*.

For both matrix configurations, the two layers are fabricated separately. The coupling slots for the 3-dB coupler and the two-layer transitions are etched in one layer only, while corresponding larger windows are etched in the other substrate layer to reduce losses due to alignment inaccuracies, Fig.4.18. To avoid the use of extra adhesive layers, copper eyelets (hollow pins) are used to attach the two layers through the pre-aligned sets of common holes between the two layers, bounding all regions including coupling slots, Figs.4.7 and Fig. 4.12. To ensure good metallization of SIW via holes, a thin copper layer is deposited using plasma vaporization prior to the classical copper electro-deposition process. The matrices are fabricated using the technological facilities of “Ecole Polytechnique de Montréal”, Poly-Grames Research Center, Quebec, Canada.

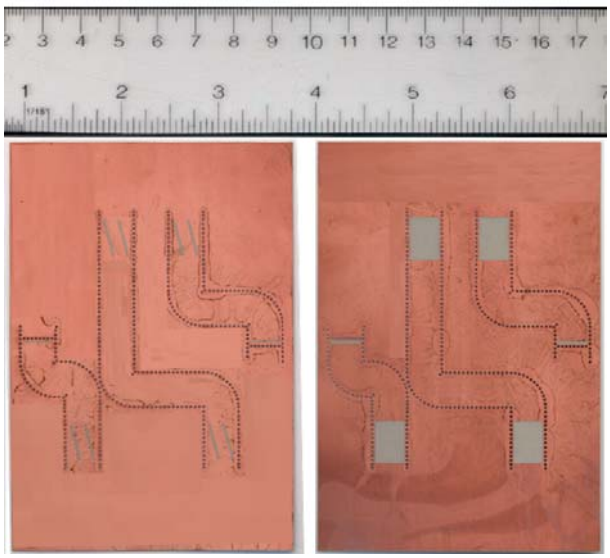

(a)

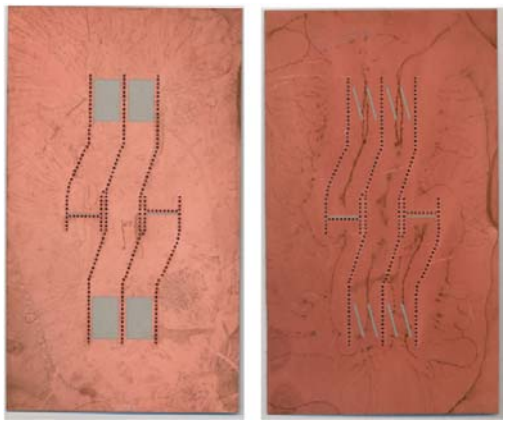

(b)

Fig. 4.18 Photograph of the common layer between the upper and lower substrates for both developed matrix configurations. (a) *Configuration 1*. (b) *Configuration 2*.

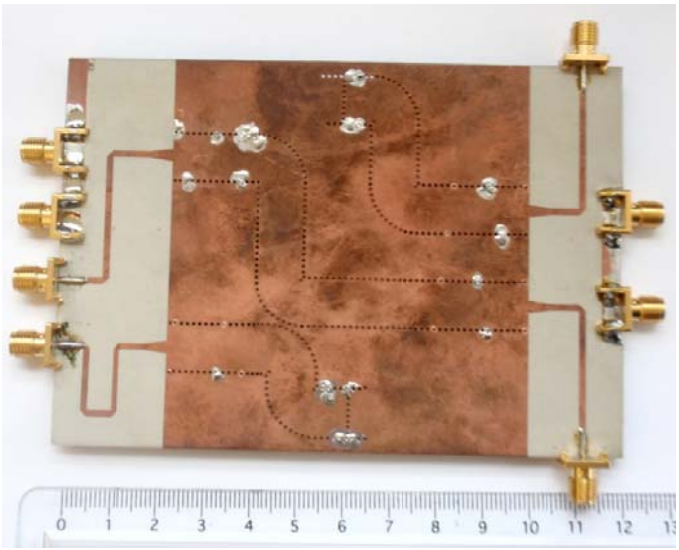

(a)

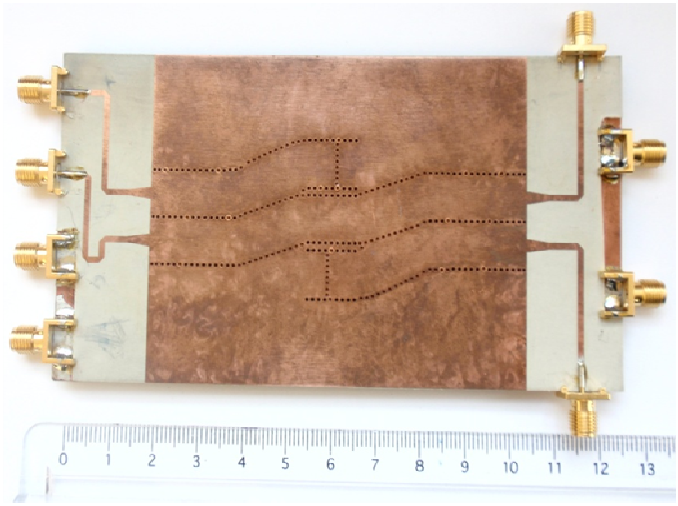

(b)

Fig.4.19 Photograph of the fabricated matrices. (a) *Configuration 1* (b) *Configuration 2*.

4.3.3. Use of the Developed Butler Matrix to Feed a Linear Antenna Array

In this section, the developed 4×4 Butler matrix is used as a feeding network for a multiple-beam antenna to investigate the impact of the phase and magnitude dispersions on the radiation pattern over the entire frequency band. The measured results of *configuration 2* are adopted to feed a theoretical 4-element linear array. The array inter-element spacing is set to $0.7\lambda_o$ at the design center frequency (12.5 GHz), while a small, low directivity antenna is selected as the radiator element.

The radiation pattern of the adopted array element is defined analytically by $cos^q(\theta), \theta$ is the observation angle with respect to the normal direction of the array

plane, with q set to 1.2. This type of antenna has been chosen together with the aforementioned value of d_s in order to reduce the grating lobes especially for those beams that have the highest values of θ_o, while maintaining realistic values.

Fig. 4.20 shows the calculated array radiation patterns versus frequency for the different input ports. According to Eq. (4.1) and Eq. (4.2) and the value of d_s, the theoretical pointing angles θ_o of the main beam produced at 12.5 GHz are -10.28°, +32.39°, -32.39° and +10.28° when feeding from ports 1 to 4 respectively. The calculated diagrams are therefore in good agreement with the theoretical ones at the design center frequency with values of θ_o of -9.25°, +30.0°, -29.5° and +9.6° when feeding at ports 1 to 4 respectively. On the other hand, as it could be expected owing to the wideband phase performance of the developed matrix, a relatively small main lobe beam squint less than 5° is observed over the 11.5-13.5 GHz frequency band. Interestingly, the natural beam squint of a linear array, due to the fact that the inter-element spacing normalized to the wavelength varies with the frequency, is of the same order. This means that the phase dispersion of the matrix over the operating bandwidth has almost no impact on the beam squint. The side lobe levels (SLL) remain around -10 dB. Typical value for a uniform magnitude array distribution is around -13 dB on the array factor. The element factor of the aforementioned array element has naturally an impact on the overall radiation pattern as it tends to degrade the side lobe levels of the beams with larger θ_o. This explains the SLL values between -10 and -9 dB of Figs. 18 (b) and (c). One can also note the existence of grating lobes in Fig. 4.20 (b) and (c). The levels of these grating lobes can be lowered by reducing the inter-element spacing down to 0.5 λ but this is obviously limited by the elementary radiator size. Most importantly, the coupling between elements will increase as they get closer which may degrade the overall performances. A preferred solution to reduce the grating lobes would be to increase the directivity of the elementary radiator, using stacked patch for instance in order to keep similar in-plane dimensions.

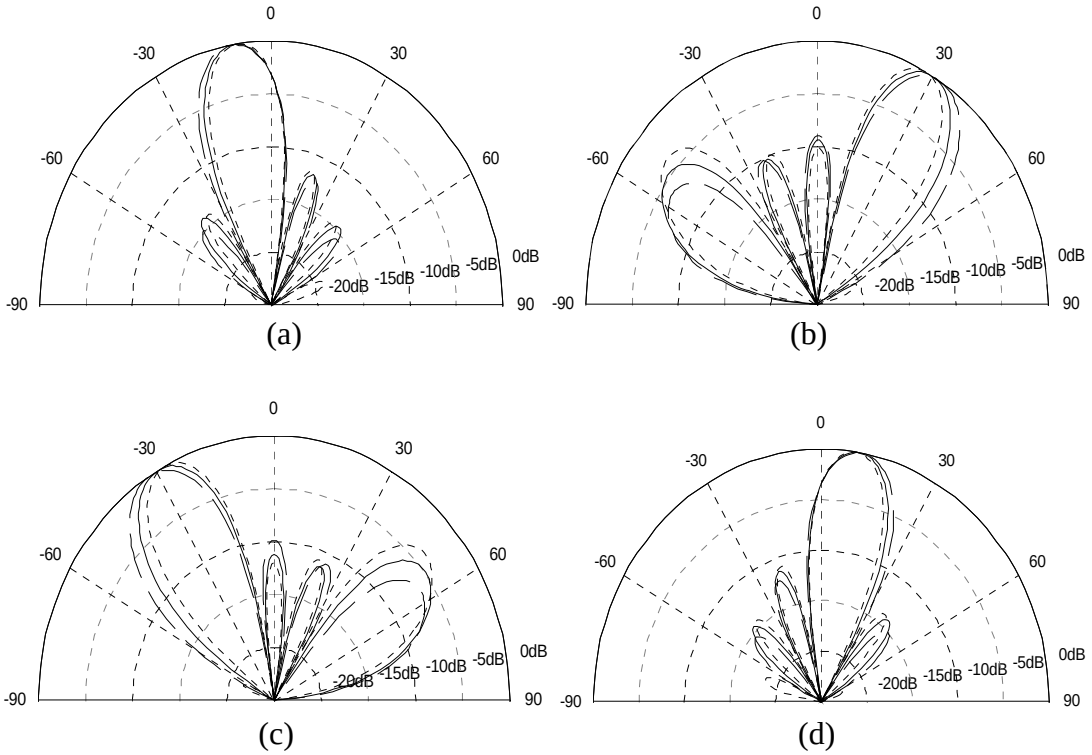

Fig. 4.20 Calculated radiation patterns versus frequency of a 4-element linear array fed by the developed Butler matrix, for different input ports. (a) Port 1. (b) Port 2. (c) Port 3. (d) Port 4. Dashed line: 11.5 GHz, solid line: 12.5 GHz and dotted line: 13.5 GHz.

4.3.4. Conclusion

A novel compact two-layer Butler matrix has been presented in SIW technology. Two 4×4 prototypes have been optimized, fabricated and tested. A space saving design with shared walls between adjacent electrical paths has also been validated, exploiting the flexibility of the two-layer SIW technology to reduce the matrix dimensions. The developed matrix has shown good dispersion characteristics in terms of insertion, reflection and isolation losses together with phase characteristics over 24 % bandwidth centered at 12.5 GHz. The two proposed designs have similar performances emphasizing that high component density is acceptable for small size sub-systems, with limited impact on isolation between electrical paths. To evaluate to which extent the compact design can be generalized; a combination of shared walls and stand alone waveguides may be the solution for larger matrices. Furthermore, the proposed implementation offers a robust, compact design, suitable for the implementation of these larger matrices.

References of Chapter Four

[1] P. S. Hall and S. J. Vetterlein, "Review of radio frequency beamforming techniques for scanned and multiple beam antennas," *IEE proceedings*, vol. 137, no. 5, pp. 293-303, 1990.

[2] A. El-Zooghby, "Potentials of Smart Antennas In CDMA Systems and Uplink Inprovements," *IEEE Ant. Prop. Mag.*, vol. 43, no. 5, pp.172-177, Oct. 2001.

[3] B. Piovano, L. Accatino, A. Angelucci, T. Jones, P. Capece and M. Votta "Design and breadboarding of wideband NxN Butler matrices for multiport amplifiers," *Microw. Conf.*, Brazil, SBMO, pp. 175-180, 1993.

[4] J. Blass, Multi-directional antenna: New approach top stacked beams, *IRE Int. Convention Record*, Pt 1, 1960, pp 48-50.

[5] J. Nolen, "Synthesis of multiple beam networks for arbitrary illuminations," Ph. D. Thesis, Bendix Corporation, Radio Division, Baltimore, April 1965.

[6] W. Rotman and R. F. Tuner, "Wide-angle microwave lens for line source applications," *IEEE Trans. Ant. Prop.*, vol. 11, pp. 623-632, 1963.

[7] J. Butler and R. Lowe, "Beam-forming matrix simplifies design of electrically scanned antennas," *Electron design*, pp. 170-173, 1961.

[8] C. Dall'Omo, T. Monediere, B. Jecko, F. Lamour, I wolk and M. Elkael, "Design and reslization of a 4x4 Microstrip Butler matrix without any crossing in millimeter waves," *Microw. Opt. Tech. Lett.*, vol. 38, no. 6, pp.462-465, Sep. 2003

[9] H. Hayashi, D.A. Hitko and C. G. Sodini, "Four-element planar butler matrix using half-wavelength open stubs," *IEEE Microw. Wireless Comp. Lett.*, vol. 12, no.3, Mar. 2002.

[10] F. Alessandri, M. Dionigi and L. Tarricone, "Rigorous and efficient fabrication-oriented CAD and optimization of complex waveguide networs," *IEEE Trans. Microw. Theory Tech.*, vol. 45, no. 12, pp. 2366-2374, Dec. 1997.

[11] T. N. Kaifas and J. Sahalos, "On the design of a single-layer wideband butler matrix for switched-beam UMTS system applications," *IEEE Trans. Ant. Prop.*, vol. 48, pp. 193-204, Dec. 2006.

[12] J. Hirokawa, F. Murukawa, K. Tsunekawa a,d N. Goto, " Double-layer structure of rectangular-waveguides for Butler matrix," *European Microw. Conf.*, pp.1-4, Milan, Oct. 2002.

[13] M. Bona, L. Manholm, J. P. Starski and B. Svensson, "Low-loss compact Butler matrix for a microstrip antenna," *IEEE Trans. Microw. Theory Tech.*, vol. 50, no.9, pp.2069-2075, Sep. 2002.

[14] M. Nedil, T. A. Denidi and L. Talbi, “Novel Butler matrix using CPW multilayer technology,” *IEEE Trans. Microw. Theory Tech.*, vol. 54, no.1, pp.499-507, Jan. 2006.

[15] D. Deslandes and K. Wu, “Integrated Microstrip and rectangular waveguide in planar form,” *IEEE Microw. Wireless Comp. Lett*., vol. 11, pp. 68-70, Feb. 2001.

[16] E. Sbarra, L. Marcaccioli, R. V. Gatti and R. Sorrentino, “A novel Rotman lense in SIW technology,” *Europ. Microw. Conf.*, Munich, Oct. 2007, pp. 1515-1518.

[17] Y. Cheng, W. Hong, K. Wu, Z. Q. Kuai; C. Yu; J. X. Chen, J. Y. Zhou and H. J. Tang, “Substrate integrated waveguide (SIW) Rotman lens and Its Ka-Band Multibeam Array Antenna Applications,” *IEEE Trans. Ant. Prop*., vol. 56, pp. 2504-2513, 2008.

[18] T. Djerafi, N. Fonseca and K. Wu, “Planar Ku-band 4×4 Nolen matrix in SIW technology,” *IEEE Trans. Microw. Theory Tech*., Vol. 58, No. 2, pp. 259-266, Feb. 2010.

[19] S. Yamamoto, J. Hirokawa and M. Ando, “A beam switching slot array with a 4-way Butler matrix installed in a single layer post-wall waveguide,” *IEEE AP-S Int. Symp*., San Antonio, June 2002, pp. 138-141.

[20] Lo, Y. T. et Lee, S.W. 1998. Antenna Handbook. New York: Van Nostrand Reinhold.

[21] N. J. G. Fonseca, Etude des matrices de Blass et Nolen, CNES Technical Note n° 152, 98 pages, Nov. 2007.

[22] S. Mosca, F. Bilotti, A. Toscano and L. Vegni, “A novel design method for Blass matrix beam-forming networks,” *IEEE Trans. Ant. Prop*., vol. 50, No. 2, pp. 225-232, Feb. 2002.

[23] N. J. G. Fonseca, “Printed S-band 4×4 Nolen matrix for multiple beam antenna applications,” *IEEE Trans. Ant. Prop*., vol. 57, No. 6, pp. 1673-1678, June 2009.

[24] W. White, “Pattern limitations in multiple-beam antennas,” *IRE Trans. Ant. Prop*., vol. 10, pp. 430-436, July 1962.

[25] Y. Cheng, W. Hong and K. Wu, “Novel Substrate Integrated Waveguide fixed phase shifter for 180-degree Directional Coupler,” *IEEE MTT-S*, pp. 189-192, Honolulu, June 2007.

[26] J. L. Allen, “A theoretical limitation on the formation of lossless multiple beams in linear arrays,” *IRE Trans. Ant. Prop*., Vol. 9, pp. 350-352, July 1961.

Conclusion

The motivation of this thesis is to explore the potentials of the Substrate Integrated Waveguide (SIW) technology, in particular, multi-layer implementations, in order to develop a compact wideband beam-forming matrix in two-layer topology. To achieve our goal, first we had to choose the matrix type that meets all required specifications and for which a two-layer SIW implementation would be of particular interest. Between the different types of BFNs, the Butler matrix has received a remarkable interest in literature as it is theoretically lossless and it can produce orthogonal beams while employing the minimum number of components. The Butler matrix suffers however from a basic structural disadvantage which is the presence of path crossings in its typical architecture. The use of two-layer topology appears then to have promising potential to bypass this problem without employing additional components neither specific design.

Among the different technologies, the SIW technology has received a growing interest in the last decade, as it maintains the advantages of rectangular waveguides in terms of low-loss, high quality factor and higher power handling capability than the planar transmission lines while being compatible to low-cost PCB and LTCC technologies. The first chapter of this thesis addressed the state of the art of BFNs, as well as the historical development of SIW technology and BFNs reported so far in literature in SIW technology. Upon determining the suitable candidate for BFN, the following step of this research was to explore the potentials of SIW technology with the degree of freedom of the multi-layer design to develop novel passive components. As the final goal of this work was to achieve a Butler matrix, the attention was focused on the two-basic building elements of the matrix, namely couplers and phase shifters.

Starting with the phase shifters, different novel topologies were investigated. First, a single-layer Composite Right/Left Handed (CRLH) structure was proposed. The structure was based on a single-layer waveguide with shunt inductive windows (irises) and series transverse capacitive slots, suitable for SIW implementations for compact phase shifters. By varying both right-handed and left-handed parameters

between different structures, wideband relative phase shifts could be obtained with a wide phase dynamic range. The main disadvantage of this structure was that it had relatively large insertion loss values, especially in applications requiring many phase shifters as beam-forming matrices. These insertion loss values were however within the typical range of non-lumped elements based CRLH implementations. Then, to exploit the multi-layer SIW topology, a novel wideband, low-loss two-layer transition was developed. The transition was based on a transverse narrow slot coupling two short-ended waveguides in two different layers. According to a wideband equivalent circuit model, a detailed study of the transmission phase and magnitude of the transition was carried out. Based on its equivalent circuit model, the transition could be optimized within the well known unequal width, equal-length SIW phase shifters in order to compensate its additional phase shift within the frequency band of interest. This two-layer wideband phase shifter scheme was adopted in the final developed matrix architecture. On the other hand, the low-loss wideband interconnect was then exploited to develop a three-layer, multiply-folded waveguide structure as a good candidate for compensated-length, variable width, low-loss, compact wideband phase shifters in SIW technology.

The following step was to investigate the SIW facilities in the development of novel coupler structures. Two novel multi-layer SIW couplers were developed. The first structure was that of a 90^{o} coupler that consisted of two parallel waveguides coupled through a pair of offset, inclined resonant slots etched in their common broad wall. By modifying the slots parameters, namely the slot length, inclination angle and offset, a wide coupling dynamic range with wideband performance for the coupling level and the phase quadrature between the direct and coupled ports could be achieved. A detailed parametric study for the slots parameters was carried out providing a good understanding of the coupler characteristics for both the coupling magnitude and transmission phase performances. Moreover, the coupler structure allowed the phase compensation for different coupling levels, in other words, different coupling levels could be achieved while maintaining the same phase delay at the output. A 6 dB coupler was experimentally verified, showing a 16% coupling bandwidth at 12.5 GHz with good isolation and reflection performances.

Another ridged-waveguide-based 180^{o} ring coupler was developed. The coupler was endowed with a novel compact design based on two concentric hybrid ring couplers offering an arbitrary dual band performance. The outer ring was

responsible for the lower frequency band operation while the coupling at the higher frequency band was carried out by the inner (smaller) one. To avoid the propagation of the higher frequency band in the outer ring, an original solution was proposed. The ridged waveguide of the outer ring was periodically loaded by radial defects in the form of transverse slots loaded by short ended waveguide sections. The separation between the slots was a crucial parameter to create a bandgap for the higher frequency band propagation in the outer ring. The loading waveguide sections had a width, such that, they became below cutoff for the lower frequency band, to avoid the presence of ripples in the corresponding coupling performance of the outer ring. The higher frequency band was therefore guided towards the inner coupler. The use of the ridged waveguide allowed a large separation between the two arbitrary operating bands. The maximum separation was limited by the fundamental mode bandwidth of the adopted ridged waveguide parameters, while tight separations could be achieved by increasing the size of the outer ring, thus compromising the total area of the coupler. A design procedure was presented to develop a C/K dual band coupler with bandwidths of 8.5% and 14.6% centered at 7.2 GHz and 20.5 GHz, respectively.

Finally, the last step to reach our goal was to develop a 4×4 wideband Butler matrix employing the previously developed SIW components. Prior to the Butler matrix design, the phase compensation of the previously designed parallel-waveguide coupler was investigated through a two-layer layout for a 4×4 Nolen matrix where the design limitations were identified. For the Butler matrix design, two 4×4 prototypes were optimized, fabricated and tested. The use of the two-layer SIW topology was exploited in a space saving design with shared walls between adjacent electrical paths to reduce the matrix dimensions without using extra 0 dB couplers. The two proposed designs had similar performances with good dispersion characteristics in terms of insertion, reflection and isolation losses together with phase characteristics over 24 % bandwidth centered at 12.5 GHz. Furthermore, the proposed implementation employing the shared SIW walls, offered a robust, compact design, suitable for the implementation of larger matrices.

Future work will focus on the development of novel SIW components in single and multi-layer topologies, the investigation of the phase compensation within the designed SIW Nolen matrix and other SIW BFNs for the beam squint with respect to frequency as well as the control of the side lobe level in BFNs.

List of Publications

Journal Articles

1. A. Ali, N. J. G. Fonseca, F. Coccetti and H. Aubert, "Design and Implementation of Two-Layer Compact Wideband Butler Matrices in SIW Technology for Ku-Band Applications," *IEEE Trans. Antennas Propagat.,*Accepted for publication.

2. N. J. G. Fonseca, A. Ali and H. Aubert, "On the Beam Pointing Stability versus Frequency of Serial Beam Forming Networks," submitted to *IEEE Antenna Prop. Mag.*

3. A. Ali, H. Aubert, N. Fonseca and F. Coccetti and, "Wideband two-layer SIW coupler: design and experiment," *Electronics Lett.*, Vol. 45, No. 13, pp. 687-689, June 2009.

4. A. Ali and H. Aubert, "Fractal superlattice cover with variable lacunarity for patch antenna directivity enhancement, analysis and design," *WSEAS Trans. on Communications*, Vol. 7, No.10, pp. 1035-1044.

International Conferences

5. A. Ali, N. J. G. Fonseca and H. Aubert, "Analysis and design of a compact SIW-based wideband phase shifter for Ku-band applications," *Antenna Propagat. Symp.*, Toronto, July 2010.

6. S. Bouaziz, A. Ali and H. Aubert, "Planar wideband microstrip antenna with inclined radiation pattern for C-band airborne applications, design and measurement," *IEEE Europ. Conf. Antenna Propagat.* (EUCAP'10), Barcelona, April 2010.

7. S. Bouaziz, A. Ali and H. Aubert, "Low-profile wideband antenna with unidirectional inclined radiation pattern for C-band airborne applications," *IEEE Asia Pac. Microw. Conf.* (APMC'09), Singapore, Dec. 2009.

8. A. Ali, H. Aubert, F. Coccetti and N. Fonseca, "Novel compact three-layer wideband phase shifter in SIW technology," *Progress in Electromagn. Research Symp.* (PIERS'09), Moscow, Aug. 2009.

9. A. Ali, H. Aubert, F. Coccetti and N. Fonseca, "Novel compact waveguide-based composite right/left-handed phase shifter with arbitrary phase shift and broad bandwidth: analysis and design," *IEEE Antenna Propagat. Symp.* (AP-S'09), Charleston, June 2009.

10. A. Ali, A. Coustou and H. Aubert, "wide band passive repeaters: design and measurements," IEEE *Antenna Propagat. Symp.* (APS'09), Charleston, June. 2009.

11. A. Ali, N. Fonseca, F. Coccetti and H. Aubert, "Novel two-layer 4x4 SIW Nolen matrix for multi-beam antenna application in Ku band," *IEEE Europ. Conf. Antenna Propagat.* (EUCAP'09), Berlin, March 2009.

12. A. Ali, N. Fonseca, F. Coccetti and H. Aubert, “Novel two-layer broadband 4x4 Butler matrix in SIW technology for Ku-band applications,” *IEEE Asia Pac. Microw. Conf.* (APMC’08), Hong Kong, Dec. 2008.

13. A. Ali, F. Coccetti, H. Aubert and N. Fonseca, “Novel multi-layer SIW broadband coupler for Nolen matrix design in Ku band,” IEEE *Antenna Propagat. Symp.* (APS’08), San Diego, Jul. 2008.

National Conferences

14. A. Ali, N. Fonseca, F. Coccetti and H. Aubert, “Nouvelles structures passives bicouches à base de GIS pour des matrices de répartitions multifaisceaux compactes,” 16^{ième} Journées Nationales de Micro-ondes, Grenoble, Mai 2009.